7 - 19

Multicenter Evaluation of a Standardized Protocol for Rest and Acetazolamide Cerebral Blood Flow Assessment Using a Quantitative SPECT Reconstruction Program and Split-Dose ^{123}I-Iodoamphetamine

Hidehiro Iida[1,2], Jyoji Nakagawara[1,3], Kohei Hayashida[1,4], Kazuhito Fukushima[1,5], Hiroshi Watabe[1,2], Kazuhiro Koshino[1,2], Tsutomu Zeniya[1,2], and Stefan Eberl[1,6]

[1]Dual-Table Autoradiography SPECT Research Group in Japan, Osaka, Japan; [2]National Cerebral and Cardiovascular Center–Research Institute, Osaka, Japan; [3]Nakamura Memorial Hospital, Sapporo, Japan; [4]Takeda Hospital, Kyoto, Japan; [5]National Cerebral and Cardiovascular Center–Hospital, Osaka, Japan; and [6]Royal Prince Alfred Hospital, Sydney, Australia

SPECT can provide valuable diagnostic and treatment response information in large-scale multicenter clinical trials. However, SPECT has been limited in providing consistent quantitative functional parametric values across the centers, largely because of a lack of standardized procedures to correct for attenuation and scatter. Recently, a novel software package has been developed to reconstruct quantitative SPECT images and assess cerebral blood flow (CBF) at rest and after acetazolamide challenge from a single SPECT session. This study was aimed at validating this technique at different institutions with a variety of SPECT devices and imaging protocols. **Methods:** Twelve participating institutions obtained a series of SPECT scans on physical phantoms and clinical patients. The phantom experiments included the assessment of septal penetration for each collimator used and of the accuracy of the reconstructed images. Clinical studies were divided into 3 protocols, including intrainstitutional reproducibility, a comparison with PET, and rest–rest study consistency. The results from 46 successful studies were analyzed. **Results:** Activity concentration estimation (Bq/mL) in the reconstructed SPECT images of a uniform cylindric phantom showed an interinstitution variation of ±5.1%, with a systematic underestimation of concentration by 12.5%. CBF values were reproducible both at rest and after acetazolamide on the basis of repeated studies in the same patient (mean ± SD difference, −0.4 ± 5.2 mL/min/100 g, n = 44). CBF values were also consistent with those determined using PET (−6.1 ± 5.1 mL/min/100 g, n = 6). **Conclusion:** This study demonstrates that SPECT can quantitatively provide physiologic functional images of rest and acetazolamide challenge CBF, using a quantitative reconstruction software package.

Key Words: ^{123}I-iodoamphetamine; cerebral blood flow; acetazolamide; SPECT; vascular reactivity; quantitation

J Nucl Med 2010; 51:1624–1631
DOI: 10.2967/jnumed.110.078352

Received Apr. 27, 2010; revision accepted Jul. 14, 2010.
For correspondence or reprints contact: Hidehiro Iida, Department of Investigative Radiology, National Cerebral and Cardiovascular Center–Research Institute, 5-7-1 Suita City, Osaka 565-8565, Japan.
E-mail: iida@ri.ncvc.go.jp

Current clinical practice using SPECT relies largely on interpretation of qualitative images reflecting physiologic function. Quantitative functional parametric images may be obtained by applying mathematic modeling to SPECT data corrected for attenuation and scatter. Quantitative regional cerebral blood flow (CBF) (*1–3*) and cerebral vascular reactivity (CVR) in response to acetazolamide challenge (*4–6*) have been obtained with these techniques. One major application of such quantitative SPECT (QSPECT) approaches is the evaluation of ischemic status in patients with occlusion or stenosis in their middle cerebral arteries, to provide prognostic information of the outcome of revascularization therapies (*7*). Quantitative analysis in SPECT has also been demonstrated in the assessment of binding potential for several neuroreceptor ligands (*8,9*), for the quantitative assessment of regional myocardial perfusion (*10,11*), and for the assessment of radioaerosol deposition and clearance in healthy and diseased lungs (*12*). However, providing the standardized quantitative approach required for multicenter clinical trials has so far received only limited attention. Challenges remain in providing consistent quantitative data across institutions using a variety of SPECT equipment and vendor-specific reconstruction strategies (*13*). This limitation is attributed to a lack of standardized procedures in the reconstruction software offered by vendors, particularly in terms of correcting attenuation and scatter. Kinetic modeling for physiologic parameter estimation is also not part of the vendors' standard SPECT software. Although separate packages can be purchased for this purpose, they are not integrated and are flexible general-purpose packages, requiring considerable skill and knowledge to effectively use. Thus, they are not ideal for routine clinical use.

Scatter and attenuation occur in the object and are thus object-dependent but are not dependent on the geometry of the imaging equipment (*14*). Therefore, once a software program is developed to provide accurate image reconstruction with compensation for both attenuation and scatter, the

237

program should be able to provide quantitative images that are intrinsically independent of the geometric design of SPECT cameras. This is an attractive feature of SPECT for multicenter clinical studies.

From the various techniques available to correct for attenuation (*15*) and scatter (*16*), one feasible approach for clinical studies is based on a combination of attenuation correction, incorporated into the ordered-subset expectation maximization (OSEM) reconstruction (*17*), and scatter correction by the transmission-dependent convolution subtraction (TDCS) originally proposed by Meikle et al. (*18*). This approach has been extensively investigated by our group (*11,19*) for ^{99m}Tc for studies of the brain and heart (*18,20*) and also in cardiac ^{201}Tl studies (*11,21*). A recent study also demonstrated the accuracy of this approach in a combined SPECT/CT system (*22*). By incorporating a correction for collimator septal penetration by high-energy emissions, one can also make the technique applicable to ^{123}I (*19*).

The QSPECT reconstruction approach has estimated CBF images at rest in a clinical setting (*11*) and quantified CVR by measuring CBF at rest and after vasodilation in a single SPECT session. This was accomplished by using the dual-table autoradiographic (DTARG) method and a dual administration of ^{123}I-iodoamphetamine (*23*). In those studies, corrections for attenuation and scatter appeared to be essential for generating quantitative CBF maps that were consistent with those generated by ^{15}O-water PET (*11,23*).

These studies were, however, validated in a single institution using a limited range of SPECT systems, and the general applicability of this technique for different SPECT systems had yet to be fully established. Thus, the aim of this study was to verify that analysis of data with a standardized reconstruction package incorporating attenuation and scatter correction can provide reproducible results across multiple institutions for quantitative rest and acetazolamide challenge CBF estimation from a single SPECT session.

MATERIALS AND METHODS

Institutions and Subjects

The 12 participating institutions were clinical centers and generally did not have scientific staff dedicated to nuclear medicine software or hardware development. Standard, vendor-supplied software was used for the collection of the studies, with unmodified scanners and collimators clinically used for brain studies. The acquired data were reconstructed with the program package developed for this project. Manufacturers and models of camera systems and the number of detectors and collimators (including fanbeam or parallel hole) used by the institution are listed in Supplemental Table 1 (supplemental materials are available online only at http://jnm.snmjournals.org). All institutions performed experiments on physical phantoms according to the protocol described in the "Phantom Experiment" section. Of the 12 institutions, 9 obtained patient scans, whereas the remaining 3 provided only phantom data. Clinical studies were approved by institutions' ethics committees or followed guidelines for clinical research protocols authorized by the institution. All subjects at each institution gave written informed consent.

The clinical studies were divided into 3 protocols: intrainstitutional, intrasubject reproducibility (reproducibility); comparison with PET (vs. PET); and intrascan consistency of the dual-time-point split-dose (rest–rest). Studies were excluded from the analysis if there was severe patient motion during one of the studies or if there were changes in the condition of the patients between the first and second studies likely to lead to changes in CBF.

Eight institutions (institutions 1, 3, 4, 6, 8, 9, 11, and 12) participated in the reproducibility arm, in which quantitative CBF values measured on separate days were compared. In this arm, all patients experienced unilateral or bilateral stenosis or occlusion in the extracranial internal carotid artery. The patients' ages ranged from 43 to 81 y (mean ± SD, 65 ± 9 y). A total of 31 studies in this protocol were analyzed. Four patients had to be excluded from the analysis—2 because of significant changes in their pathophysiologic status between the studies and 2 because of severe motion and mispositioning in the scanner.

One institution (institution 4) performed the versus-PET studies. CBF values obtained by the DTARG method were compared with those by ^{15}O-water and PET. Studies were performed on 6 patients (5 men, 1 woman; age range, 71–74 y; mean age ± SD, 72 ± 1 y) with stenosis or occlusion of the extracranial internal carotid artery unilaterally (n = 3) or bilaterally (n = 3).

Two institutions (institutions 2 and 12) provided data for the rest–rest comparison. Five patients from institution 2 had chronic cerebral infarction, whereas 4 subjects from institution 12 had no sign of cerebral disease. Patients' ages ranged from 32 to 72 y (mean ± SD, 52 ± 15 y); 5 patients were men and 4 women.

Phantom Experiment

Three experiments were performed by each institution using the SPECT camera fitted with the collimators normally used in clinical brain studies. The first scan determined the absolute sensitivity or the becquerel calibration factor (BCF) of the reconstructed images. For 10 min, a 360° projection set was acquired of a syringe filled with a ^{123}I-iodoamphetamine solution of known radioactivity and placed at the center of the field of view. The syringe was supplied by Nihon-Medi Physics, and its radioactivity was calibrated to 111 MBq at noon on the day before the experiment, with an accuracy better than 3%, decaying to approximately 30 MBq at the time of the experiment, avoiding the dead time of the camera. The BCF was determined by dividing the absolute radioactivity by the total counts for the syringe region in the reconstructed image.

The second experiment determined the collimator septal penetration contribution (*24*) from high-energy photons into the primary 159-keV energy window for ^{123}I. A line-spread function was obtained from the projection data of a line source filled with ^{123}I-iodoamphetamine. The septal penetration was determined from the background level as described previously (*19*). A projection line-spread function was also generated from this line source placed in a water-filled cylindric phantom (diameter, 16 cm).

The third experiment used a 16-cm-diameter, 15-cm-long uniform cylindric phantom. The whole radioactivity used for the BCF determination was diluted into the phantom, and projection data were acquired for 30 min, using the clinical scan protocols described in the "Clinical Studies" section. The radioactivity concentration (counting rate per unit mass) of an approximately 0.3-mL sample from the phantom was measured using the well counters available at the various institutions. Both NaI- and plastic scintillator–based well counters were used (Supplemental Table

1). Average pixel counts derived from regions of interest on the reconstructed emission images were referred to the well counter radioactivity counting rate, to determine the cross-calibration factor between the SPECT images and well counter system. This cross-calibration factor was subsequently used for the blood sample counts of the clinical studies. Uniformity of the reconstructed emission images was evaluated.

Clinical Studies

All clinical SPECT studies followed the DTARG protocol, with dual administration of iodoamphetamine (*23*), depicted in Figure 1. Briefly, 2 dynamic scans were acquired in quick succession, with a 2-min interval between the scans. The first scan covered the initial 0- to 28-min period, and the second was acquired from 30 to 58 min. At 4 min per frame, 7 frames covered each of the 2 dynamic scan periods. ^{123}I-iodoamphetamine (111 MBq at institutions 2–12 or 167 MBq at institution 1) was infused twice over 1 min into the antecubital vein at 0 and 30 min. Acetazolamide (17 mg/kg, 1,000 mg maximum) was administered intravenously at 20 min after the first iodoamphetamine injection, corresponding to 10 min before the second iodoamphetamine injection. Projection data were summed for the acquisition duration of the first and second scans and reconstructed as described in the "QSPECT Reconstruction" section. In contrast to the study of Kim et al. (*23*), which used full arterial blood sampling, the individual arterial input functions were derived from a population-based standardized input function scaled with the whole-blood counts from a single arterial blood sample taken at approximately 10 min (*1,25–28*). This sample was also used for arterial blood gas analysis.

In the reproducibility arm, an additional, non-DTARG CBF study was performed on a separate day. Instead of DTARG, the previously reported ^{123}I-IMP autoradiographic (IMPARG) method (*1,19,25*) was performed within a month of the DTARG study. The IMPARG method is essentially equivalent to the present DTARG method, except that the IMPARG method uses a single iodoamphetamine administration to assess CBF either at rest or after acetazolamide challenge. The same image reconstruction process as for the DTARG protocol was used. In 12 studies, the DTARG protocol was used instead of IMPARG—namely, the DTARG study was performed twice to assess the CBF reproducibility at rest and after acetazolamide.

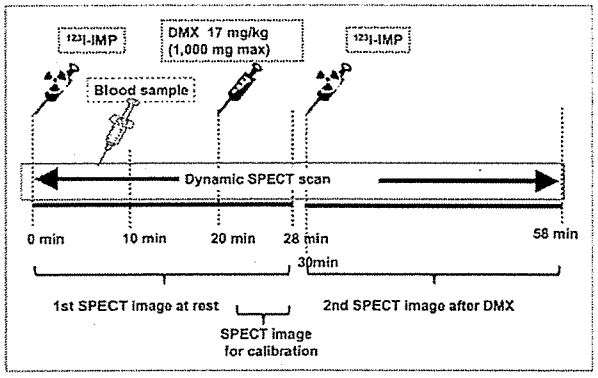

FIGURE 1. Scanning protocol flow for DTARG procedure. ^{123}I-iodoamphetamine was injected at 0 min, and 28-min resting dynamic SPECT scan was commenced. Blood sample for calibration of population input function was drawn at 10 min. Acetazolamide (DMX-diamox) was administered at 20 min. CBF values are scaled by last frame (time, 24–28 min). Second dynamic SPECT scan followed second injection of ^{123}I-iodoamphetamine at 30 min. IMP = iodoamphetamine.

In the versus-PET protocol, the PET study was performed within 2 d of the DTARG SPECT study. PET scans used intravenous ^{15}O-water both at rest and after the acetazolamide challenge. CBF images were calculated by the ^{15}O-water autoradiography technique (*29*), with careful corrections for delay and dispersion (*30–32*). Patients were stable between the SPECT and PET studies.

In the rest–rest protocol, the DTARG scan was obtained without the pharmacologic challenge during the study to evaluate the consistency of CBF values estimated from the 2 scans.

QSPECT Reconstruction

The program package for QSPECT uses a wrapper written in JAVA to run several programs written in C for Microsoft Windows systems. The package includes programs for reconstructing SPECT images, calculating functional images, coregistering images, and reslicing and printing summary logs.

The QSPECT package reconstructs images from the original projection data from commercial SPECT equipment, based on previous work by Iida and his colleagues (*19–21,23,33,34*). Reconstructed SPECT images are calibrated in Bq/mL, which provides independence from scanning parameters such as the acquisition time, number of views, matrix size, and zoom factor. Uniformity and center-of-rotation corrections and fanbeam–to–parallel beam conversion (for fanbeam collimators) were performed using the clinical routine software before reconstruction by this package.

An overall flow diagram of the correction and reconstruction process is shown in Supplemental Figure 1. The OSEM reconstruction technique includes attenuation correction (*17*). A threshold-based edge-detection algorithm generated the attenuation μ-map, assuming a uniform attenuation coefficient of 0.166 cm^{-1} for ^{99m}Tc (0.160 cm^{-1} for ^{123}I) as an average over the brain and skull (*19*). The threshold was optimized via the user interface to correctly define the brain outline. The attenuation μ-map was generated from the summed 0- to 28-min rest frame and was coregistered to the other images (*35*) reconstructed with filtered backprojection without attenuation or scatter correction. The attenuation μ-maps were forward projected to provide the transmission projection data for TDCS. The emission projections were scatter-corrected by the TDCS method, as originally proposed by Meikle et al. (*18*), and further optimized for realistic ^{99m}Tc, ^{201}Tl, and ^{123}I data in the brain and thorax regions (*20,21,23,33,34*). An offset compensated for the septal penetration of high-energy photons for ^{123}I studies, which adds fairly uniform background counts, or direct current (DC) components, to the projections.

Scatter- and attenuation-corrected images were reconstructed with OSEM (5 iterations, 5 subsets using geometric-mean projections, postreconstruction gaussian filter of 7 mm in full width at half maximum) and then realigned to the image set obtained from the first scan. The acquisition parameters and BCF were used to convert the reconstructed raw counts to Bq/mL.

The global CBF over the entire gray matter was estimated from the SPECT frame covering 24–28 min, because this timing minimizes the individual shape variations in individual input function. The look-up table generated for estimating CBF images from the complete dynamic study (0–28 min) was then

scaled to provide global cortical gray matter CBF values consistent with the 24- to 28-min frame estimates. A careful detection algorithm was used to reliably exclude extracranial accumulation of ^{123}I-iodoamphetamine (e.g., in the parotid region), which could adversely affect this scaling procedure. The regional CBF was then estimated at each pixel by means of the table look-up procedure (*25,28*). The background image at the time of the second ^{123}I-iodoamphetamine injection was estimated from the first-phase CBF images, according to the compartment model assumed in this study (*23*). An additional table look-up procedure was applied to the second dynamic dataset (30–58 min) for calculating the vasodilated (acetazolamide challenge) CBF images as described previously (*23*). The data were successfully reconstructed, and CBF was estimated at each institution. To facilitate and provide consistent analysis, the data presented are from the reanalysis conducted at the core lab (National Cerebral and Cardiovascular Center).

Data Analysis

The uniform phantom SPECT activity estimates were compared with the known activity in the phantom. Images for the baseline study were displayed with subsequent images using an absolute flow value scale to visually ascertain regional and global differences in flow. Regions of interest were placed on the middle cerebral artery territories of both hemispheres, and the average flow values between the different methods were compared and plotted. Bland–Altman plots and the SD of the differences evaluated the consistency of CBF values obtained from the reproducibility and versus-PET protocols.

All data were presented as mean ± SD. Pearson correlation analysis and linear regression analysis were used to evaluate relationships between the 2 CBF values. A P value less than 0.05 was considered statistically significant.

RESULTS

Phantom Studies

In the 16-cm scattering cylinder line source experiment, the scatter-uncorrected images show background counts extending beyond the phantom, from septal penetration of the high-energy photons. The scatter correction is largely effective in correcting for scatter and septal penetration counts. As shown in Supplemental Figure 2, the Toshiba-ECAM low- to medium-energy general-purpose (LMEGP) collimator, designed for reduced ^{123}I septal penetration, compared with the standard low-energy high-resolution collimator (GE Healthcare), demonstrates reduced scatter and septal penetration counts. The lower septal penetration of the Toshiba-ECAM LMEGP collimators is also supported by a lowered scatter correction offset value (DC = 0.05, compared with DC = 0.20 for the GE low-energy high-resolution collimator). The reduced scatter and septal penetration result in more complete removal of scatter for the LMEGP collimator.

Figure 2 displays reconstructed slices of the uniform phantom for all 12 institutions, scaled to the same maximum activity concentration. The estimated activity concentrations from these studies, compared with the known activity concentration, represented an accuracy of 87.5% ± 5.1% (Supplemental Table 1). The well counter–to–SPECT cross-calibration factor, which represents the sensitivity of the well counter system for ^{123}I, was 0.5–1.0 for NaI systems and 0.1–0.2 for plastic scintillation detector systems. The BCF values were consistent for the same SPECT camera–collimator configurations.

Clinical Studies

Figure 3A shows typical CBF images obtained at 4 institutions with 4 different γ-camera vendors, performed as part of the reproducibility arm of the study. Each case shows different CBF distributions both at rest and after acetazolamide challenge. The acetazolamide images obtained using the DTARG method agree well with the images subsequently obtained with the IMPARG method after acetazolamide infusion.

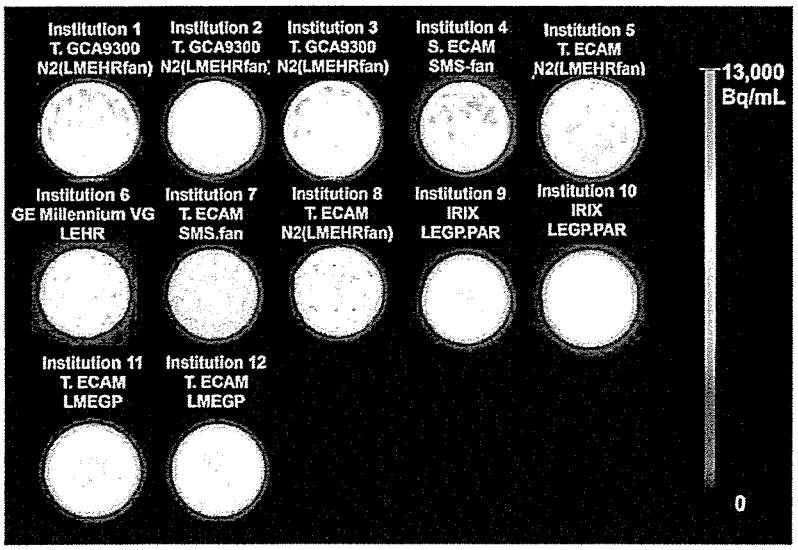

FIGURE 2. Reconstructed slices through uniform phantom from the participating 12 institutions. Experiment was designed to have same phantom activity concentration for each center's study. Nonuniformities and also differences in absolute activity concentration estimates can be observed, highlighting need for rigorous calibration, flood correction, and quality control. Legend above each image gives institution number (given in Supplemental Table 1), γ-camera model, and collimator used.

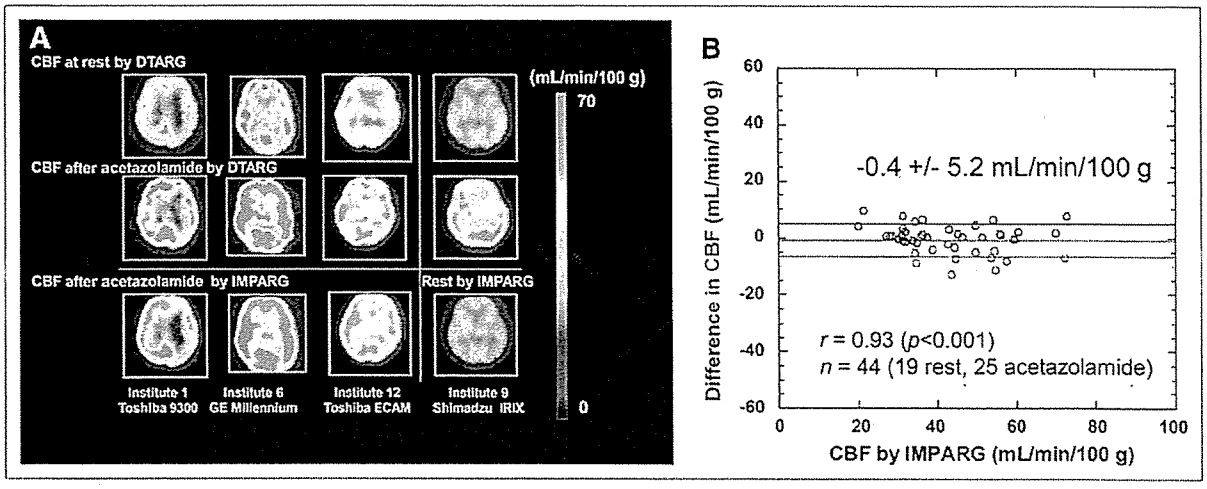

FIGURE 3. (A) Images from reproducibility study. CBF images obtained at rest and after acetazolamide with DTARG method. Repeated scan (third row) within 1 mo using IMPARG method and acetazolamide stress (columns 1–3) and at rest (last column). Images demonstrate that CVR can be estimated with this technique and demonstrate good reproducibility of measuring both at rest and after acetazolamide challenge CBF. (B) Bland–Altman plot showing difference vs. IMPARG CBF values estimated from DTARG method and repeated IMPARG studies to assess reproducibility. Little systematic bias is detected (mean difference, −0.4 mL/100 g/min), and SD of differences is moderate (5.2 mL/100 g/min). Correlation coefficient of $r = 0.93$ ($P < 0.001$) was found.

CBF images of a subject with left middle cerebral artery occlusion are shown in Supplemental Figure 3 for slices covering the whole brain. The images demonstrate reduced CBF after acetazolamide challenge in the left middle cerebral artery territory. The good reproducibility is confirmed by the Bland–Altman plot comparison of DTARG CBF values, with the CBF values obtained at a different imaging session with IMPARG or DTARG (Fig. 3B). The SD of the differences is 5.2 mL/100 g/min, with low bias supported by the mean difference of 0.4 mL/100 g/min. Regression analysis between DTARG and IMPARG values yielded a significant correlation ($P < 0.001$), with a correlation coefficient of $r = 0.93$.

Figure 4A shows MR and CBF images at rest and after acetazolamine obtained with DTARG SPECT and ^{15}O-water PET in a 73-y-old male patient (63 kg) with right internal carotid artery occlusion and left internal carotid stenosis. The MR images do not show any evidence of cerebral infarction in either hemisphere. Rest CBF was reduced bilaterally in the frontal-to-parietal regions, and acetazolamide increased CBF in left parietal regions but not in the right parietal area. DTARG CBF indicated the loss of vasoreactivity in the right internal carotid artery stenotic area. These findings were consistent with those from the PET evaluation. An additional example is shown in Supplemental Figure 4 for a 74-y-old female patient (48 kg) with left internal carotid artery stenosis, for whom MR images did not show cerebral infarction. DTARG CBF demonstrated preserved CBF in both hemispheres but reduced CBF reactivity in the left middle cerebral artery territory. The findings were again consistent with those from PET. Figure 4B compares the flow values obtained at rest and after acetazolamide with DTARG with the corresponding values obtained by ^{15}O-water PET. The SD of the differences is 5.1 mL/100 g/min, with the significant underestimation by ^{15}O-water PET, compared with PET by the DTARG method, highlighted by a mean difference of −6.1 mL/100 g/min. The Pearson analysis showed a significant correlation ($P < 0.001$), with a correlation coefficient of $r = 0.88$.

The results from the rest–rest protocol are summarized in Figure 5. The differences between the measurements performed with the 2 injections were small, with good agreement between the 2 flow values. The mean ± SD of the differences was 0.6 ± 2.9 mL/100 g/min.

DISCUSSION

The QSPECT package provided quantitative images consistent between the participating centers, using dual- or triple-detector SPECT scanners and collimators routinely used for nonquantitative brain studies. All centers successfully acquired the dynamic SPECT images, and the data from the variety of cameras encountered were successfully processed by the software package. Rest CBF and CVR could be readily obtained by the participating institutions in a single, clinically practical, 1-h scanning session. Good reproducibility of CBF estimates was observed in 31 pairs of studies at 8 institutions (Fig. 3), and the CBF estimated with the ^{123}I-iodoamphetamine SPECT agreed well with ^{15}O-water PET CBF at 1 institution (Fig. 4). The CBF values after the second injection of the DTARG were consistent with the values obtained after the

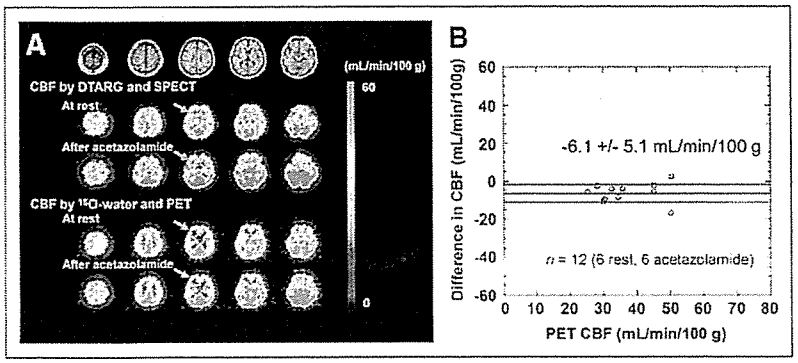

FIGURE 4. (A) MR and CBF images at rest and after acetazolamide stress assessed with corresponding measurements with ^{15}O-water PET (vs. PET evaluation) in patient with right internal carotid artery occlusion and left internal carotid stenosis. Gaussian filter was not applied to SPECT CBF in this display. (B) Bland–Altman plot. Moderate underestimation of CBF determined by DTARG method, compared with PET, is observed (mean difference, −6.1 mL/100 g/min). Correlation coefficient of $r = 0.88$ ($P < 0.001$) was found.

first injection when no vasodilating stress was given in 9 studies at 2 institutions (Fig. 5).

Quantitative CBF and CVR in response to acetazolamide challenge can be of significant prognostic value for patients considered for revascularization of cerebral arteries (*5–7*). The previously validated IMPARG method requires 2 independent scans on different days to assess the CVR (*5–7*), limiting it for routine clinical studies. The DTARG protocol to quantitatively assess CBF both at rest and after acetazolamide from a single dynamic SPECT session with the dual administration of ^{123}I-iodoamphetamine (*23*) facilitates clinical use. Errors caused by ambiguity in the absolute scaling, and possible changes in physiologic status of the subjects between scans, can be reduced substantially with the DTARG protocol. The quantitative reconstruction program enabled the compartment model–based kinetic analysis to compensate for the residual radioactivity concentration during the second session of the dynamic scan.

Major error sources in SPECT, namely attenuation and scatter, are only object-dependent (*14*) and not γ-camera– or collimator-dependent, and thus SPECT images obtained by this quantitative reconstruction package should be consistent across systems. Septal penetration of high-energy photons for ^{123}I is, however, collimator-dependent (*24*) but could be compensated as part of the TDCS scatter correction algorithm (*11*), as demonstrated in Supplemental Figure 2. The radioactivity concentration of the uniform cylinder phantom estimated in units of Bq/mL was consistent and showed variation within ±5.1% (Fig. 2; Supplemental Table 1), though a systematic underestimation by 12.5%, which is attributed to the BCFs being derived from a line source in air, reconstructed without scatter, attenuation, and septal penetration corrections. However, this underestimation does not affect the CBF estimation, because it relies on the direct cross-calibration between the γ-counter used to count the blood sample and the SPECT measurements.

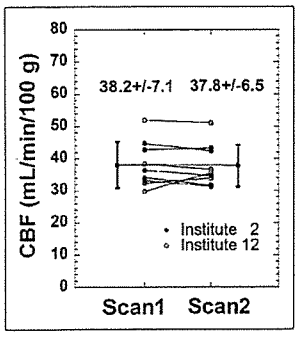

FIGURE 5. Results from rest–rest evaluation carried out at 2 institutions (2 and 12). In this study, DTARG method was performed as per normal protocol but without pharmacologic stress. CBFs estimated with first injection (left on graph) are in good agreement with those estimated after second injection (right on graph).

This phantom study also highlighted the importance of proper calibration and quality control of the γ-camera to avoid artifacts and bias in the reconstructed images. These corrections were applied, as for other clinical studies, by the vendors' software rather than as part of the QSPECT system, because these corrections are typically performed online and on-the-fly, with only the corrected data being stored. The nonuniformities seen on some phantom images should improve with more rigorous quality-control procedures.

The previously validated population-based input function requiring only a single arterial blood sample for scaling (*1,25–28*) has been incorporated in the software package. Blood from this single arterial sample is also used to measure arterial blood gases, which are relevant and of interest clinically in these patients. The timing of the single blood sample (~10 min after iodoamphetamine injection) was optimized previously (*1,25–28*) to minimize the errors associated with individual differences in shape of the arterial input function. In addition, absolute global CBF was estimated from SPECT images taken at an optimized mid scan time of approximately 30 min (24–28 min), rather than from the initial part of the study, to maximize the accuracy of using the population-based input function (*1,25–28*).

Partial-volume correction has not been implemented as part of this processing protocol. Partial-volume effects can potentially lead to underestimation of flow values in gray matter regions because of the limited resolution of SPECT. The small underestimation of 6.1 mL/100 g/min by the DTARG method, compared with ^{15}O-water PET (Fig. 4B), is attributed to the partial-volume effects due to differences in resolution between PET and SPECT. The underestimation can also lead to variations in CBF values obtained with different-

resolution collimators. However, consistent postreconstruction filtering, as applied in this study, can reduce this effect.

Only the reproducibility within an institution was assessed. Hence, the reproducibility of measurements between institutions cannot be gleaned from these data, particularly because patients with vascular disease were studied. Thus, unlike estimates from healthy volunteers, flow values and vascular reactivity are expected to vary from patient to patient, and flow values determined at one institution with one group of patients are therefore not directly comparable with flow values from another group of patients in another institution. A realistic brain phantom, such as recently developed by our group, simulating head contour with bone attenuation, could be used to assess the consistency of brain images between institutions.

CONCLUSION

The developed QSPECT package allows absolute CBF and CVR to be estimated in routine clinical studies. This multicenter study has demonstrated the applicability of QSPECT for a variety of clinical settings and equipment. Results from the studies suggest that a change of approximately 10% or 5 mL/min/100 g can be readily detected in follow-up studies. The graphical user interface for easily controlling the in-built sophisticated programs and tools ensures that routine use does not require dedicated support from scientific or computing staff. The package is now successfully used in over 130 institutions in Japan, and more than 25,000 patient studies have been analyzed with the QSPECT package.

ACKNOWLEDGMENTS

We thank the staff of each of the following institutions that participated in this project for their invaluable help with supporting the SPECT studies: Azabu Neurosurgical Hospital, Sapporo City; Asahikawa Red Cross Hospital, Asahikawa City; Handa City Hospital, Handa City; Ichinomiya Municipal Hospital, Ichinomiya City; Kashiwaba Neurosurgical Hospital, Sapporo City; Japanese Red Cross Kobe Hospital, Kobe City; Nakamura Memorial Hospital, Sapporo City; National Cardiovascular Center, Osaka; Ogori Daiichi General Hospital, Yamaguchi City; Oji General Hospital, Tomakomai City; Sunagawa City Medical Center, Sunagawa City; and Teine Keijinkai Hospital, Sapporo City. The present study was supported by the Japan Cardiovascular Research Foundation and a grant for Translational Research from the Ministry of Health, Labor and Welfare (MHLW), Japan.

REFERENCES

1. Iida H, Akutsu T, Endo K, et al. A multicenter validation of regional cerebral blood flow quantitation using [^{123}I]iodoamphetamine and single photon emission computed tomography. *J Cereb Blood Flow Metab.* 1996;16:781–793.
2. Hatazawa J, Iida H, Shimosegawa E, Sato T, Murakami M, Miura Y. Regional cerebral blood flow measurement with iodine-123-IMP autoradiography: normal values, reproducibility and sensitivity to hypoperfusion. *J Nucl Med.* 1997;38:1102–1108.
3. Yamaguchi T, Kanno I, Uemura K, et al. Reduction in regional cerebral metabolic rate of oxygen during human aging. *Stroke.* 1986;17:1220–1228.
4. Ogasawara K, Ito H, Sasoh M, et al. Quantitative measurement of regional cerebrovascular reactivity to acetazolamide using ^{123}I-*N*-isopropyl-*p*-iodoamphetamine autoradiography with SPECT: validation study using $H_2{}^{15}O$ with PET. *J Nucl Med.* 2003;44:520–525.
5. Ogasawara K, Ogawa A, Terasaki K, Shimizu H, Tominaga T, Yoshimoto T. Use of cerebrovascular reactivity in patients with symptomatic major cerebral artery occlusion to predict 5-year outcome: comparison of xenon-133 and iodine-123-IMP single-photon emission computed tomography. *J Cereb Blood Flow Metab.* 2002;22:1142–1148.
6. Ogasawara K, Ogawa A, Yoshimoto T. Cerebrovascular reactivity to acetazolamide and outcome in patients with symptomatic internal carotid or middle cerebral artery occlusion: a xenon-133 single-photon emission computed tomography study. *Stroke.* 2002;33:1857–1862.
7. Ogasawara K, Ogawa A. JET study (Japanese EC-IC Bypass Trial) [in Japanese]. *Nippon Rinsho.* 2006;64(suppl 7):524–527.
8. Fujita M, Ichise M, Zoghbi SS, et al. Widespread decrease of nicotinic acetylcholine receptors in Parkinson's disease. *Ann Neurol.* 2006;59:174–177.
9. Deloar HM, Watabe H, Kudomi N, Kim KM, Aoi T, Iida H. Dependency of energy and spatial distributions of photons on edge of object in brain SPECT. *Ann Nucl Med.* 2003;17:99–106.
10. Iida H, Eberl S, Kim KM, et al. Absolute quantitation of myocardial blood flow with ^{201}Tl and dynamic SPECT in canine: optimisation and validation of kinetic modelling. *Eur J Nucl Med Mol Imaging.* 2008;35:896–905.
11. Iida H, Eberl S. Quantitative assessment of regional myocardial blood flow with thallium-201 and SPECT. *J Nucl Cardiol.* 1998;5:313–331.
12. Eberl S, Chan HK, Daviskas E, Constable C, Young I. Aerosol deposition and clearance measurement: a novel technique using dynamic SPET. *Eur J Nucl Med.* 2001;28:1365–1372.
13. Hapdey S, Soret M, Ferrer L. Quantification in SPECT: myth or reality? A multicentric study. *IEEE Nucl Sci Symp Conf Rec.* 2004;5:3170–3317.
14. Graham LS, Fahey FH, Madsen MT, van Aswegen A, Yester MV. Quantitation of SPECT performance: report of Task Group 4, Nuclear Medicine Committee. *Med Phys.* 1995;22:401–409.
15. Hendel RC, Corbett JR, Cullom SJ, DePuey EG, Garcia EV, Bateman TM. The value and practice of attenuation correction for myocardial perfusion SPECT imaging: a joint position statement from the American Society of Nuclear Cardiology and the Society of Nuclear Medicine. *J Nucl Cardiol.* 2002;9:135–143.
16. Zaidi H, Koral KF. Scatter modelling and compensation in emission tomography. *Eur J Nucl Med Mol Imaging.* 2004;31:761–782.
17. Hudson HM, Larkin RS. Accelerated image reconstruction using ordered subsets of projection data. *IEEE Trans Med Imaging.* 1994;13:601–609.
18. Meikle SR, Hutton BF, Bailey DL. A transmission-dependent method for scatter correction in SPECT. *J Nucl Med.* 1994;35:360–367.
19. Iida H, Narita Y, Kado H, et al. Effects of scatter and attenuation correction on quantitative assessment of regional cerebral blood flow with SPECT. *J Nucl Med.* 1998;39:181–189.
20. Narita Y, Eberl S, Iida H, et al. Monte Carlo and experimental evaluation of accuracy and noise properties of two scatter correction methods for SPECT. *Phys Med Biol.* 1996;41:2481–2496.
21. Narita Y, Iida H, Eberl S, Nakamura T. Monte Carlo evaluation of accuracy and noise properties of two scatter correction methods for ^{201}Tl cardiac SPECT. *IEEE Trans Nucl Sci.* 1997;44:2465–2472.
22. Willowson K, Bailey DL, Baldock C. Quantitative SPECT reconstruction using CT-derived corrections. *Phys Med Biol.* 2008;53:3099–3112.
23. Kim K, Watabe H, Hayashi T, et al. Quantitative mapping of basal and vasareactive cerebral blood flow using split-dose ^{123}I-idoamphetamine and single photon emission computed tomography. *Neuroimage.* 2006;33:1126–1135.
24. Kim KM, Watabe H, Shidahara M, Ishida Y, Iida H. SPECT collimator dependency of scatter and validation of transmission dependent scatter compensation methodologies. *IEEE Trans Nucl Sci.* 2001;48:689–696.
25. Iida H, Itoh H, Nakazawa M, et al. Quantitative mapping of regional cerebral blood flow using iodine-123-IMP and SPECT. *J Nucl Med.* 1994;35:2019–2030.
26. Iida H, Nakazawa M, Uemura K. Quantitation of regional cerebral blood flow using 123I-IMP from a single SPECT scan and a single blood sampling: analysis on statistical error source and optimal scan time [in Japanese]. *Kaku Igaku.* 1995;32:263–270.
27. Kurisu R, Ogura T, Takikawa S, Saito H, Nakazawa M, Iida H. Estimation and optimization of the use of standard arterial input function for split-dose administration of *N*-isopropyl-*p*[^{123}I]iodoamphetamine [in Japanese]. *Kaku Igaku.* 2002;39:13–20.

28. Ogura T, Takikawa S, Saito H, Nakazawa M, Shidahara M, Iida H. Validation and optimization of the use of standardized arterial input function in *N*-isopropyl-*p*[^{123}I]iodoamphetamine cerebral blood flow SPECT [in Japanese]. *Kaku Igaku.* 1999;36:879–890.
29. Shidahara M, Watabe H, Kim KM, et al. Evaluation of a commercial PET tomograph-based system for the quantitative assessment of rCBF, rOEF and $rCMRO_2$ by using sequential administration of ^{15}O-labeled compounds. *Ann Nucl Med.* 2002;16:317–327.
30. Iida H, Higano S, Tomura N, et al. Evaluation of regional differences of tracer appearance time in cerebral tissues using [^{15}O] water and dynamic positron emission tomography. *J Cereb Blood Flow Metab.* 1988;8:285–288.
31. Iida H, Kanno I, Miura S, Murakami M, Takahashi K, Uemura K. Error analysis of a quantitative cerebral blood flow measurement using $H_2{}^{15}O$ autoradiography and positron emission tomography, with respect to the dispersion of the input function. *J Cereb Blood Flow Metab.* 1986;6:536–545.
32. Iida H, Kanno I, Miura S, Murakami M, Takahashi K, Uemura K. A determination of the regional brain/blood partition coefficient of water using dynamic positron emission tomography. *J Cereb Blood Flow Metab.* 1989;9:874–885.
33. Iida H, Shoji Y, Sugawara S, et al. Design and experimental validation of a quantitative myocardial ^{201}Tl SPECT System. *IEEE Trans Nucl Sci.* 1999;46:720–726.
34. Narita Y, Iida H. Scatter correction in myocardial thallium SPECT: needs for optimization of energy window settings in the energy window-based scatter correction techniques [in Japanese]. *Kaku Igaku.* 1999;36:83–90.
35. Eberl S, Kanno I, Fulton RR, Ryan A, Hutton BF, Fulham MJ. Automated interstudy image registration technique for SPECT and PET. *J Nucl Med.* 1996;37:137–145.

Clinical Chemistry 56:7
1183–1185 (2010)

Brief Communications

Plasma MicroRNA 499 as a Biomarker of Acute Myocardial Infarction

Taichi Adachi,[1] Michio Nakanishi,[1] Yoritaka Otsuka,[1] Kunihiro Nishimura,[2] Gou Hirokawa,[2] Yoichi Goto,[1] Hiroshi Nonogi,[1] and Naoharu Iwai[1,2*]
Departments of [1] Cardiology and [2] Epidemiology, National Cardiovascular Center, Suita, Osaka, Japan; * address correspondence to this author at: Department of Epidemiology, National Cardiovascular Center, 5-7-1 Fujishirodai, Suita, Osaka 565-8565, Japan. Fax +81-6-6835-2077; e-mail iwai@ri.ncvc.go.jp.

BACKGROUND: MicroRNAs (miRNAs) are endogenous small RNAs 21–25 nucleotides in length. Recently, we reported that miRNA 208 (miR-208) is produced exclusively in the rat myocardium and that plasma miR-208 is a biomarker of myocardial injury in rats. In the present study, we assessed the hypothesis that plasma concentrations of myocardial-specific miRNAs can be used to diagnose myocardial injury in humans.

METHODS: We used array analysis of miRNA production in various human tissues to identify heart-specific miRNAs. We assessed the plasma concentrations of miR-499 in 14 individuals with acute coronary syndromes, 15 individuals with congestive heart failure, and 10 individuals without cardiovascular diseases. Plasma miR-499 concentrations were measured with a real-time reverse-transcription PCR method that used an artificial small RNA as an internal calibrator.

RESULTS: The miRNA array analysis of various human tissues indicated that miR-499 was produced almost exclusively in the heart. Plasma miR-499 concentrations were measurably increased in all individuals with acute myocardial infarction but were below the limit of detection for all individuals in the other patient groups.

CONCLUSIONS: The plasma concentration of miR-499 may be a useful biomarker of myocardial infarction in humans.

MicroRNAs (miRNAs),[3] endogenous small RNAs 21–25 nucleotides in length, can pair with the 3′ untranslated region sites in mRNAs of protein-coding genes to downregulate their expression *(1)*, and they play important roles in various physiological and pathologic processes *(2, 3)*. More than 500 human miRNAs have been identified *(4)*, and most human protein-coding genes appear to be targeted by these miRNAs *(5, 6)*. miRNAs appear to function as rheostats to fine-tune adjustments in the protein output *(7, 8)*.

The presence of miRNAs in various body fluids has recently been reported *(9–11)*, and we recently reported that the plasma concentration of miRNA 208 (miR-208), a myocardial-specific miRNA in rats, is a useful biomarker of myocardial injury *(12)*. Other groups have also reported that plasma miRNAs are sensitive and specific biomarkers of various tissue injuries *(13, 14)*. In the present study, we examined which human tissues produced miR-499 and assessed whether the plasma concentration of miR-499 is a useful biomarker of myocardial injury in humans.

We collected blood samples from 29 inpatients and 10 healthy asymptomatic outpatients at the National Cardiovascular Center Hospital after obtaining their written informed consent. This study was approved by the Ethics Committee of the National Cardiovascular Center.

The acute coronary syndromes group consisted of 9 patients with acute myocardial infarction (AMI) and 5 patients with unstable angina pectoris. All acute coronary syndrome patients underwent coronary angiography and percutaneous coronary intervention. The blood samples from the acute coronary syndrome patients were obtained within 48 h of the last onset of chest pain. We also obtained blood samples from AMI patients before their final discharge when their clinical status was stable. The congestive heart failure (CHF) group consisted of 8 patients with old myocardial infarction [New York Heart Association (NYHA) class III], 4 patients with dilated cardiomyopathy (NYHA class II), and 3 patients with valvular diseases (1 patient in NYHA class III and 2 in NYHA class II). The blood samples of patients in the CHF group were obtained while they were in NYHA functional class II or III. The control individuals consisted of asymptomatic healthy and/or borderline hypertensive outpatients who were visiting the hospital for regular health checkups. Creatine kinase MB was increased in the patients with AMI and not in the patients with unstable angina pectoris (Table 1).

We isolated total plasma RNA with the mirVana™ PARIS Kit (Ambion) according to the manufacturer's protocol. Before purification, we added a fixed amount of a small synthetic RNA to the plasma samples for a dual assay to verify the RNA-purification procedures. Details of the procedure are described in the Supplemental Data file available in the Data Supplement that accompanies the online version of this Brief Communication at http://www.clinchem.org/content/vol56/issue7.

[3] Nonstandard abbreviations: miRNA, microRNA; miR-208, miRNA 208; AMI, acute myocardial infarction; CHF, congestive heart failure; NYHA, New York Heart Association.

Table 1. Patient characteristics.[a]

	AMI[b] (n = 9)	UAP (n = 5)	CHF_III (n = 9)	CHF_II (n = 6)	Normal (n = 10)
F/M sex, n	3/6	2/3	2/7	2/4	5/5
Age, years	66.8 (9.28)	70.2 (16.2)	71.6 (6.6)	61.5 (16.4)	41.5 (8.0)
CKMB, U/L[c]	122.2 (124.9)	18.9 (6.6)	ND	ND	ND
BNP, ng/L[c]	ND	ND	674 (341)	175 (142)	ND
Log miR-499 copies/100 μL	4.19 (0.24)	<2.38	<2.38	<2.38	<2.38

[a] Data are expressed as the mean (SD) where indicated.
[b] AMI, acute myocardial infarction; UAP, unstable angina pectoris; CHF_III, congestive heart failure in NYHA class III; CHF_II, congestive heart failure in NYHA class II; Normal, healthy control individuals; CKMB, creatine kinase MB; BNP, brain natriuretic peptide; ND, not determined.
[c] CKMB (reference interval, 0–23 U/L) and BNP (reference interval, <18.4 ng/L) were measured in the AMI groups (AMI and UAP) and the CHF groups, respectively.

To identify myocardial-specific miRNAs, we used the ABI TaqMan MicroRNA Array kit (Applied Biosystems) according to the manufacturer's protocol for profiling the production of miRNAs in various human tissues and cultured cells.

To measure miR-499 concentrations, we used a TaqMan microRNA real-time RT-PCR kit (Applied Biosystems) *(15)* according to the manufacturer's protocol. We simultaneously assessed the concentration of the internal reference small RNA in a single tube. The limit of detection for miR-499 was 240 copies/100 μL. All assays were performed in duplicate. Calibration assays with various amounts of synthetic miR-499 were performed on each assay plate. Details of the statistical analyses are described in the Supplemental Data file in the online Data Supplement.

The miRNA array analyses of 671 species of miRNAs in various tissues and cells indicated that miR-499 is produced almost exclusively in the human heart (see Supplemental Table in the online Data Supplement). miR-208a and miR-208b concentrations appear to be very low in the human heart (see Supplemental Table in the online Data Supplement), and these 2 miRNAs appear not to be useful as plasma biomarkers.

Fig. 1 summarizes the data for plasma miR-499 concentrations in the study population. Plasma miR-499 concentrations were below the limit of detection in the control and CHF groups; however, plasma miR-499 concentrations were measurably increased in patients with AMI in the acute phase (within 48 h of the last onset of chest pain) and became undetectable before hospital discharge, whereas this miRNA was not detected in the plasma of patients with unstable angina pectoris. The large variation in the plasma miR-499 concentration in AMI patients was most likely related to variation in the time of blood collection. Our preliminary investigation indicated that the peak plasma miR-499 concentration occurred between 6 h and 12 h of the onset of myocardial infarction (data not shown). A positive correlation between creatine kinase MB activity and plasma miR-499 concentration was clearly

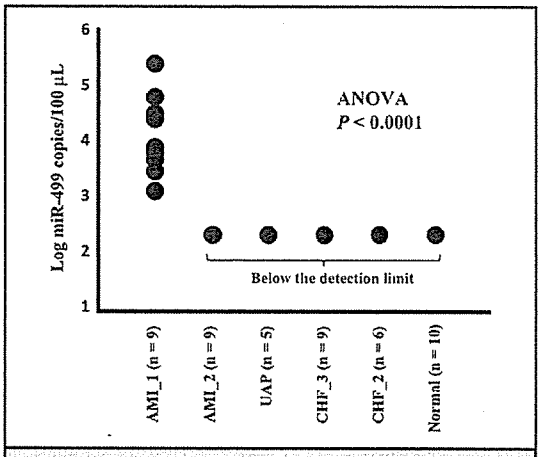

Fig. 1. Plasma concentrations of miR-499 in the study population.

Plasma miR-499 concentrations were assessed by real-time reverse-transcription PCR with a synthetic miRNA included as an internal calibrator. Values are expressed as log miR-499 copies/100 μL. Concentrations were measured in patients with AMI [repeatedly measured in samples obtained within 48 h (AMI_1) and at just before hospital discharge (AMI_2)], in patients with unstable angina pectoris (UAP), in CHF patients in NYHA class III (CHF_3), in CHF patients in NYHA class II (CHF_2), and in healthy control individuals (Normal). An ANOVA indicated that the mean miR-499 values were significantly different among the groups ($P < 0.0001$). The subsequent Dunnett test indicated that values in the AMI_1 group were significantly higher than those of the other groups ($P < 0.0001$ for all comparisons).

observed in individuals with AMI (see Supplemental Data in the online Data Supplement).

The present study is the first to confirm that a cardiac-specific miRNA, miR-499, can be a biomarker of myocardial infarction in humans. The next question is whether this assessment of the plasma miR-499 concentration has any clinical significance. We expected the PCR-based assay of plasma miR-499 to detect possible myocardial micronecrosis in CHF. In fact, our study showed that this method could not detect plasma miR-499 concentrations reliably in CHF patients. A more sensitive assay to detect plasma miR-499 can be developed, however, and it might establish miR-499 as a new biomarker of cardiovascular diseases in the same way that the recently developed high-sensitivity assays for troponins have become very useful for evaluating patients with cardiovascular diseases *(16)*.

Accumulating evidence suggests the usefulness of circulating miRNAs as stable blood-based biomarkers for various diseases *(9–11)*. The present study has confirmed, for the first time, that the plasma miR-499 concentration may be a biomarker of myocardial infarction in humans. Our array data indicate other intriguing candidates for clinical applications, including miR-124a for the central nervous system, miR-122 for the liver, and miR-133a for skeletal muscle. These observations await further clinical investigations.

Author Contributions: *All authors confirmed they have contributed to the intellectual content of this paper and have met the following 3 requirements: (a) significant contributions to the conception and design, acquisition of data, or analysis and interpretation of data; (b) drafting or revising the article for intellectual content; and (c) final approval of the published article.*

Authors' Disclosures of Potential Conflicts of Interest: *No authors declared any potential conflicts of interest.*

Role of Sponsor: The funding organizations played no role in the design of study, choice of enrolled patients, review and interpretation of data, or preparation or approval of manuscript.

Acknowledgments: The National Cardiovascular Center received funds from the Program for the Promotion of Fundamental Studies in Health Science of the National Institute of Biomedical Innovation, Japan.

References

1. Bartel DP. MicroRNAs: genomics, biogenesis, mechanism, and function. Cell 2004;116:281–97.
2. Croce CM. Oncogenes and cancer. N Engl J Med 2008;358:502–11.
3. van Rooij E, Sutherland LB, Qi X, Richardson JA, Hill J, Olson EN. Control of stress-dependent cardiac growth and gene expression by a microRNA. Science 2007;316:575–9.
4. Griffiths-Jones S, Grocock RJ, van Dongen S, Bateman A, Enright AJ. miRBase: microRNA sequences, targets and gene nomenclature. Nucleic Acids Res 2006;34:D140–4.
5. Krek A, Grun D, Poy MN, Wolf R, Rosenberg L, Epstein EJ, et al. Combinatorial microRNA target predictions. Nat Genet 2005;37:495–500.
6. Lewis BP, Burge CB, Bartel DP. Conserved seed pairing, often flanked by adenosines, indicates that thousands of human genes are microRNA targets. Cell 2005;120:15–20.
7. Baek D, Villen J, Shin C, Camargo FD, Gygi SP, Bartel DP. The impact of microRNAs on protein output. Nature 2008;455:64–71.
8. Selbach M, Schwanhausser B, Thierfelder N, Fang Z, Khanin R, Rajewsky N. Widespread changes in protein synthesis induced by microRNAs. Nature 2008;455:58–63.
9. Gilad S, Meiri E, Yogev Y, Benjamin S, Lebanony D, Yerushalmi N, et al. Serum microRNAs are promising novel biomarkers. PLoS One 2008;3:e3148.
10. Chen X, Ba Y, Ma L, Cai X, Yin Y, Wang K, et al. Characterization of microRNAs in serum: a novel class of biomarkers for diagnosis of cancer and other diseases. Cell Res 2008;18:997–1006.
11. Chim SS, Shing TK, Hung EC, Leung TY, Lau TK, Chiu RW, Lo YM. Detection and characterization of placental microRNAs in maternal plasma. Clin Chem 2008;54:482–90.
12. Ji X, Takahashi R, Hiura Y, Hirokawa G, Fukushima Y, Iwai N. Plasma miR-208 as a biomarker of myocardial injury. Clin Chem 2009;55:1944–9.
13. Laterza OF, Lim L, Garrett-Engele PW, Vlasakova K, Muniappa N, Tanaka WK, et al. Plasma microRNAs as sensitive and specific biomarkers of tissue injury. Clin Chem 2009;55:1977–83.
14. Wang K, Zhang S, Marzolf B, Troisch P, Brightman A, Hu Z, et al. Circulating microRNAs, potential biomarkers for drug-induced liver injury. Proc Natl Acad Sci U S A 2009;106:4402–7.
15. Chen C, Ridzon DA, Broomer AJ, Zhou Z, Lee DH, Nguyen JT, et al. Real-time quantification of microRNAs by stem-loop RT-PCR. Nucleic Acids Res 2005;33:e179.
16. Omland T, de Lemos JA, Sabatine MS, Christophi CA, Rice MM. A sensitive cardiac troponin T assay in stable coronary artery disease. N Engl J Med 2009;361:2538–47.

Previously published online at
DOI: 10.1373/clinchem.2010.144121

Clinical Chemistry 56:4
550–558 (2010)

LOX Index, a Novel Predictive Biochemical Marker for Coronary Heart Disease and Stroke

Nobutaka Inoue,[1] Tomonori Okamura,[2] Yoshihiro Kokubo,[2] Yoshiko Fujita,[1] Yuko Sato,[1] Mamoru Nakanishi,[3] Kazuki Yanagida,[3] Akemi Kakino,[1] Shin Iwamoto,[1] Makoto Watanabe,[2] Sayoko Ogura,[1] Kazunori Otsui,[1] Haruo Matsuda,[4] Kagehiro Uchida,[3] Ryo Yoshimoto,[1] and Tatsuya Sawamura[1]*

BACKGROUND: Lectin-like oxidized LDL receptor 1 (LOX-1) is implicated in atherothrombotic diseases. Activation of LOX-1 in humans can be evaluated by use of the LOX index, obtained by multiplying the circulating concentration of LOX-1 ligands containing apolipoprotein B (LAB) times that of the soluble form of LOX-1 (sLOX-1) [LOX index = LAB × sLOX-1]. This study aimed to establish the prognostic value of the LOX index for coronary heart disease (CHD) and stroke in a community-based cohort.

METHODS: An 11-year cohort study of 2437 residents age 30–79 years was performed in an urban area located in Japan. Of these, we included in the analysis 1094 men and 1201 women without history of stroke and CHD. We measured LAB and sLOX-1 using ELISAs with recombinant LOX-1 and monoclonal anti–apolipoprotein B antibody and with 2 monoclonal antibodies against LOX-1, respectively.

RESULTS: During the follow-up period, there were 68 incident cases of CHD and 91 cases of stroke (with 60 ischemic strokes). Compared with the bottom quartile, the hazard ratio (HR) of the top quartile of LOX index was 1.74 (95% CI 0.92–3.30) for stroke and 2.09 (1.00–4.35) for CHD after adjusting for sex, age, body mass index, drinking, smoking, hypertension, diabetes, non-HDL cholesterol, and use of lipid-lowering agents. Compared with the bottom quartile of LOX index, the fully adjusted HRs for ischemic stroke were consistently high from the second to the top quartile: 3.39 (95% CI 1.34–8.53), 3.15 (1.22–8.13) and 3.23 (1.24–8.37), respectively.

CONCLUSIONS: Higher LOX index values were associated with an increased risk of CHD. Low LOX index values may be protective against ischemic stroke.

Therapeutic interventions for dyslipidemia such as hypercholesterolemia have proven their effectiveness for the primary as well as secondary prevention of coronary heart disease (CHD).[5] It is also well known that the risk for CHD is significantly associated with high serum concentrations of LDL cholesterol or low concentrations of HDL cholesterol in both Japanese *(1, 2)* and Western populations *(3)*. In contrast, dyslipidemia has much weaker relationship to stroke than CHD *(4)*. Although the pathogenesis of ischemic stroke and CHD is based largely on atherosclerotic changes of arteries, there is still much unresolved discrepancy.

Oxidized LDL induces a wide variety of cellular responses, such as induction of the expression of adhesion molecules and proinflammatory cytokines, which enhance progression of atherothrombotic cardiovascular diseases. Using antibodies against oxidation-dependent epitopes of LDL, cross-sectional studies reported association of oxidized LDL concentrations with ischemic heart disease, and a cohort study reported association of oxidized LDL with metabolic syndrome *(5–8)*.

Lectin-like oxidized LDL receptor 1 (LOX-1) is the receptor for oxidized LDL identified in endothelial cells *(9, 10)*. Activation of LOX-1 in endothelial cells induces various changes relevant to endothelial dysfunction, e.g., superoxide generation, reduction in the release of nitric oxide, and induction of the expression

[1] Department of Vascular Physiology and [2] Department of Preventive Cardiology, National Cardiovascular Center, Osaka, Japan; [3] Biomarker Science Co. Ltd., Osaka, Japan; [4] Laboratory of Immunobiology, Department of Molecular and Applied Biosciences, Graduate School of Biosphere Science, Hiroshima University, Hiroshima, Japan.
* Address correspondence to this author at: Department of Vascular Physiology, National Cardiovascular Center, 5-7-1, Fujishirodai, Suita, Osaka, 565-8565 Japan. Fax +81-6-6872-7485; e-mail t-sawamura@umin.ac.jp.

Received November 15, 2009; accepted December 18, 2009.
Previously published online at DOI: 10.1373/clinchem.2009.140707

[5] Nonstandard abbreviations: CHD, coronary heart disease; LOX-1, lectin-like oxidized LDL receptor 1; MCP-1, monocyte chemoattractant protein 1; ApoB, apolipoprotein B; LAB, LOX-1 ligand containing ApoB; sLOX-1, soluble LOX-1; TC, total cholesterol; MI, myocardial infarction; MONICA, Monitoring Trends and Determinants of Cardiovascular Disease; CVD, cardiovascular disease; HR, hazard ratio; BMI, body mass index.

of monocyte chemoattractant protein 1 (MCP-1) and adhesion molecules *(11–13)*. In addition to oxidized LDL, LOX-1 binds various ligands, e.g., apoptotic cells, activated platelets, leukocytes, and C-reactive protein *(14–17)*. Accumulating evidence suggests that LOX-1 is involved in endothelial dysfunction, inflammation, atherogenesis, myocardial infarction, and intimal thickening after balloon catheter injury *(16, 18–23)*.

Recently, we developed a system to measure the biological activity of apolipoprotein B (ApoB)-containing lipoprotein based on binding to LOX-1 *(24)*. The activity of LOX-1 ligand containing ApoB (LAB) might reflect atherogenicity of LDL better than measurements of oxidized lipids, oxidized LDL, and LDL. In addition, recent reports have shown that the serum concentrations of soluble LOX-1 (sLOX-1), which is released from the cell surface by proteolysis of LOX-1, might be a useful biomarker for the diagnosis of acute coronary syndrome *(25, 26)*. Accordingly, we hypothesized that the product of LAB and sLOX-1, here designated "LOX index," might be an even better marker reflecting the interaction of atherogenic lipoproteins and their receptors.

Materials and Methods

STUDY POPULATION

The Suita Study is a population-based cohort study in an urban area performed by the National Cardiovascular Center, the details of which have been reported *(2, 27, 28)*. Briefly, in 1989, 6485 men and women, aged 30–79 years, were enrolled as study participants randomly selected from the community of Suita City. They underwent medical examinations every 2 years. In these participants, we set the baseline of the present study as the medical examination held between April 1994 and February 1995, since at that time serum samples were collected and stored at −80 °C. During this 10-month time period, 2437 participants were followed until December 31, 2007. Of these, 142 participants were excluded or the following reasons: history of CHD or stroke (n = 94), lost to follow-up (n = 17), and other reasons such as missing data (n = 31). Data from the remaining 2295 participants (1094 men and 1201 women) were included in the analysis. Informed consent was obtained from all participants. This study was approved by the institutional review board at the National Cardiovascular Center.

BASELINE MEDICAL EXAMINATION

A baseline survey included questionnaires, anthropometric measurements, and blood sample testing after overnight fasting (at least 10 h). Height and weight were measured in light clothing, and body mass index (BMI) was calculated as weight (kg) divided by height (m) squared. Blood pressure of participants in a sitting position after at least 5 min of rest was measured 3 times by well-trained physicians, using a standard mercury sphygmomanometer *(27)*. The average of the second and third measurement was used in the analysis. Hypertension was defined as systolic blood pressure ≥140 mmHg, diastolic blood pressure ≥90 mmHg, and/or the use of antihypertensive agents. Serum total cholesterol (TC), HDL cholesterol, and fasting serum glucose were analyzed with an automated analyzer at the laboratory of the National Cardiovascular Center. Non-HDL cholesterol was calculated by subtracting HDL cholesterol from TC. Diabetes was defined as serum glucose concentrations ≥7.0 mmol/L (126 mg/dL) in fasting or ≥11.1 mmol/L (200 mg/dL) in nonfasting samples and/or current use of medications for diabetes. Well-trained health nurses obtained information on the smoking, alcohol drinking, and medical histories of the participants.

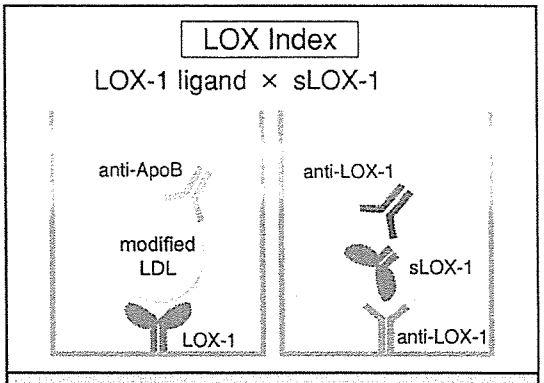

Fig. 1. Scheme of the detection systems for LAB and sLOX-1 to determine LOX index.

MEASUREMENT OF LAB

A schematic presentation of the detection system for sLOX-1 and LAB is shown in Fig. 1.

We immobilized recombinant human LOX-1(61–273) (0.25 μg/well) on 384-well plates (Greiner 384 Plate High Bind 781061) by incubating overnight at 4 °C in 50 μL PBS *(9, 24)*. After 3 washes with PBS, we blocked the plates with 80 μL of 3% BSA in HEPES buffer (10 mol/L HEPES, 150 mmol/L NaCl, pH 7.0). After 3 washes with PBS, the plates were incubated for 2 h at room temperature with 40 μL standard oxidized LDL or samples. We prepared samples by 20-fold dilution of serum with EDTA-BSA-HEPES buffer [2 mmol/L EDTA, 5% BSA/HEPES buffer (10 mmol/L HEPES, 150 mmol/L NaCl, pH 7.0)] and standards by dilution of oxidized LDL with EDTA-BSA-HEPES buffer. After 3 washes with PBS, the plates were incu-

bated for 1 h at room temperature with 83 μg/L chicken monoclonal anti-ApoB antibody (HUC20) in EDTA-BSA-HEPES buffer *(24)*. After 3 washes with PBS, the plates were incubated for 1 h at room temperature with peroxidase-conjugated donkey antichicken IgY (AP194P; Chemicon) diluted 6000 times with EDTA-BSA-HEPES buffer. After 5 washes with PBS, we added the substrate solution containing 3,3′,5,5′-tetramethylbenzidine (TMB solution; Bio-Rad) to the plates and incubated them for 30 min at room temperature. The reaction was terminated with 2 mol/L sulfuric acid. We determined peroxidase activity by measuring absorbance at 450 nm; the functional sensitivity of the measurement was 7.8 μg/L, and the range of the measurement was 7.8–500 μg/L oxidized LDL. Imprecision (CV) was 7.5% intraassay and 12.5% interassay at 50 μg/L (n = 10).

MEASUREMENT OF sLOX-1

We immobilized antihuman LOX-1 antibody (TS92, 0.25 μg/well) on 384-well plates (Corning 384 Plate High Bind 3700) by incubating overnight at 4 °C in 50 μL PBS *(9)*. After 3 washes with PBS, the plates were blocked with 20% ImmunoBlock (DS Pharma). After 3 washes with PBS, the plates were incubated with 40 μL standard oxidized LDL or samples for 2 h at room temperature. We prepared samples by 4-fold dilution of the serum with 1% BSA/PBS containing 0.04% Tween20 and 2 mmol/L EDTA and also by dilution of recombinant extracellular LOX-1(61–273) with the same buffer. After 3 washes with PBS, the plates were incubated with 0.16 μg/mL chicken monoclonal antihuman LOX-1 antibody (HUC5–40) in PBS containing 0.04% Tween20 and 2 mmol/L EDTA for 1 h at room temperature *(29)*. After 3 washes with PBS, the plates were incubated with the peroxidase-conjugated donkey antichicken IgY diluted 5000 times. After 5 washes with PBS, the substrate solution containing TMB solution was added to the plates and incubated for 30 min at room temperature. The reaction was terminated with 2 mol/L sulfuric acid. We determined peroxidase activity by measuring absorbance at 450 nm; the functional sensitivity of the measurement was 15.6 ng/L and the range of the measurement of sLOX-1 was 15.6–2500 ng/L. Imprecision (CV) was 8.5% intraassay and 14.7% interassay at 150 ng/L (n = 10).

ENDPOINT DETERMINATION

The method of endpoint determination for the Suita Study has been reported *(2, 27, 28)*. The endpoints of the current follow-up study were (1) date of first CHD or stroke event; (2) date of death; (3) date of leaving Suita city; and (4) December 31, 2007.

The first step in the survey for CHD and stroke involved checking the health status of all participants by repeated clinical visits every 2 years and yearly questionnaires sent by mail or conducted by telephone. In the second step, in-hospital medical records of participants who were suspected of having CHD or stroke were reviewed by registered hospital physicians or research physicians who were blinded to the baseline information. To complete the surveillance for fatal CHD and stroke, we conducted a systematic search for death certificates. The criteria for stroke were defined according to US National Survey of Stroke criteria *(30)*. Classification of patients into stroke subtypes (ischemic stroke, intracerebral hemorrhage, and subarachnoid hemorrhage) was based on examination of computed tomography, magnetic resonance imaging, or autopsy. Definite and probable myocardial infarction (MI) were defined according to the criteria of the MONICA (Monitoring Trends and Determinants of Cardiovascular Disease) project *(31)*. The criteria for a diagnosis of CHD included first-ever MI, coronary artery bypass surgery, or angioplasty. Sudden deaths of unknown origin that occurred within 24 h from onset were classified as CHD in the present study. We also defined cardiovascular disease (CVD) as a composite outcome of CHD or stroke.

STATISTICAL ANALYSIS

In addition to sLOX and LAB, we calculated the LOX index by multiplying serum concentrations of sLOX-1 by those of LAB. We set the cutoff points of sLOX, LAB, and LOX index according to the quartile ranges. Statistical methods of data analysis included ANOVA for assessing mean differences between groups and χ^2 tests for proportions. Multivariable analysis combining patients of both sexes was performed because there was no interaction between sex and LOX index (or LAB, sLOX) on the incidence of CHD or stroke. We calculated the multivariable-adjusted hazard ratios (HRs) of sLOX, LAB, and LOX index for CHD or stroke using a proportional hazards regression model after adjusting for sex, age, hypertension, diabetes, use of lipid-lowering agent, BMI, and current smoking and alcohol drinking (model 1). Further adjustment for non-HDL cholesterol was also performed (model 2). All CIs were estimated at the 95% level, and significance was set at $P < 0.05$. We used the SAS Statistical Package (release version 8.2, SAS Institute) for all the analyses.

Results

LAB and sLOX-1 concentrations at baseline [mean (SE)] were 516.1 (17.1) μg/L and 1060.1 (8.6) ng/L in men and 782.3 (23.7) μg/L and 797.8 (0.2) ng/L in women. The mean baseline serum TC was 181.5 (1.3) mg/dL [4.70 (0.034) mmol/L] in men and 224.5 (2.0) mg/dL [5.81 (0.052) mmol/L] in women in this population. Table 1

Table 1. Sex-specific means and prevalence of risk factors according to LAB or sLOX-1 quartiles at the baseline survey.[a]

	Mean LAB, μg/L (range)					Mean sLOX1, ng/L (range)				
	Q1, 217 (21–349)	Q2, 496 (350–644)	Q3, 870 (649–1128)	Q4, 1931 (1133–6379)	*P* (trend)	Q1, 558 (85–754)	Q2, 925 (755–1085)	Q3, 1289 (1084–1534)	Q4, 2367 (1540–9874)	*P* (trend)
Men										
n	261	257	288	288		229	251	284	330	
Age, years	61 (12)	60 (12)	60 (12)	59 (12)	0.41	62 (12)	61 (13)	60 (13)	59 (12)	0.01
TC										
mg/dL	186 (30)	195 (30)	192 (33)	203 (30)	<0.001	195 (33)	194 (29)	193 (34)	196 (32)	0.65
mmol/L	4.82 (0.78)	5.05 (0.78)	4.97 (0.85)	5.26 (0.78)		5.05 (0.85)	5.02 (0.75)	5.00 (0.88)	5.08 (0.83)	
HDL cholesterol										
mg/dL	54 (14)	56 (14)	54 (15)	53 (12)	0.06	54 (14)	55 (15)	55 (14)	53 (13)	0.33
mmol/L	1.40 (0.36)	1.45 (0.36)	1.40 (0.39)	1.37 (0.31)		1.40 (0.36)	1.42 (0.39)	1.42 (0.36)	1.37 (0.34)	
Non-HDL cholesterol										
mg/dL	132 (31)	139 (32)	139 (34)	151 (32)	<0.001	141 (33)	139 (30)	138 (34)	142 (34)	0.35
mmol/L	3.42 (0.80)	3.60 (0.83)	3.60 (0.88)	3.91 (0.83)		3.65 (0.85)	3.60 (0.78)	3.57 (0.88)	3.68 (0.88)	
Hypertension, %[b]	35	37	37	39	0.96	34	37	37	39	0.99
Lipid-lowering agent use, %	4	4	3	5	0.53	5	4	4	4	0.88
Diabetes, %[c]	7	6	5	6	0.79	6	6	7	5	0.62
Current smoking, %	41	44	43	39	0.71	32	37	45	48	<0.001
Current alcohol drinking, %[d]	69	68	71	67	0.75	70	73	65	67	0.21
Women										
n	312	317	286	286		344	323	290	244	
Age, years	57 (12)	59 (12)	57 (12)	57 (12)	0.05	58 (12)	57 (12)	57 (13)	58 (13)	0.71
TC										
mg/dL	200 (32)	204 (33)	207 (32)	216 (37)	<0.001	208 (33)	207 (35)	203 (34)	207 (35)	0.19
mmol/L	5.18 (0.83)	5.28 (0.85)	5.36 (0.83)	5.59 (0.96)		5.39 (0.85)	5.36 (0.91)	5.26 (0.88)	5.36 (0.91)	
HDL cholesterol										
mg/dL	62 (14)	62 (14)	61 (13)	59 (13)	0.06	62 (14)	62 (13)	60 (13)	60 (13)	0.04
mmol/L	1.61 (0.36)	1.61 (0.36)	1.58 (0.34)	1.53 (0.34)		1.61 (0.36)	1.61 (0.34)	1.55 (0.34)	1.55 (0.34)	
Non-HDL cholesterol										
mg/dL	138 (32)	142 (33)	146 (34)	156 (39)	<0.001	146 (34)	145 (36)	143 (35)	148 (36)	0.48
mmol/L	3.57 (0.83)	3.68 (0.85)	3.78 (0.88)	4.04 (1.01)		3.78 (0.88)	3.76 (0.93)	3.70 (0.91)	3.83 (0.93)	
Hypertension, %	33	27	30	32	0.84	29	30	30	34	0.42
Lipid-lowering agent use, %	8	5	7	6	0.27	8	5	7	7	0.62
Diabetes, %	3	3	3	5	0.26	3	3	4	4	0.72
Current smoking, %	7	12	10	10	0.31	6	8	11	16	<0.001
Current alcohol drinking, %	25	28	26	24	0.84	25	27	23	28	0.52

[a] Data are mean (SE) unless noted otherwise.
[b] Hypertension was defined as systolic blood pressure ≥140 mmHg, diastolic blood pressure ≥90 mmHg, or use of antihypertensive agents.
[c] Diabetes was defined as fasting serum glucose ≥7.0 mmol/L (126 mg/dL), use of antidiabetic agents, or both.
[d] Alcohol drinking was defined as consuming at least 1 drink per week.

shows the baseline characteristics of the participants in each LAB or sLOX-1 quartile. In both sexes, there were significant differences in the mean concentrations for TC and non-HDL cholesterol according to LAB quartile, with higher concentrations in the higher LAB quartiles. Conversely, serum TC and non-HDL cholesterol were not found to be associated with sLOX-1 quartiles. In women, HDL cholesterol was lower in the higher LOX-1 quartiles. The prevalence of smoking was higher in the upper sLOX-1 quartiles but was not associated with LAB. There were no significant differences across quartiles in the prevalence of hypertension and diabetes.

During the mean follow-up period of 11 years, there were 68 incident cases of CHD and 91 cases of stroke, including 60 cases of ischemic stroke. The number of incident cases and multivariable-adjusted HRs for CVD, stroke, ischemic stroke, and CHD stratified by LAB and sLOX-1 are shown in Table 2. The HRs for stroke, ischemic stroke, and CHD were highest in the highest LAB quartile, and except for CHD, the trends in HRs across quartiles were statistically significant. The HR for CVD was highest in the top quartile of LAB, and the trend across quartiles was statistically significant. For sLOX-1, however, the across-quartile trends in HRs did not reach statistical significance.

The number of incident cases and multivariable-adjusted HRs for CVD, stroke, ischemic stroke, and CHD stratified by LOX index (LAB × sLOX-1) are shown in Table 3. The HR for ischemic stroke was constantly high from the second to the highest quartile: 3.39 (95% CI 1.34–8.53), 3.15 (1.22–8.13), and 3.23 (1.24–8.37), respectively. Furthermore, the HR of the highest quartile of LOX index was 2.09 (1.00–4.35) for CHD. In the highest LOX index quartile, the incidence of CVD was approximately 2-fold that in the lowest LOX index quartile, and the associated HR was 1.83 (1.03–2.96).

After additional adjustment for HDL cholesterol or the exclusion of sudden cardiac death from CHD, the results of all the analyses listed above remained the same (data not shown).

Discussion

In the present study, we followed 1094 men and 1201 women for a mean period of 11 years to investigate the impact of LAB, sLOX-1, and LOX index (LAB × sLOX) on the incidence of CVD. We found LAB and LOX index to be significantly associated with the incidence of CVD and CHD, especially ischemic stroke. This investigation is the first cohort study on the relationship between CVD and LOX index–related or oxidized LDL–related parameters in a general population.

Instead of oxidized LDL, here we measured the serum concentrations of LAB. Researchers have applied several methods to measure circulating concentrations of oxidized LDL, including measurement of oxidation-dependent epitopes in the ApoB moiety of LDL. These methods, however, which evaluate the amount of oxidized moiety on LDL, do not necessarily reflect biological activity. In contrast, the present assay system using recombinant LOX-1 and anti-ApoB antibody has the ability to evaluate the biological activity of the atherogenic lipoproteins (Fig. 1). On the other hand, circulating sLOX-1 concentrations might reflect the expression levels of LOX-1, the target site of the atherogenic lipoproteins in vascular wall. Therefore, LOX index (LAB × sLOX-1) could represent ligand (LAB)–receptor (LOX-1) interaction leading to vascular dysfunction. The present results confirmed LOX index as a predictor of the incidence of CVD. This suggests that LOX-1 may be important in the pathogenesis of CVD, and indicates that the evaluation of LOX-1–mediated signaling may serve as a potential tool for risk stratification.

It is well known that increased blood pressure, smoking, diabetes, and atrial fibrillation are major risk factors for stroke, especially for ischemic stroke *(32)*. In contrast with these risk factors, we found either no relationship or a weakly positive one between TC or LDL cholesterol and ischemic stroke in several cohort studies performed in the Japanese population *(32–34)*. A large metaanalysis of individual data from 61 prospective studies performed mainly in Western populations also showed no association between TC or non-HDL cholesterol and stroke mortality *(4)*. We recently reported that we found no association between LDL cholesterol or non-HDL cholesterol concentrations and the incidence of ischemic stroke in this cohort using another baseline survey, shortly before that of the present study *(2)*. In contrast, the present investigation demonstrated that the LOX index is a predictor of not only CHD but also ischemic stroke. A strong association of LOX-1 with ischemic stroke in experimental models has been reported. For example, expression of LOX-1 and MCP-1 is increased in the early stage of atherosclerotic changes of common carotid arteries in spontaneously hypertensive rats *(35)*. Schwarz et al. *(36)* reported that LOX-1 expression was induced >10-fold at ischemic core sites during experimental stroke. Furthermore, we found that LOX-1 contributed to the formation of arterial thrombus (unpublished data). Thus, activation of LOX-1 might facilitate the pathophysiological conditions leading to stroke. In the present study, the risk for ischemic stroke was significantly increased from the second to the fourth quartile of LOX index, which suggests a protective role

Table 2. Age- and multivariable-adjusted odds ratios (95% CIs) for the incidence of cardiovascular disease and its subtypes according to LAB and sLOX-1 quartiles.

	Mean LAB, μg/L (range)					Mean sLOX1, ng/L (range)				
	Q1, 217 (21–349)	Q2, 496 (350–644)	Q3, 870 (649–1128)	Q4, 1931 (1133–6379)	*P* (trend)	Q1, 558 (85–754)	Q2, 925 (755–1085)	Q3, 1289 (1084–1534)	Q4, 2367 (1540–9874)	*P* (trend)
Person-years	6447	6343	6323	6156		6376	6446	6173	6276	
Stroke										
Cases, n	16	27	22	26		21	20	25	25	
Age-adjusted	1	1.60 (0.86–2.99)	1.44 (0.75–2.75)	1.86 (0.99–3.50)	0.09	1	0.93 (0.50–1.72)	1.18 (0.66–2.12)	1.17 (0.65–2.11)	0.45
Multivariable-adjusted, model 1[a]	1	1.68 (0.90–3.15)	1.49 (0.77–2.89)	2.07 (1.09–3.91)	0.05	1	0.89 (0.48–1.65)	1.16 (0.64–2.09	1.12 (0.61–2.03)	0.52
Multivariable-adjusted, model 2	1	1.69 (0.90–3.17)	1.50 (0.77–2.90)	2.09 (1.10–3.98)	0.05	1	0.89 (0.48–1.66)	1.17 (0.64–2.10)	1.12 (0.61–2.04)	0.52
Ischemic stroke										
Cases, n	9	18	13	20		12	17	13	18	
Age-adjusted	1	1.99 (0.89–4.44)	1.51 (0.64–3.56)	2.62 (1.18–5.79)	0.04	1	1.37 (0.65–2.87)	1.02 (0.46–2.25)	1.34 (0.64–2.81)	0.63
Multivariable-adjusted, model 1	1	2.12 (0.94–4.77)	1.63 (0.68–3.90)	3.18 (1.41–7.12)	0.01	1	1.38 (0.65–2.94)	1.02 (0.46–2.25)	1.29 (0.60–2.74)	0.72
Multivariable-adjusted, model 2	1	2.10 (0.93–4.74)	1.62 (0.67–3.88)	3.11 (1.37–7.04)	0.15	1	1.38 (0.65–2.94)	1.03 (0.46–2.29)	1.29 (0.60–2.74)	0.71
CHD										
Cases, n	12	18	15	23		12	17	23	16	
Age-adjusted	1	1.46 (0.69–3.07)	1.35 (0.63–2.90)	2.02 (1.00–4.08)	0.06	1	1.47 (0.69–3.16)	2.12 (1.03–4.37)	1.44 (0.66–3.12)	0.24
Multivariable-adjusted, model 1	1	1.54 (0.73–3.26)	1.44 (0.66–3.16)	2.18 (1.06–4.44)	0.04	1	1.53 (0.71–3.30)	1.97 (0.95–4.08)	1.42 (0.64–3.07)	0.31
Multivariable-adjusted, model 2	1	1.42 (0.67–3.02)	1.35 (0.62–2.96)	1.82 (0.88–3.76)	0.13	1	1.66 (0.77–3.58)	2.13 (1.02–4.42)	1.47 (0.67–3.21)	0.27
Cardiovascular disease										
Cases, n	28	45	37	49		33	37	48	41	
Age-adjusted	1	1.52 (0.94–2.45)	1.38 (0.84–2.26)	1.89 (1.18–3.02)	0.02	1	1.13 (0.70–1.81)	1.50 (0.96–2.35)	1.26 (0.79–2.02)	0.18
Multivariable-adjusted, model 1	1	1.60 (0.99–2.59)	1.44 (0.87–2.38)	2.05 (1.28–3.29)	0.01	1	1.11 (0.69–1.80)	1.43 (0.91–2.24)	1.21 (0.75–1.94)	0.27
Multivariable-adjusted, model 2	1	1.56 (0.96–2.52)	1.41 (0.85–2.32)	1.91 (1.18–3.08)	0.02	1	1.13 (0.70–1.83)	1.48 (0.94–2.33)	1.21 (0.76–1.95)	0.26

[a] Model 1 adjusted for age, sex, BMI, smoking, drinking, hypertension, diabetes, and use of lipid-lowering agents; model 2 as model 1 with the addition of non-HDL cholesterol.

Table 3. Age- and multivariable-adjusted odds ratios (95% CIs) for the incidence of cardiovascular disease and its subtypes according to LOX index ($\times 10^6$) quartiles.

	Mean LOX index (range)				
	Q1, 0.21 (0.017–0.363)	Q2, 0.52 (0.364–0.7040)	Q3, 0.97 (0.7043–1.314)	Q4, 2.64 (1.315–44.22)	*P* (trend)
Person-years	6416	6396	6314	6144	
Stroke					
Cases, n	17	24	25	25	
Age-adjusted	1	1.49 (0.80–2.80)	1.50 (0.80–2.79)	1.68 (0.90–3.14)	0.12
Multivariable-adjusted, model 1[a]	1	1.44 (0.76–2.71)	1.59 (0.85–2.99)	1.74 (0.92–3.28)	0.08
Multivariable-adjusted, model 2	1	1.44 (0.76–2.71)	1.60 (0.85–3.00)	1.74 (0.92–3.30)	0.09
Ischemic stroke					
Cases, n	6	20	17	17	
Age-adjusted	1	3.54 (1.41–8.87)	2.80 (1.10–7.14)	3.03 (1.18–7.74)	0.07
Multivariable-adjusted, model 1	1	3.40 (1.35–8.56)	3.22 (1.25–8.29)	3.31 (1.28–8.56)	0.03
Multivariable-adjusted, model 2	1	3.39 (1.34–8.53)	3.15 (1.22–8.13)	3.23 (1.24–8.37)	0.04
CHD					
Cases, n	12	19	12	25	
Age-adjusted	1	1.81 (0.85–3.81)	1.07 (0.47–2.44)	2.40 (1.17–4.93)	0.05
Multivariable-adjusted, model 1	1	1.70 (0.80–3.64)	1.04 (0.45–2.40)	2.37 (1.15–4.90)	0.05
Multivariable-adjusted, model 2	1	1.67 (0.78–3.59)	1.02 (0.44–2.35)	2.09 (1.00–4.35)	0.11
Cardiovascular disease					
Cases, n	29	43	37	50	
Age-adjusted	1	1.58 (0.98–2.55)	1.31 (0.80–2.15)	1.92 (1.20–3.07)	0.02
Multivariable-adjusted, model 1	1	1.49 (0.92–2.42)	1.35 (0.82–2.23)	1.95 (1.21–3.13)	0.01
Multivariable-adjusted, model 2	1	1.48 (0.91–2.41)	1.31 (0.80–2.17)	1.83 (1.13–2.96)	0.03

[a] Model 1 adjusted for age, sex, BMI, smoking, drinking, hypertension, diabetes, and use of lipid-lowering agents; model 2 as model 1 with the addition of non-HDL cholesterol.

against ischemic stroke. Additional epidemiologic studies to establish clinical cut points of LOX index are warranted.

The positive relationship between LOX index and ischemic stroke bridged, for the first time, the missing link between stroke and cholesterol-related parameters. In those with high LOX index, breaking the interaction between LAB and LOX-1 might be effective in preventing stroke. The most straightforward approach would be to apply a LOX-1 antagonist, which is yet to be developed. Although most of the randomized controlled trials failed to find a beneficial effect of antioxidants for the prevention of CVD *(21)*, we may reduce LAB concentration per se by statin therapy, thereby increasing LDL receptor expression, leading to an increase in the turnover of LDL and a decrease in the chance of LDL modification *(37)*. Actually, in the present study, serum concentrations of LAB showed a significant association with TC and non-HDL cholesterol. In addition, a positive relationship between smoking and LOX-1 suggests the possibility of smoking cessation to reduce sLOX-1 concentration by decreasing the expression level of LOX-1.

The present study has some limitations. First, a recent report from the Hisayama study showed a positive relationship between LDL cholesterol and atherothrombotic infarction, which accounts for one fourth of all ischemic stroke *(38)*. Therefore, the relation between LOX index and each subtype of ischemic stroke would be worth analyzing; however, the relatively small sample size of the current study precludes such analysis. Second, the participants in the present investigation were all Japanese; therefore, the study should be repeated in other ethnic populations. Because the incidence of stroke in Japan is much greater than in other countries *(39)*, some Japanese-specific factors might be affecting the present findings. Finally, since the number of cardiovascular events was not sufficiently large to enable a sex-specific analysis, especially in women, we did not perform such analysis.

In conclusion, LOX index is associated with an increased risk of CVD, especially ischemic stroke, in a Japanese urban population. From a public health viewpoint, the novel biochemical marker may provide new insights into not only risk stratification but also therapeutic strategy for CVD.

Author Contributions: *All authors confirmed they have contributed to the intellectual content of this paper and have met the following 3 requirements: (a) significant contributions to the conception and design, acquisition of data, or analysis and interpretation of data; (b) drafting or revising the article for intellectual content; and (c) final approval of the published article.*

Authors' Disclosures of Potential Conflicts of Interest: *Upon manuscript submission, all authors completed the Disclosures of Potential Conflict of Interest form. Potential conflicts of interest:*

Employment or Leadership: None declared.

Consultant or Advisory Role: None declared.

Stock Ownership: None declared.

Honoraria: None declared.

Research Funding: This study was supported in part by grants from the Ministry of Education, Culture, Sports, Science and Technology of Japan; the Ministry of Health, Labour and Welfare of Japan; the National Institute of Biomedical Innovation; Japan Science and Technology Agency; and the New Energy and Industrial Technology Development Organization. The authors have declared that no conflict of interests exist.

Expert Testimony: None declared.

Role of Sponsor: The funding organizations played no role in the design of study, choice of enrolled patients, review and interpretation of data, or preparation or approval of manuscript.

Acknowledgments: T. Sawamura had full access to all of the data in the study and takes responsibility for the integrity of the data and the accuracy of the data analysis.

We acknowledge the members of Suita City Health Center, the Suita Medical Association, and Satsuki-Junyukai, the volunteers involved in the administration of the Suita Study.

References

1. Kitamura A, Iso H, Naito Y, Iida M, Konishi M, Folsom AR, et al. High-density lipoprotein cholesterol and premature coronary heart disease in urban Japanese men. Circulation 1994;89:2533–9.
2. Okamura T, Kokubo Y, Watanabe M, Higashiyama A, Miyamoto Y, Yoshimasa Y, Okayama A. Low-density lipoprotein cholesterol and non-high-density lipoprotein cholesterol and the incidence of cardiovascular disease in an urban Japanese cohort study: the Suita study. Atherosclerosis 2009;203:587–92.
3. Expert Panel on Detection, Evaluation and Treatment of High Blood Cholesterol in Adults. Executive summary of the Third Report of the National Cholesterol Education Program (NCEP) Expert Panel on Detection, Evaluation, and Treatment of High Blood Cholesterol in Adults (Adult Treatment Panel III). JAMA 2001;285:2486–97.
4. Prospective Studies Collaboration. Blood cholesterol and vascular mortality by age, sex, and blood pressure: a meta-analysis of individual data from 61 prospective studies with 55,000 vascular deaths. Lancet 2007;370:1829–39.
5. Holvoet P, Collen D, Van de Werf F. Malondialdehyde-modified LDL as a marker of acute coronary syndromes. JAMA 1999;281: 1718–21.
6. Tsimikas S, Brilakis ES, Miller ER, McConnell JP, Lennon RJ, Kornman KS, et al. Oxidized phospholipids, Lp(a) lipoprotein, and coronary artery disease. N Engl J Med 2005;353:46–57.
7. Holvoet P, Lee D-H, Steffes M, Gross M, Jacobs DR Jr. Association between circulating oxidized low-density lipoprotein and incidence of the metabolic syndrome. JAMA 2008;299:2287–93.
8. Toshima S, Hasegawa A, Kurabayashi M, Itabe H, Takano T, Sugano J, et al. Circulating oxidized low density lipoprotein levels: a biochemical risk marker for coronary heart disease. Arterioscler Thromb Vasc Biol 2000;20:2243–7.
9. Sawamura T, Kume N, Aoyama T, Moriwaki H, Hoshikawa H, Aiba Y, et al. An endothelial receptor for oxidized low-density lipoprotein. Nature 1997;386:73–7.
10. Ogura S, Kakino A, Sato Y, Fujita Y, Iwamoto S, Otsui K, et al. LOX-1: the multifunctional receptor underlying cardiovascular dysfunction. Circ J 2009;73:1993–9.
11. Cominacini L, Rigoni A, Pasini AF, Garbin U, Davoli A, Campagnola M, et al. The binding of oxidized low density lipoprotein (ox-LDL) to ox-LDL receptor-1 reduces the intracellular concentration of nitric oxide in endothelial cells through an increased production of superoxide. J Biol Chem 2001;276:13750–5.
12. Sakurai K, Cominacini L, Garbin U, Fratta Pasini A, Sasaki N, Takuwa Y, et al. Induction of endothelin-1 production in endothelial cells via co-operative action between CD40 and lectin-like oxidized LDL receptor (LOX-1). J Cardiovasc Pharmacol 2004;44:S173–80.
13. Szmitko PE, Wang CH, Weisel RD, Jeffries GA, Anderson TJ, Verma S. Biomarkers of vascular disease linking inflammation to endothelial activation: part II. Circulation 2003;108:2041–8.
14. Oka K, Sawamura T, Kikuta K, Itokawa S, Kume N, Kita T, Masaki T. Lectin-like oxidized low-density lipoprotein receptor 1 mediates phagocytosis of aged/apoptotic cells in endothelial cells. Proc Natl Acad Sci U S A 1998;95:9535–40.
15. Kakutani M, Masaki T, Sawamura T. A platelet-endothelium interaction mediated by lectin-like oxidized low-density lipoprotein receptor-1. Proc Natl Acad Sci U S A 2000;97:360–4.
16. Honjo M, Nakamura K, Yamashiro K, Kiryu J, Tanihara H, McEvoy LM, et al. Lectin-like oxidized LDL receptor-1 is a cell-adhesion molecule involved in endotoxin-induced inflammation. Proc Natl Acad Sci U S A 2003;100:1274–9.
17. Fujita Y, Kakino A, Nishimichi N, Yamaguchi S, Sato Y, Machida S, et al. Oxidized LDL receptor LOX-1 binds to C-reactive protein and mediates its vascular effects. Clin Chem 2009;55:285–94.
18. Mehta JL, Sanada N, Hu CP, Chen J, Dandapat A, Sugawara F, et al. Deletion of LOX-1 reduces atherogenesis in LDLR knockout mice fed high cholesterol diet. Circ Res 2007;100:1634–42.
19. Inoue K, Arai Y, Kurihara H, Kita T, Sawamura T. Overexpression of lectin-like oxidized low-density lipoprotein receptor-1 induces intramyocardial vasculopathy in apolipoprotein E-null mice. Circ Res 2005;97:176–84.
20. Nakagawa T, Akagi M, Hoshikawa H, Chen M, Yasuda T, Mukai S, et al. Lectin-like oxidized low-density lipoprotein receptor 1 mediates leukocyte infiltration and articular cartilage destruction in rat zymosan-induced arthritis. Arthritis Rheum 2002;46:2486–94.
21. Asplund K. Antioxidant vitamins in the prevention of cardiovascular disease: a systematic review. J Intern Med 2002;251:372–92.
22. Kataoka K, Hasegawa K, Sawamura T, Fujita M, Yanazume T, Iwai-Kanai E, et al. LOX-1 pathway affects the extent of myocardial ischemia-reperfusion injury. Biochem Biophys Res Commun 2003;300:656–60.
23. Hinagata J, Kakutani M, Fujii T, Naruko T, Inoue N, Fujita Y, et al. Oxidized LDL receptor LOX-1 is involved in neointimal hyperplasia after balloon arterial injury in a rat model. Cardiovasc Res 2006;69:263–71.
24. Sato Y, Nishimichi N, Nakano A, Takikawa K, Inoue N, Matsuda H, Sawamura T. Determination of LOX-1-ligand activity in mouse plasma with a chicken monoclonal antibody for ApoB. Atherosclerosis 2008;200:303–9.
25. Murase T, Kume N, Kataoka H, Minami M, Sawamura T, Masaki T, Kita T. Identification of soluble forms of lectin-like oxidized LDL receptor-1. Arterioscler Thromb Vasc Biol 2000; 20:715–20.
26. Hayashida K, Kume N, Murase T, Minami M, Nakagawa D, Inada T, et al. Serum soluble lectin-like oxidized low-density lipoprotein receptor-1 levels are elevated in acute coronary syndrome: a novel marker for early diagnosis. Circulation 2005;112:812–8.
27. Kokubo Y, Kamide K, Okamura T, Watanabe M, Higashiyama A, Kawanishi K, et al. Impact of high-normal blood pressure on the risk of cardiovascular disease in a Japanese urban cohort: the Suita study. Hypertension 2008;52:652–9.

28. Kokubo Y, Okamura T, Yoshimasa Y, Miyamoto Y, Kawanishi K, Kotani Y, et al. Impact of metabolic syndrome components on the incidence of cardiovascular disease in a general urban Japanese population: the Suita study. Hypertens Res 2008;31:2027–35.
29. Iwamoto S, Nishimichi N, Tateishi Y, Sato Y, Horiuchi H, Furusawa S, et al. Generation and characterization of chicken monoclonal antibodies against human LOX-1. MAbs 2009;1:357–63.
30. Walker AE, Robins M, Weinfeld FD. The national survey of stroke: clinical findings. Stroke 1981; 12:I13–44.
31. WHO. MONICA manual. CVD/MNC/version 1.1, 1986 Dec. Geneva: WHO; 1987 Jan. Section 4, Event registration data component; p 1–104 (S-4). http://www.ktl.fi/publications/monica/monograph_cd/manual86.htm (Accessed March 2010).
32. Tanizaki Y, Kiyohara Y, Kato I, Iwamoto H, Nakayama K, Shinohara N, et al. Incidence and risk factors for subtypes of cerebral infarction in a general population: the Hisayama study. Stroke 2000;31:2616–22.
33. Okamura T, Tanaka H, Miyamatsu N, Hayakawa T, Kadowaki T, Kita Y, et al. The relationship between serum total cholesterol and all-cause or cause-specific mortality in a 17.3-year study of a Japanese cohort. Atherosclerosis 2007;190:216–23.
34. Cui R, Iso H, Toyoshima H, Date C, Yamamoto A, Kikuchi S, et al. Serum total cholesterol levels and risk of mortality from stroke and coronary heart disease in Japanese: the JACC study. Atherosclerosis 2007;194:415–20.
35. Hamakawa Y, Omori N, Ouchida M, Nagase M, Sato K, Nagano I, et al. Severity dependent upregulations of LOX-1 and MCP-1 in early sclerotic changes of common carotid arteries in spontaneously hypertensive rats. Neurol Res 2004;26:767–73.
36. Schwarz DA, Barry G, Mackay KB, Manu F, Naeve GS, Vana AM, et al. Identification of differentially expressed genes induced by transient ischemic stroke. Mol Brain Res 2002;101:12–22.
37. Sawamura T. New idol for cholesterol reduction? Clin Chem 2009;55:2082–4.
38. Imamura T, Doi Y, Arima H, Yonemoto K, Hata J, Kubo M, et al. LDL cholesterol and the development of stroke subtypes and coronary heart disease in a general Japanese population: the Hisayama study. Stroke 2009;40:382–8.
39. Ueshima H, Sekikawa A, Miura K, Turin TC, Takashima N, Kita Y, et al. Cardiovascular disease and risk factors in Asia: a selected review. Circulation 2008;118:2702–9.

Clinical Chemistry 56:3
478–481 (2010)

Brief Communications

C-Reactive Protein Uptake by Macrophage Cell Line via Class-A Scavenger Receptor

Yoshiko Fujita, Akemi Kakino, Mariko Harada-Shiba, Yuko Sato, Kazunori Otsui, Ryo Yoshimoto, and Tatsuya Sawamura*

Department of Vascular Physiology, National Cardiovascular Center Research Institute, Suita, Osaka, Japan; *address correspondence to this author at: Department of Vascular Physiology, National Cardiovascular Center Research Institute, 5-7-1 Fujishirodai, Suita, Osaka 565-8565, Japan. Fax +81-6-6835-5329; e-mail t-sawamura@umin.ac.jp.

BACKGROUND: C-reactive protein (CRP) increases in response to inflammation and is purported to be a risk factor for atherogenesis. We recently demonstrated that a scavenger receptor, lectin-like oxidized LDL receptor (LOX-1), is a receptor for CRP. In light of the overlapping ligand spectrum of scavenger receptors such as modified LDL, bacteria, and advanced glycation end products, we examined whether other scavenger receptors recognize CRP.

METHODS: We analyzed the uptake of fluorescently labeled CRP in COS-7 cells expressing a series of scavenger receptors and in a monocytic cell line, THP-1, differentiated into macrophage with phorbol 12-myristate 13-acetate (PMA). We applied small interfering RNA (siRNA) against class-A scavenger receptor (SR-A) to THP-1 cells to suppress the expression of SR-A. We also analyzed the binding of nonlabeled CRP to immobilized recombinant LOX-1 and SR-A in vitro using anti-CRP antibody.

RESULTS: COS-7 cells expressing LOX-1 and SR-A internalized fluorescently labeled CRP in a dose-dependent manner, but cells expressing CD36, SR-BI, or CD68 did not. The recombinant LOX-1 and SR-A proteins recognized nonlabeled purified CRP and native CRP in serum in vitro. THP-1 cells differentiated into macrophage-like cells by treatment with PMA internalized fluorescently labeled CRP. siRNA against SR-A significantly and concomitantly inhibited the expression of SR-A ($P < 0.01$) and CRP uptake ($P < 0.01$), whereas control siRNA did not.

CONCLUSIONS: CRP is recognized by SR-A as well as LOX-1 and taken up via SR-A in a macrophage-like cell line. This process might be of significance in the pathogenesis of atherosclerotic disease.

C-reactive protein (CRP),[1] which is synthesized by hepatocytes in response to inflammation and tissue damage *(1)*, binds to various ligands exposed on damaged tissues or bacteria promoting phagocytosis and complement activation with C1q *(1, 2)*. Plasma CRP concentrations may rise as much as 1000-fold during infection or inflammation *(3)*. In addition, CRP concentrations, within the reference range, can predict cardiovascular diseases *(4, 5)*, and there is a good correlation between plasma CRP concentrations and the degree of atherosclerosis in hypercholesterolemic rabbits *(6)*.

Fcγ receptors CD16, CD32, and CD64 have been reported as the receptors for CRP *(7–9)*. In addition, we recently demonstrated that CRP increases vascular permeability through a direct binding to lectin-like oxidized LDL receptor (LOX-1), which is expressed in endothelial cells *(10)*. Members of the scavenger receptor family, such as class A scavenger receptor (SR-A), CD36, LOX-1, and scavenger receptor B-I (SR-BI), recognize common ligands such as modified LDL, bacteria, and advanced glycation end products, and they are thought to affect the progression of atherosclerosis *(11, 12)*. In this study, to further elucidate the atherogenic properties of CRP, we addressed whether other scavenger receptors are involved in the recognition of CRP.

Human sera with high and normal concentrations of CRP were obtained from Dako. Human CRP purified from pleural fluid was purchased from Chemicon (AG723). Sodium azide in the solution was extensively removed by dialyzing 3 times against a 3000-fold volume of Dulbecco's PBS (Wako). Gram-negative bacterial endotoxins were undetectable by limulus amebocyte lysate (Associates of Cape Cod), which can detect as little as 0.03 endotoxin units per mL endotoxins. CRP was fluorescently labeled with CypHer5E (GE Healthcare) and dialyzed 3 times against a 3000-fold volume of PBS.

COS-7 cells maintained with Dulbecco's modified Eagle's medium (DMEM; Invitrogen)/10% fetal bovine serum (FBS) were seeded 1 day before transfection. After reaching 80%–90% confluency, we transfected the cells with the plasmid using Lipofectamin 2000 transfection reagent (Invitrogen). We used the following cDNAs: human LOX-1 (GenBank NM002543), SR-A (GenBank NM002445), CD36 (GenBank NM000072), SR-BI (GenBank NM005505), CD68 (GenBank NM001251), and

[1] Nonstandard abbreviations: CRP, C-reactive protein; LOX-1, lectin-like oxidized LDL receptor; SR, scavenger receptor; DMEM, Dulbecco's modified Eagle's medium; FBS, fetal bovine serum; siRNA, small interfering RNA; PMA, phorbol 12-myristate 13-acetate; SRA-C6, anti–SR-A antibody; DAPI, 4′,6-diamidino-2-phenylindole.

dectin-1 (GenBank NM197947), which were subcloned into pcDNA6.2/V5/GW/D-TOPO expression vector (Invitrogen). We used pcDNA3.1/V5-His/lacZ (Invitrogen) as a control. After 48 h, we washed the cells with DMEM:1% antibiotics and antimycotic (AbAm; Invitrogen). We replaced the medium with CypHer5E-CRP-containing DMEM/1% AbAm and incubated the cells for 2 h at 37 °C. After washing with PBS, the cells were fixed with phosphate-buffered formalin (Wako) and permeabilized with 0.1% Triton X-100/PBS. We detected the expression of each receptor by immunostaining with anti-V5 antibody (Nacalai Tesque) combined with Alexa 488 antimouse IgG (Invitrogen). The nuclei of the cells were counterstained with 0.5 mg/L 4′,6-diamidino-2-phenylindole (DAPI) (Sigma). We divided the fluorescence intensities of CypHer5E and Alexa 488 by the cell number in a field, then divided the CypHer5E-CRP fluorescence intensity in the field by the Alexa 488 fluorescence value. These quantitative analyses were performed with an IN Cell Analyzer 1000 system (GE Healthcare).

We prepared recombinant human SR-A (amino acids 76–358) as described for LOX-1 *(10)*. Recombinant human SR-A (0.1 μg) or BSA (0.1 μg, Sigma) was immobilized to each well of 384-well plates (High Bind; Corning) by incubating at 4 °C in PBS overnight. After 2 washes with PBS, the plates were blocked with 80 μL of 20% ImmunoBlock (DS Pharma)/PBS at 4 °C for 8 h. After washing twice with PBS, we added CRP in the reaction buffer (10 mmol/L HEPES, 150 mmol/L NaCl, 2 mmol/L $CaCl_2$, 1% BSA, pH 7.0) to each well and incubated them at 4 °C overnight. We detected the binding of CRP with a TMB Peroxidase EIA Substrate kit (Bio-Rad) as described for LOX-1 *(10)*. We obtained small interfering RNA (siRNA) duplex oligoribonucleotides targeting the SR-A coding region (GenBank NM002445) from Invitrogen and used stealth RNAi duplex (Invitrogen) as a negative control. The siRNA sequences were as follows: 5′-GAUAUAACUCAAAGUCUCACGGGAA-3′, 5′-UUCCCGUGAGACUUUGAGUUAUAUC-3′ and 5′-CAGACCUUGAGAAAUAUCACUUUAA-3′, 5′-UUAAAGUGAUAUUUCUCAAGGUCUG-3′.

THP-1 cells were maintained with 10% FBS/1% AbAm/20 μmol/L mercaptoethanol:RPMI 1640 and differentiated with 100 nmol/L phorbol 12-myristate 13-acetate (PMA) (Sigma) for 48 h. We transfected the cells with siRNA oligos or control siRNA using Lipofectamin 2000 transfection reagent (Invitrogen) according to the manufacturer's instruction. After incubation at 37 °C for 24 h, we washed the cells with RPMI 1640/1% AbAm and replaced the medium with CypHer5E-CRP–containing RPMI 1640/1% AbAm, and the cells were incubated for 2 h. After washing with PBS, the cells were fixed with phosphate-buffered formalin (Wako) and permeabilized with 0.1% Triton X-100/PBS. We detected the effects of downregulation of SR-A gene expression by immunostaining with anti–SR-A antibody (SRA-C6; Trans Genic Inc) combined with Alexa 488 antimouse IgG. For detection of Fcγ receptors, we used anti-CD32 antibody (AT10; Santa Cruz) and anti-CD64 antibody (10.1; Santa Cruz). For CRP detection, we used anti-CRP antibody (Bethyl). The nuclei of the cells were counterstained with 0.5 mg/L DAPI. We divided the fluorescence intensities of CypHer5E and Alexa 488 by the cell number in a field. Quantitative analysis was performed with an IN Cell Analyzer 1000 system. All transfections were performed in triplicate.

All data are presented as mean (SE). Statistical analysis was performed with Student *t*-test. A *P* value <0.05 was considered statistically significant.

We examined whether CRP binds to scavenger receptors: LOX-1, SR-A, CD36, SR-BI, CD68, and dectin-1. Dectin-1 has the closest structural similarity to LOX-1 and belongs to C-type lectin-like molecule, although it is not a member of scavenger receptors.

Alexa546-labeled CRP at the concentration of 1 mg/L at 4 °C bound significantly to LOX-1–expressing cells ($P < 0.01$) but bound poorly to the cells expressing the other receptors (see Supplemental Fig. 1, which accompanies the online version of this article at http://www.clinchem.org/content/vol56/issue3). Cellular uptake of CypHer5E-labeled CRP, which shows fluorescence after endocytosis, was significantly higher in SR-A–expressing cells, in a dose-dependent manner (1–30 mg/L), as well as in LOX-1–expressing cells, compared with cells expressing the other receptors (Fig. 1). Immunostaining with anti-V5 antibody revealed that all the receptors were expressed at a similar level in the respective cells.

Using anti-CRP antibody, we confirmed that nonlabeled CRP was also taken up by SR-A–expressing COS-7 cells. We further observed a significant binding of nonlabeled CRP (0.1–1 mg/L) to immobilized recombinant SR-A ($P < 0.01$) (see online Supplemental Fig. 2). The binding was not affected by polymyxin B (5 mg/L), suggesting that it did not depend on the presence of endotoxin. Importantly, native CRP contained in human serum showed significant binding to SR-A, as well as to LOX-1 ($P < 0.01$) (see online Supplemental Fig. 3). The binding was dependent on the concentration of CRP in the serum, suggesting that SR-A and LOX-1 have a capacity to bind to a native form of CRP in serum in the presence of other plasma proteins. These results indicate that SR-A and LOX-1 are the receptors for CRP among the examined receptors.

Because SR-A works in the monocyte-macrophage system, we assessed whether CRP is taken up by macrophages via SR-A. We used a human monocytic cell line,

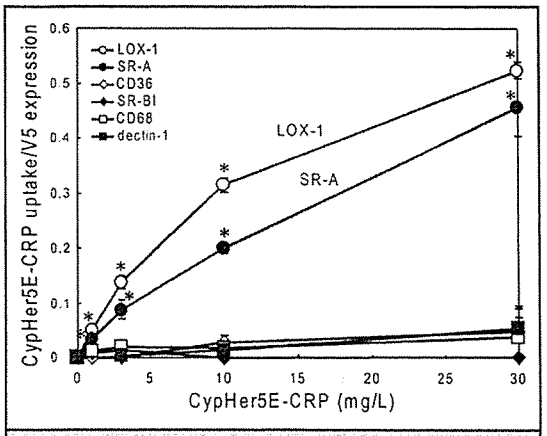

Fig. 1. Quantitative analyses of CypHer5E-CRP taken up by COS-7 cells expressing LOX-1, SR-A, CD36, SR-BI, and dectin-1.

Signals observed in the cells transfected with pcDNA3.1/V5-His/lacZ were considered as non-specific background. *Significant difference vs. negative control ($P < 0.01$).

THP-1, after inducing differentiation into macrophage by the treatment of PMA *(13)*. In PMA-treated THP-1 cells, CypHer5E-CRP was taken up in a dose-dependent manner (0.3–30 mg/L). SR-A expression and CRP uptake were concomitantly suppressed by 2 different siRNAs targeting SR-A, but not by control siRNA (Table 1). The siRNA targeting SR-A did not affect the expression of Fcγ receptors (data not shown), indicating that CRP is taken up mainly via SR-A in a macrophage cell line, at least under these conditions.

The ligand specificity of the scavenger receptor family overlaps considerably *(11, 12)*, and while all can bind to oxidized LDL, only SR-A or LOX-1 bound to CRP. Interestingly, dectin-1, the most structurally similar molecule to LOX-1, did not bind to CRP.

Using a monoclonal antibody, a previous report suggested the presence of an unknown receptor other than Fcγ receptors in macrophages *(14)*. It has been reported that fucoidin, a ligand for SR-A, inhibits the in vivo CRP-promoted uptake of oxidized LDL *(15)*. SR-A might be the unidentified CRP receptor. Fcγ receptors and SR-A are under different regulation of gene expression. In fact, in response to differentiation stimulus of PMA, the expression of SR-A is strongly induced, whereas the expression of Fcγ receptors is suppressed *(16, 17)*. Conversely, stimulation by interferon-γ enhances the expression of Fcγ receptors but suppresses the expression of SR-A *(18)*. These results suggest that Fcγ receptors and SR-A would work in the cells stimulated by different molecules.

Table 1. Suppression of the uptake of fluorescently labeled CRP by siRNA against SR-A in differentiated THP-1 cells.[a]

siRNA	SR-A expression, %	CypHer5E-CRP, %
None	103 (3.2)	108 (9.1)
Control siRNA	100 (2.7)	100 (9.8)
siRNA1 for SR-A	17 (1.6)[b]	31 (3.9)[b]
siRNA2 for SR-A	13 (0.0)[b]	32 (1.1)[b]

[a] Data are as mean (SE).
[b] Significant difference vs control siRNA groups ($P < 0.01$).

Interestingly, the activity of SR-A as CRP receptor was more pronounced in the uptake of CRP, whereas LOX-1 showed strong activity in both binding and uptake. Because SR-A works in phagocytes, the CRP uptake activity of SR-A is reasonable. CRP was originally identified as a binding protein for bacterial component C-polysaccharide *(3)*. SR-A may function to engulf bacteria, viruses, and harmful substances opsonized by CRP in a context of innate immunity.

Related to epidemiological risk factors for cardiovascular disease, the presence of CRP in atheroma has been reported in both rabbits and humans *(6)*. Furthermore, the colocalization of CRP and SR-A in macrophages in atheromas has been reported *(19)*. Taking these reports together with the present results, SR-A-mediated CRP uptake by macrophages in atheromas might affect the foam cell formation and progression of atherosclerotic disease.

Author Contributions: *All authors confirmed they have contributed to the intellectual content of this paper and have met the following 3 requirements: (a) significant contributions to the conception and design, acquisition of data, or analysis and interpretation of data; (b) drafting or revising the article for intellectual content; and (c) final approval of the published article.*

Authors' Disclosures of Potential Conflicts of Interest: *Upon manuscript submission, all authors completed the Disclosures of Potential Conflict of Interest form. Potential conflicts of interest:*

Employment or Leadership: None declared.
Consultant or Advisory Role: None declared.
Stock Ownership: None declared.
Honoraria: None declared.
Research Funding: Grants from the Ministry of Education, Culture, Sports, Science and Technology of Japan; the Ministry of Health, Labour and Welfare of Japan; the National Institute of Biomedical Innovation; and Japan Science and Technology Agency.
Expert Testimony: None declared.

Role of Sponsor: The funding organizations played no role in the design of study, choice of enrolled patients, review and interpretation of data, or preparation or approval of manuscript.

References

1. Black S, Kushner I, Samols D. C-reactive protein. J Biol Chem 2004;279:48487–90.
2. Volanakis JE, Kaplan MH. Interaction of C-reactive protein complexes with the complement system. II. Consumption of guinea pig complement by CRP complexes: requirement for human C1q. J Immunol 1974;113:9–17.
3. Gabay C, Kushner I. Acute-phase proteins and other systemic responses to inflammation. N Engl J Med 1999;340:448–54.
4. Ridker PM, Cushman M, Stampfer MJ, Tracy RP, Hennekens CH. Inflammation, aspirin, and the risk of cardiovascular disease in apparently healthy men. N Engl J Med 1997;336:973–9.
5. Ridker PM, Danielson E, Fonseca FA, Genest J, Gotto AM Jr, Kastelein JJ, et al. Rosuvastatin to prevent vascular events in men and women with elevated C-reactive protein. N Engl J Med 2008; 359:2195–207.
6. Sun H, Koike T, Ichikawa T, Hatakeyama K, Shiomi M, Zhang B, et al. C-reactive protein in atherosclerotic lesions: its origin and pathophysiological significance. Am J Pathol 2005;167: 1139–48.
7. Khreiss T, Jozsef L, Hossain S, Chan JS, Potempa LA, Filep JG. Loss of pentameric symmetry of C-reactive protein is associated with delayed apoptosis of human neutrophils. J Biol Chem 2002; 277:40775–81.
8. Bharadwaj D, Stein MP, Volzer M, Mold C, Du Clos TW. The major receptor for C-reactive protein on leukocytes is Fcgamma receptor II. J Exp Med 1999;190:585–90.
9. Stein MP, Mold C, Du Clos TW. C-reactive protein binding to murine leukocytes requires Fc gamma receptors. J Immunol 2000;164:1514–20.
10. Fujita Y, Kakino A, Nishimichi N, Yamaguchi S, Sato Y, Machida S, et al. Oxidized LDL receptor LOX-1 binds to C-reactive protein and mediates its vascular effects. Clin Chem 2009;55:285–94.
11. Moore KJ, Freeman MW. Scavenger receptors in atherosclerosis: beyond lipid uptake. Arterioscler Thromb Vasc Biol 2006;26:1702–11.
12. Greaves DR, Gordon S. The immune system and atherogenesis: recent insights into the biology of macrophage scavenger receptors. Thematic review series. J Lipid Res 2005;46:11–20.
13. Nishimura N, Harada-Shiba M, Tajima S, Sugano R, Yamamura T, Qiang QZ, Yamamoto A. Acquisition of secretion of transforming growth factor-beta 1 leads to autonomous suppression of scavenger receptor activity in a monocyte-macrophage cell line, THP-1. J Biol Chem 1998; 273:1562–7.
14. Tebo JM, Mortensen RF. Characterization and isolation of a C-reactive protein receptor from the human monocytic cell line U-937. J Immunol 1990;144:231–8.
15. Singh U, Dasu MR, Yancey PG, Afify A, Devaraj S, Jialal I. Human C-reactive protein promotes oxidized low density lipoprotein uptake and matrix metalloproteinase-9 release in Wistar rats. J Lipid Res 2008;49:1015–23.
16. Fleit HB, Kobasiuk CD. The human monocyte-like cell line THP-1 expresses Fc gamma RI and Fc gamma RII. J Leukoc Biol 1991;49:556–65.
17. Morganelli PM, Kennedy SM, Mitchell TI. Differential effects of interferon-gamma on metabolism of lipoprotein immune complexes mediated by specific human macrophage Fcgamma receptors. J Lipid Res 2000;41:405–15.
18. Geng YJ, Hansson GK. Interferon-gamma inhibits scavenger receptor expression and foam cell formation in human monocyte-derived macrophages. J Clin Invest 1992;89:1322–30.
19. Turk JR, Carroll JA, Laughlin MH, Thomas TR, Casati J, Bowles DK, Sturek M. C-reactive protein correlates with macrophage accumulation in coronary arteries of hypercholesterolemic pigs. J Appl Physiol 2003;95:1301–4.

Previously published online at
DOI: 10.1373/clinchem.2009.140202

Molecular Biology of the Cell
Vol. 21, 584–596, February 15, 2010

Vascular Endothelial-Cadherin Stabilizes at Cell–Cell Junctions by Anchoring to Circumferential Actin Bundles through α- and β-Catenins in Cyclic AMP-Epac-Rap1 Signal-activated Endothelial Cells

Kazuomi Noda,*†‡ Jianghui Zhang,*‡ Shigetomo Fukuhara,* Satoshi Kunimoto,*§ Michihiro Yoshimura,† and Naoki Mochizuki*

*Department of Structural Analysis, National Cardiovascular Center Research Institute, Suita, Osaka 565-8565, Japan; and †Division of Cardiology, Department of Internal Medicine, The Jikei University School of Medicine, Minato-ku, Tokyo 105-8461, Japan

Submitted July 17, 2009; Revised November 19, 2009; Accepted December 15, 2009
Monitoring Editor: Asma Nusrat

Vascular endothelial (VE)-cadherin is a cell–cell adhesion molecule involved in endothelial barrier functions. Previously, we reported that cAMP-Epac-Rap1 signal enhances VE-cadherin–dependent cell adhesion. Here, we further scrutinized how cAMP-Epac-Rap1 pathway promotes stabilization of VE-cadherin at the cell–cell contacts. Forskolin induced circumferential actin bundling and accumulation of VE-cadherin fused with green fluorescence protein (VEC-GFP) on the bundled actin filaments. Fluorescence recovery after photobleaching (FRAP) analyses using VEC-GFP revealed that forskolin stabilizes VE-cadherin at cell–cell contacts. These effects of forskolin were mimicked by an activator for Epac but not by that for protein kinase A. Forskolin-induced both accumulation and stabilization of junctional VEC-GFP was impeded by latrunculin A. VE-cadherin, α-catenin, and β-catenin were dispensable for forskolin-induced circumferential actin bundling, indicating that homophilic VE-cadherin association is not the trigger of actin bundling. Requirement of α- and β-catenins for forskolin-induced stabilization of VE-cadherin on the actin bundles was confirmed by FRAP analyses using VEC-GFP mutants, supporting the classical model that α-catenin could potentially link the bundled actin to cadherin. Collectively, circumferential actin bundle formation and subsequent linkage between actin bundles and VE-cadherin through α- and β-catenins are important for the stabilization of VE-cadherin at the cell–cell contacts in cAMP-Epac-Rap1 signal-activated cells.

INTRODUCTION

Endothelial cells lining blood vessels regulate endothelial barrier function, which restricts the passage of plasma proteins and circulating cells across the endothelium. Compromising vascular integrity leads to an increase in vascular permeability, which is associated with chronic inflammation, edema, and tumor angiogenesis (Dejana *et al.*, 2008; Wallez and Huber, 2008; Dejana *et al.*, 2009). Endothelial cells have two specialized junctional domains, adherens junctions (AJs) and tight junctions. AJs are constituted by vascular endothelial (VE)-cadherin (also known as cadherin-5 and CD144) and nectin, whereas tight junctions are composed of members of junctional adhesion molecule, claudins, and occludins (Dejana, 2004; Ebnet *et al.*, 2004; Wallez and Huber, 2008).

Interendothelial AJs are dynamic structures, and their adhesive property is finely controlled by various signaling molecules (Dejana *et al.*, 2008; Vestweber *et al.*, 2009). Inflammatory mediators such as thrombin and histamine induce intercellular gap formation leading to an increase in endothelial permeability (Andriopoulou *et al.*, 1999; Gavard, 2009). Vascular endothelial growth factor also weakens interendothelial cell junctions, which is thought to be a key initiation step of angiogenesis (Paul *et al.*, 2001; Weis *et al.*, 2004; Gavard and Gutkind, 2006; Dejana *et al.*, 2008). In contrast, angiopoietin-1 and sphingosine-1-phosphate stabilize endothelial barrier integrity (Thurston *et al.*, 1999; Gamble *et al.*, 2000; Garcia *et al.*, 2001; Fukuhara *et al.*, 2009; Augustin *et al.*, 2009). Furthermore, it is widely recognized that an increase in intracellular cAMP level in endothelial

This article was published online ahead of print in *MBC in Press* (http://www.molbiolcell.org/cgi/doi/10.1091/mbc.E09-07-0580) on December 23, 2009.

‡ These authors contributed equally to this work.

§ Present address: Division of Cardiology, Department of Medicine Nihon University School of Medicine, Itabashi-ku, Tokyo 173-8610, Japan.

Address correspondence to: Shigetomo Fukuhara (fuku@ri.ncvc.go.jp) or Naoki Mochizuki (nmochizu@ri.ncvc.go.jp).

Abbreviations used: 007, 8-pCPT-2′-*O*-methl-cAMP; 6-Bnz, N^6-benzoyl-cAMP; AJ, adherens junction; CREB, cAMP response element-binding protein; E-cadherin-GFP, green fluorescent protein-tagged E-cadherin; Epac, exchange protein directly activated by cAMP; EPLIN, epithelial protein lost in neoplasm; FRAP, fluorescence recovery after photobleaching; FSK, forskolin; GFP, green fluorescent protein; HUVEC, human umbilical vein endothelial cell; Lat.A, latrunculin A; PECAM, platelet/endothelial cell adhesion molecule; PECAM1-GFP, platelet/endothelial cell adhesion molecule 1 carboxy-terminally tagged with green fluorescent protein; PKA, protein kinase A; VE, vascular endothelial; VEC-GFP, vascular endothelial-cadherin carboxy-terminally fused with green fluorescent protein.

cells strengthens barrier function and attenuates endothelial permeability both in vitro and in vivo (Fukuhra *et al.*, 2006; Kooistra *et al.*, 2007; Adamson *et al.*, 2008; Pannekoek *et al.*, 2009). Consistently, cAMP-elevating G protein-coupled receptor agonists, such as adrenomedullin, prostacyclin, prostaglandin E2, and β-adrenergic agonists, reduce endothelial hyperpermeability induced by inflammatory stimuli (Langeler and van Hinsbergh, 1991; Farmer *et al.*, 2001; Hippenstiel *et al.*, 2002).

The mechanism by which cAMP enhances endothelial barrier function is thought to involve two cAMP effectors, protein kinase A (PKA) and exchange protein directly activated by cAMP (Epac) (Yuan, 2002; Fukuhara *et al.*, 2005; Cullere *et al.*, 2005; Kooistra *et al.*, 2005; Pannekoek *et al.*, 2009). Although we could not find a significant role for PKA in cAMP-induced barrier function previously (Fukuhara *et al.*, 2005), several reports have suggested that PKA stabilizes endothelial cell–cell junctions through reduction of myosin light chain phosphorylation, leading to relaxation of actomyosin complex, inhibition of Rho, and activation of Rac (Liu *et al.*, 2001; Qiao *et al.*, 2003; Birukova *et al.*, 2004, 2007). Lorenowicz *et al.* (2008) have also reported that PKA activation by N^6-benzoyl-cAMP (6-Bnz), a specific cAMP analogue for PKA, promotes endothelial barrier function in vitro. However, they also observed increased stress fiber formation in 6-Bnz–stimulated cells, which is a hallmark of Rho activation leading to disruption of endothelial cell–cell junctions. Thus, the role of PKA in cAMP-enhanced endothelial barrier function still remains elusive.

Epac is a guanine nucleotide exchange factor for Rap1 small GTPase (Kooistra *et al.*, 2007; Pannekoek *et al.*, 2009). 8-pCPT-2′-O-methl-cAMP (hereafter referred to as 007), a cAMP analogue specific for Epac, enhances endothelial barrier functions in vitro and in vivo (Fukuhara *et al.*, 2005; Cullere *et al.*, 2005; Kooistra *et al.*, 2005; Adamson *et al.*, 2008). Previously, we and others have shown that a cAMP–Epac–Rap1 pathway promotes endothelial barrier function by potentiating VE-cadherin–mediated cell–cell adhesions (Fukuhara *et al.*, 2005; Cullere *et al.*, 2005; Kooistra *et al.*, 2005). Consistently, Rap1 is involved in E-cadherin–based cell–cell adhesions in epithelial cells (Hogan *et al.*, 2004; Price *et al.*, 2004). In endothelial cells, 007 induces cortical actin bundle formation along the cell–cell junctions, which is thought to be required for Rap1-enhanced barrier function (Fukuhara *et al.*, 2005; Kooistra *et al.*, 2005; Lorenowicz *et al.*, 2008). Several signaling molecules, including Rac, K-Rev Interaction Trapped gene-1 (also known as CCM1), and AF-6, have been reported to act downstream of Rap1 to regulate actin cytoskeleton and barrier integrity (Boettner *et al.*, 2000; Boettner *et al.*, 2003; Arthur *et al.*, 2004; Birukova *et al.*, 2007; Glading *et al.*, 2007). However, it remains elusive how a cAMP–Epac–Rap1 pathway enhances VE-cadherin-dependent cell adhesions.

In the classical model, cadherin-β-catenin complexes are statically linked to bundled actin filaments via α-catenin to maintain AJs. Cytoplasmic region of cadherin binds to three armadillo-family proteins, β-, γ-, and p120-catenins (Ozawa and Kemler, 1992; Kemler, 1993; Reynolds *et al.*, 1994). α-Catenin associates with not only β- and γ-catenins but also the actin cytoskeleton (Nagafuchi *et al.*, 1994; Rimm *et al.*, 1995; Watabe-Uchida *et al.*, 1998; Sako *et al.*, 1998; Imamura *et al.*, 1999). However, the Weiss and Nelson groups have recently suggested a new dynamic model that α-catenin does not stably connect actin to cadherin by showing that α-catenin does not bind simultaneously to both the cadherin-β–catenin complex and actin filaments (Yamada *et al.*, 2005; Drees *et al.*, 2005; Gates and Peifer, 2005). However, Abe and Takeichi have recently shown that epithelial protein lost in neoplasm (EPLIN) is able to mediate a stable linkage between the cadherin–catenin complex and the actin cytoskeleton (Abe and Takeichi, 2007). Thus, it is still controversial how α-catenin functions in cadherin-based cell–cell adhesions.

In the present study, we demonstrate that initial circumferential actin bundling induced by the cAMP–Epac–Rap1 signal and its linkage to VE-cadherin-β-catenin by α-catenin is essential for the stabilization of VE-cadherin at the cell–cell contacts.

MATERIALS AND METHODS

Reagents and Antibodies

Materials were purchased as follows: forskolin (FSK) and latrunculin A (Lat.A) were from Calbiochem (San Diego, CA), Epac-specific activator 007 was from Tocris Bioscience (Bristol, United Kingdom), PKA-specific activator 6-Bnz was from Biolog Life Science Institute (Bremen, Germany), H89 was from Sigma-Aldrich (St. Louis, MO), and Cellmatrix type I-C was from Nitta Gelatin (Osaka, Japan). Antibodies used here were purchased as follows: anti-VE-cadherin was from Santa Cruz Biotechnology (Santa Cruz, CA), BD Biosciences (San Jose, CA), and Cell Signaling Technology (Danvers, MA); anti-α-catenin was from Zymed Laboratories (South San Francisco, CA), anti-β-catenin and anti-p120-catenin were from BD Bioscience, anti-cAMP response element-binding protein (CREB) and anti-phospho-CREB (Ser133) were from Cell Signaling Technology; anti-Rap1 was from Santa Cruz Biotechnology; anti-β-actin and anti-β-tubulin were from Sigma-Aldrich; rhodamine-phalloidin, Alexa 488-labeled goat anti-mouse immunoglobulin G (IgG), Alexa 633-labeled goat anti-mouse IgG, and Alexa 546-labeled goat anti-rabbit IgG were from Invitrogen (Carlsbad, CA); horseradish peroxidase-coupled goat anti-mouse and horseradish peroxidase-coupled goat anti-rabbit IgG were from GE Healthcare (Piscataway, NJ); and horseradish peroxidase-coupled donkey anti-goat IgG was from Santa Cruz Biotechnology.

Cell Culture, Transfection, Small Interfering RNA (siRNA)-mediated Protein Knockdown, and Adenovirus Infection

Human umbilical vein endothelial cells (HUVECs) were purchased from Kurabo (Kurashiki, Japan), maintained as described previously (Fukuhara *et al.*, 2008), and used for the experiments before passage 9. 293T cells were cultured in DMEM (Nissui, Tokyo, Japan) supplemented with 10% fetal bovine serum and antibiotics (100 μg streptomycin/ml and 100 U penicillin/ml). HUVECs and 293T cells were transfected using Lipofectamine 2000 and 293 fectin reagents (Invitrogen), respectively. Stealth siRNAs targeted to human VE-cadherin (HSS101682), human α-catenin (HSS102451 and 5′-UUAUUAGAGGGCCCUUUACUAUUGG-3′), human β-catenin (VHS50819 and VHS50822), and human p120-catenin (HSS102463 and HSS102465) were purchased from Invitrogen. As a control, siRNA duplexes with irrelevant sequences were used. HUVECs were transfected with 20 nM siRNA duplexes using Lipofectamine RNAi MAX reagent (Invitrogen). After incubation for 48 h, the cells were replated, cultured for additional 24 h, and were used for the experiments.

Recombinant adenoviruses encoding Rap1GAP and LacZ were obtained from S. Hattori (The Institute of Medical Science, University of Tokyo, Tokyo, Japan) and M. Matsuda (Research Institute for Microbial Disease, Osaka University, Osaka, Japan), respectively. HUVECs were infected with adenoviruses at the appropriated multiplicities of infection as described in the figure legends.

Plasmids

cDNAs for human VE-cadherin and human platelet/endothelial cell adhesion molecule (PECAM)1 were amplified from human heart cDNAs by reverse transcription-polymerase chain reaction (PCR) and cloned into pEGFP-N1 vector (Clontech, Mountain View, CA) to construct pEGFP-N1-VEC encoding VE-cadherin carboxy-terminally tagged with green fluorescence protein (VEC-GFP) and pEGFP-N1-PECAM1 encoding PECAM1 carboxy-terminally tagged with GFP (PECAM1-GFP), respectively. To generate the plasmid encoding VEC-GFP lacking β-catenin binding domain (VECΔβ-GFP) and that encoding VEC-GFP lacking cytoplasmic domain (VECΔC-GFP), amino acids 1-700 and 1-631 fragments of VE-cadherin were amplified by PCR and subcloned into pEGFP-N1 vector, namely, pEGFP-N1-VECΔβ and pEGFP-N1-VECΔC, respectively. To generate pEGFP-N1-VECΔC-α vector encoding VEC-GFP mutant in which cytoplasmic domain of VE-cadherin is replaced with α-catenin (VECΔC-α-GFP), a cDNA encoding full-length α-catenin was amplified by PCR using an expression vector for α-catenin (a gift from A. Nagafuchi, Kumamoto University, Kumamoto, Japan) as a template and inserted into the site immediately upstream of GFP in pEGFP-N1-VECΔC

vector. Similarly, a cDNA encoding amino acids 327–906 fragment of α-catenin was amplified by PCR and inserted into the same site of pEGFP-N1-VECΔC vector to construct the plasmid expressing VECΔC-αΔN-GFP. An siRNA-insensitive version of pEGFP-N1-VECΔC-α plasmid, namely, pEGFP-N1-VECΔC-α-in vector, was generated using QuickChange Site-directed mutagenesis kit (Stratagene, La Jolla, CA). A cDNA fragment encoding PECAM1 lacking cytoplasmic region was amplified by PCR and inserted into pEGFP-N1-vector to generate the pEGFP-N1-PECAM1ΔC plasmid encoding PECAM1-GFP mutant lacking the cytoplasmic region of PECAM1 (PECAM1ΔC-GFP). To construct the pEGFP-N1-PECAM1ΔC-α plasmid encoding PECAM1-GFP mutant in which cytoplasmic region is replaced with α-catenin (PECAM1ΔC-α-GFP), a cDNA encoding full-length α-catenin amplified by PCR was inserted into the site immediately upstream of GFP in pEGFP-N1-PECAM1ΔC vector. Similarly, a cDNA encoding cytoplasmic region of VE-cadherin was also inserted into the same site of pEGFP-N1-PECAM1ΔC vector to construct the pEGFP-N1-PECAM1ΔC-VEC/C plasmid encoding PECAM1-GFP mutant in which cytoplasmic region is replaced with that of VE-cadherin (PECAM1ΔC-VEC/C-GFP).

Fluorescence Recovery after Photobleaching Analysis

HUVECs plated on a 35-mm-diameter collagen-coated glass-base dish (Asahi Techno Glass, Chiba, Japan) were transfected with the expression plasmids encoding VEC-GFP, PECAM1-GFP, and their mutants and cultured for 24 h at confluent cell density. The cells were then starved in medium 199 containing either 1 or 0.1% bovine serum albumin (BSA) for 3 h, and stimulated with vehicle, 10 μM FSK, 0.2 mM 007, and 0.2 mM 6-Bnz for 30 min. Fluorescence recovery after photobleaching (FRAP) experiments were performed on a FV1000 laser-scanning confocal microscope (Olympus, Tokyo, Japan) with a 60× objective lens, and GFP fluorescence was imaged by the excitation with 473-nm diode laser. All experiments were performed at 37°C with 5% CO_2 using a heating chamber (Tokai Hit, Shizuoka, Japan). GFP-positive cells surrounded by GFP-negative cells were selected and subjected to FRAP analysis. GFP fluorescence at the cell–cell contacts was bleached for 5 s using 405-nm diode laser set at full power. To monitor fluorescence recovery, images were acquired every 90 s over a period of 50–60 min using the FluoView version 1.7c software (Olympus). Using Excel software (Microsoft, Redmond, WA), data were corrected for the overall loss in total fluorescence intensity as a result of the imaging scans. The fluorescence intensity of the bleached region over time was normalized with the prebleached fluorescence intensity. Recovery measurements were quantified by fitting normalized fluorescence intensities of bleached areas to a one-phase exponential association by using Prism 5 software (GraphPad Software, San Diego, CA). This program was also used for plotting of the data and statistical analysis.

Immunocytochemistry

Monolayer-cultured HUVECs grown on a collagen-coated glass-base dish were starved in medium 199 containing either 0.5 or 0.1% BSA for 3 h and subsequently stimulated with vehicle, 10 μM FSK, 0.2 mM 007, or 0.2 mM 6-Bnz for 30 min. After stimulation, the cells were fixed in phosphate-buffered saline (PBS) containing 2% formaldehyde for 30 min at 4°C, permeabilized with 0.05% Triton X-100 for 30 min at 4°C, and blocked with PBS containing 4% BSA for 1 h at room temperature. The cells were then stained with rhodamine-phalloidin for 20 min and with anti-VE-cadherin, anti-α-catenin, anti-β-catenin, and anti-p120-catenin antibodies for 60 min at room temperature. Protein reacting with antibody was visualized with species-matched Alexa 488-, Alexa 546- or Alexa 633-labeled secondary antibodies. Fluorescence images of GFP, rhodamine, Alexa 488, Alexa 546, and Alexa 633 were recorded with an Olympus IX-81 inverted fluorescence microscope (Olympus) equipped with pE-1 LED excitation system (CoolLED, Andover, United Kingdom) with a cooled charge-coupled device camera CoolSNAP-HQ (Roper Scientific, Trenton, NJ) and appropriate filter sets for GFP, Alexa 488, Alexa 546, and Alexa 633, and with a FluoView FV1000 confocal microscope with 60× and 100× oil immersion objective lens. To quantify the levels of F-actin at cell–cell contacts, fluorescence intensity of rhodamine along the 5-pixel-width lines randomly drawn on the rhodamine images was determined by line intensity scanning using MetaMorph software (Molecular Devices, Sunnyvale, CA). Peak fluorescence intensity at the points across the cell–cell contacts was taken as the value of F-actin at cell–cell contacts. A minimum of 80 contacts were analyzed per experiment, and experiments were repeated three times.

Detection of GTP-bound Form of Rap1 and Phosphorylated CREB

Rap1 activity and phosphorylation of CREB were assessed as described previously (Fukuhara *et al.*, 2005). In brief, HUVECs starved in medium 199 containing 1% BSA for 6 h were stimulated with vehicle, 10 μM FSK, 0.2 mM 007, or 0.2 mM 6-Bnz for 15 min and lysed at 4°C in a pull-down lysis buffer containing 20 mM Tris-HCl, pH 7.5, 100 mM NaCl, 10 mM $MgCl_2$, 1% Triton X-100, 1 mM EGTA, 1 mM dithiothreitol, 1 mM Na_3VO_4, and 1× protease inhibitor cocktail (Roche Applied Science, Indianapolis, IN). GTP-bound Rap1 was collected on the glutathione transferase-tagged Rap1 binding domain of RalGDS precoupled to glutathione-Sepharose beads and subjected to Western blot analysis with anti-Rap1 antibody. Aliquots of total cellular lysates were also subjected to Western blot analysis with anti-Rap1, anti-phospho-CREB, anti-CREB, and anti-β-actin antibodies.

Fluorescence-activated Cell Sorting (FACS) Analysis

Expression levels of VEC-GFP, PECAM1-GFP, and their mutants were analyzed by FACS analysis using FACSAria cell-sorting system (BD Biosciences).

Statistical Analysis

Data are expressed as either mean ± SD or mean ± SE as indicated in figure legends. Statistical significance was determined using Student's *t* test for paired samples or one-way analysis of variance and nonparametric tests for multiple groups. Data were considered statistically significant if p values <0.05.

RESULTS

cAMP Stabilizes VE-Cadherin at Cell–Cell Contacts through Epac–Rap1 Pathway, but Not PKA Pathway

To examine the dynamics of VE-cadherin in living cells, we constructed the plasmid encoding VE-cadherin carboxy-terminally tagged with GFP (VEC-GFP; Figure 1A). VEC-GFP, but not GFP, expressed in confluent HUVECs localized at the cell–cell contacts and seemed to form the zipper-like structures, as did endogenous VE-cadherin (Supplemental Figure 1A). On stimulation with FSK, VEC-GFP as well as endogenous VE-cadherin was linearly accumulated at the cell–cell contacts (Supplemental Figure 1A). Coimmunoprecipitation study using 293T cells revealed the ability of VEC-GFP to associate with α-catenin, β-catenin, and p120-catenin (Supplemental Figure 1B). These results indicate that VEC-GFP behaves similarly to endogenous VE-cadherin. Thus, we decided to use VEC-GFP as a tool to analyze the dynamics of VE-cadherin in living cells.

To investigate whether intracellular cAMP stabilizes VE-cadherin at the endothelial cell–cell contacts, we performed the FRAP analysis of VEC-GFP. We examined the fluorescence recovery at the photobleached region of the cell–cell junctions in the confluent HUVECs expressing VEC-GFP using a confocal time-lapse microscope. In control cells, fluorescence of VEC-GFP recovered to 74.3% of the original level (Figure 1, B–D), indicating that the mobile and immobile fractions of VEC-GFP at the cell–cell contacts are 74.3 and 25.7%, respectively (Figure 1D). Among the mobile fraction, the half-time of fluorescence recovery for VEC-GFP was 10.1 min (Figure 1E). On stimulation with FSK, the mobile fraction of VEC-GFP at cell–cell contacts was reduced to 55.3%, whereas the half-time of the fluorescence recovery was prolonged to 18.3 min (Figure 1, B–E). These results suggest that elevation of intracellular cAMP level induces the stabilization of VE-cadherin at the cell–cell contacts.

Intracellular cAMP regulates diverse cellular functions mainly through two downstream effectors; Epac and PKA. Therefore, we investigated which effectors are involved in cAMP-induced VE-cadherin stabilization at cell–cell contacts by using specific activators for PKA and Epac, 6-Bnz and 007, respectively. 007 but not 6-Bnz induced activation of Rap1, a small GTPase acting downstream of Epac, whereas 6-Bnz but not 007 induced phosphorylation of CREB, a direct PKA substrate, confirming their specificity (Figure 1F). The mobile fraction of VEC-GFP at the cell–cell contacts was decreased by 007 to the level observed in FSK-stimulated cells (Figure 1G). 007 prolonged the half-time of the fluorescence recovery of VEC-GFP (Figure 1H). In contrast, 6-Bnz did not affect the mobile fraction and recovery rate of junctional VEC-GFP (Figure 1, G and H). In addition, H89, a PKA-specific inhibitor, did not affect FSK-reduced mobile fraction of VEC-GFP, although it blocked FSK-induced CREB phosphorylation (Figure 1I and

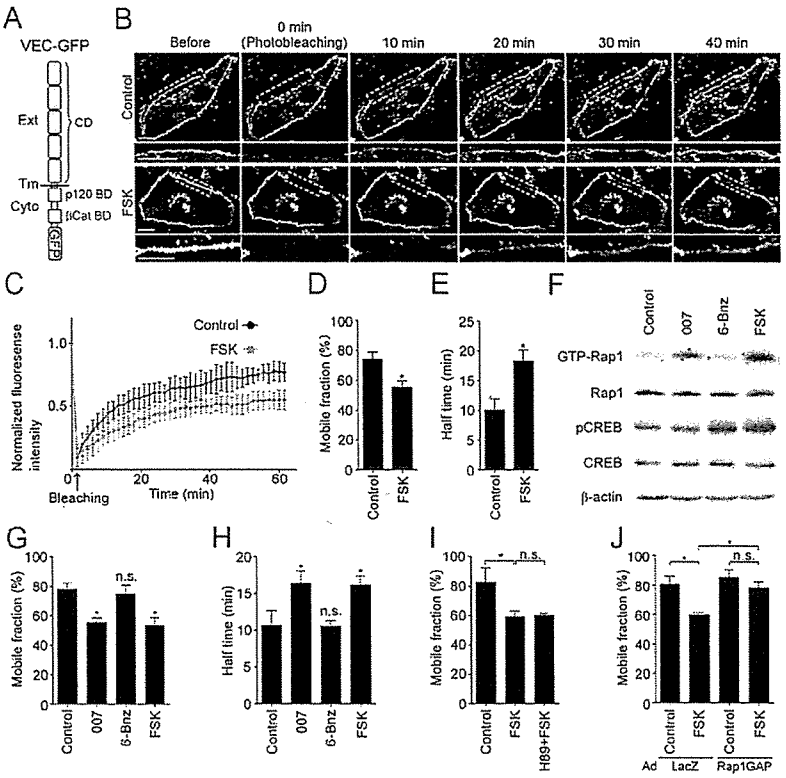

Figure 1. cAMP stabilizes VE-cadherin at cell–cell contacts through Epac, but not PKA. (A) Schematic illustration of VEC-GFP in which a GFP tag is fused to the carboxy terminus of full-length VE-cadherin. VE-cadherin consists of an extracellular region (Ext) consisting of five cadherin domains (CD), a transmembrane region (Tm), and a conserved cytoplasmic region (Cyto) containing p120–catenin-binding domain (p120 BD) and β-catenin-binding domain (βCat BD). (B) Confluent HUVECs plated on a collagen-coated glass-base dish were transfected with the plasmid encoding VEC-GFP. After 24 h, the cells were starved in medium 199 containing 1% BSA for 3 h and stimulated with vehicle (top, control) or 10 μM FSK (bottom) for 30 min. To measure the mobility of VEC-GFP at cell–cell junctions, GFP-positive cells surrounded by GFP-negative cells were selected and immediately subjected to FRAP analysis as described in *Materials and Methods*. Representative GFP images before and at the indicated time points after photobleaching are shown. Photobleached areas are marked by dotted rectangles and enlarged at the bottom of each image. Bar, 20 μm. (C) Quantitative analysis of FRAP experiments in B. Plot of normalized fluorescence intensity of VEC-GFP expressed in the cells stimulated with vehicle (control, black circles) or FSK (red squares) versus time (minutes) after photobleaching. Data are expressed as mean ± SD of five independent experiments. (D and E) The mobile fraction (D) and the recovery half-time (E) of VEC-GFP expressed in the cells stimulated with vehicle (control) or FSK were calculated from the fluorescence recovery curves shown in C. Data are expressed as mean ± SE of five independent experiments. (F) HUVECs starved in 0.5% BSA-containing medium 199 for 6 h were stimulated with either vehicle (control), 0.2 mM 007, 0.2 mM 6-Bnz, or 10 μM FSK for 15 min as indicated at the top. GTP-bound Rap1 was collected as described in *Materials and Methods* and subjected to Western blot analysis with anti-Rap1 antibody (GTP-Rap1). Aliquots of cell lysates were also subjected to Western blot analysis with anti-Rap1 (Rap1), anti-phospho-CREB (pCREB), anti-CREB (CREB), and anti-β-actin (β-actin) antibodies. (G and H) Confluent HUVECs expressing VEC-GFP were stimulated with vehicle (control), 0.2 mM 007, 0.2 mM 6-Bnz, or 10 μM FSK for 30 min and subjected to FRAP analysis as described in B. The mobile fraction of VEC-GFP (G) and its recovery half-time (H) were calculated similarly to D and E. Data are expressed as mean ± SE of six independent experiments. (I) Confluent HUVECs expressing VEC-GFP were starved in medium 199 containing 0.1% BSA for 3 h, treated with or without 10 μM H89 for 30 min, and subsequently stimulated with vehicle (control) or 10 μM FSK for 30 min as indicated at the bottom of each graph. The cells were then subjected to FRAP analysis as described in B. The mobile fraction of VEC-GFP was calculated similarly to D. (J) Confluent HUVECs plated on collagen-coated glass-base dish were transfected with the plasmid encoding VEC-GFP and infected with adenoviruses encoding either LacZ or Rap1GAP. After 24 h, the cells were starved, stimulated with FSK, and subsequently subjected to FRAP analysis as described in B. The mobile fraction of VEC-GFP was calculated similarly to D. Data are expressed as mean ± SE of four to five independent experiments. Significant differences from the control (D, E, G, and H) or between two groups (I and J) are indicated as $^*p < 0.05$. n.s. indicates no significance between two groups.

Supplemental Figure 2A). However, increased recovery rate of VEC-GFP observed in either FSK- or 007-stimulated cells was partially inhibited by H89 (Supplemental Figure 2B; data not shown). Thus, basal PKA activity may influence the mobility of VE-cadherin at cell–cell contacts. Furthermore, overexpression of Rap1GAP, a GTPase-activating protein for Rap1, not only prevented FSK-induced Rap1 activation but also inhibited FSK-decreased mobile fraction of junctional VEC-GFP and the FSK-prolonged half-time of its fluorescent recovery (Figure 1J and Supplemental Figure 2, C and D). Collectively, these results indicate that cAMP stabilizes VE-cadherin at cell–cell contacts through Epac–Rap1 pathway, but not PKA pathway.

Circumferential Actin Bundles Induced by cAMP Are Required for Stabilization of VE-Cadherin at the Endothelial Cell–Cell Contacts

Previously, we and others have reported that cAMP induces accumulation of polymerized actin at the endothelial cell–cell contacts (Fukuhara *et al.*, 2005; Kooistra *et al.*, 2005; Lorenowicz *et al.*, 2008). Thus, we decided to investigate whether reorganization of actin cytoskeleton is required for cAMP-mediated stabilization of VE-cadherin at cell–cell contacts. In control HUVECs, VE-cadherin formed zipper-like structures along the cell–cell junctions (Figure 2A). Staining with rhodamine-phalloidin revealed that actin stress fibers terminating at VE-cadherin-based cell–cell contacts were distributed through the cytoplasm (Figure 2A). Stimulation with either FSK or 007 reduced the central stress fibers and induced the formation of circumferential actin bundles along the cell–cell junctions (Figure 2, A and B). In these cells, VE-cadherin clearly concentrated along the circumferential actin bundles (Figure 2A). In contrast, PKA activation induced by 6-Bnz did not affect the organization of actin cytoskeleton and the localization of VE-cadherin (Figure 2, A and B). Furthermore, H89 inhibited neither FSK-induced formation of circumferential actin bundles nor

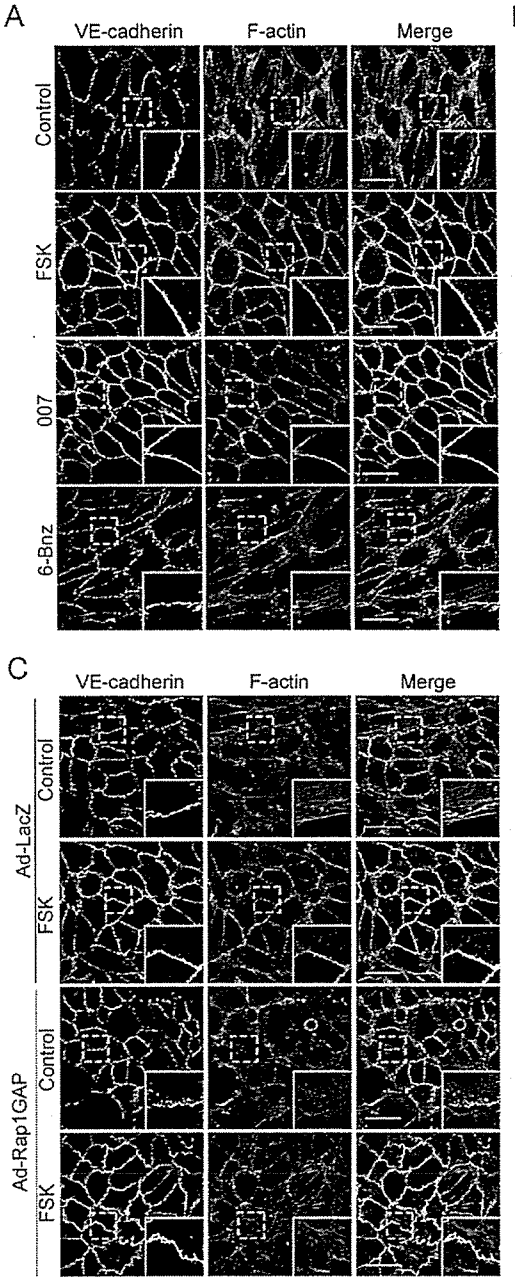

Figure 2. cAMP induces circumferential actin bundle formation and accumulation of VE-cadherin on the bundled actin filaments through an Epac-Rap1 pathway. (A) Monolayer-cultured HUVECs starved in 0.5% BSA-containing medium 199 for 3 h were stimulated with vehicle (top, control), 10 μM FSK (second panel), 0.2 mM 007 (third panel), and 0.2 mM 6-Bnz (bottom) for 30 min. After stimulation, the cells were fixed, immunostained with anti-VE-cadherin antibody and visualized with Alexa 488-conjugated secondary antibody. The cells were also stained with rhodamine-phalloidin to visualize F-actin. Alexa 488 and rhodamine images were obtained through a confocal microscope. Alexa 488 (VE-cadherin, green), rhodamine (F-actin, red) and the merged (merge) images are shown as indicated at the top of each column. The boxed areas marked by dotted line in the images are enlarged in the bottom right corner of each image. (B) Levels of F-actin at cell–cell contacts observed in A were quantified as described in *Materials and Methods*. Values are expressed as a percentage relative to that in the control cells and shown as mean ± SE of >80 contacts. Similar results were obtained in three independent experiments. (C) Confluent HUVECs were infected with adenoviruses encoding either LacZ (Ad-LacZ) or Rap1GAP (Ad-Rap1GAP) as indicated at the left. After 24 h, the cells were starved in 0.5% BSA-containing medium 199 for 3 h and stimulated with vehicle (control) or 10 μM FSK for 30 min. The cells were then stained with anti-VE-cadherin antibody and visualized with Alexa 488-conjugated secondary antibody as described in A. The cells were also stained with rhodamine-phalloidin to visualize F-actin. Alexa 488 (VE-cadherin, green), rhodamine (F-actin, red) and the merged (merge) images are shown as indicated at the top of each column. The boxed areas marked by dotted line in the images are enlarged in the bottom right corner of each image. (D) Levels of F-actin at cell–cell contacts observed in C were quantified similarly to B. Values are expressed as a percentage relative to that in the control cells infected with adenoviruses encoding LacZ and are shown as mean ± SE of >100 contacts. Similar results were obtained in three independent experiments. Bars, 50 μm (A and C). Significant differences from the control (B) or between two groups (D) are indicated as *$p < 0.05$. n.s. indicates no significance between two groups.

FSK-induced accumulation of VE-cadherin at the cell–cell contacts (Supplemental Figure 3). However, overexpression of Rap1GAP in HUVECs prevented FSK-induced circumferential actin bundling (Figure 2, C and D). Collectively, these findings suggest that a cAMP–Epac–Rap1 pathway induces circumferential actin bundling and accumulation of VE-cadherin on the bundled actin filaments.

It has been reported that circumferential actin filament networks are required for the maintenance of E-cadherin-based cell–cell contacts in epithelial cells (Quinlan and Hyatt, 1999; Kobielak and Fuchs, 2004; Mege *et al.*, 2006). Therefore, we investigated whether circumferential actin bundle formation is responsible for cAMP-induced accumulation of VE-cadherin at the cell–cell contacts. Treatment with 200 nM Lat.A, an inhibitor of actin polymerization (Spector *et al.*, 1989), resulted in not only disruption of central stress fibers in the control HUVECs expressing VEC-GFP but also in fragmentation of circumferential actin bundles formed upon stimulation with either FSK or 007 (Figure 3A). In these cells, VEC-GFP could not accumulate at the cell–cell junctions even when stimulated with FSK and 007 (Figure 3A). We further performed the FRAP analysis of VEC-GFP in the presence or absence of Lat.A; 100 nM Lat.A less suppressed FSK-induced circumferential actin bundling

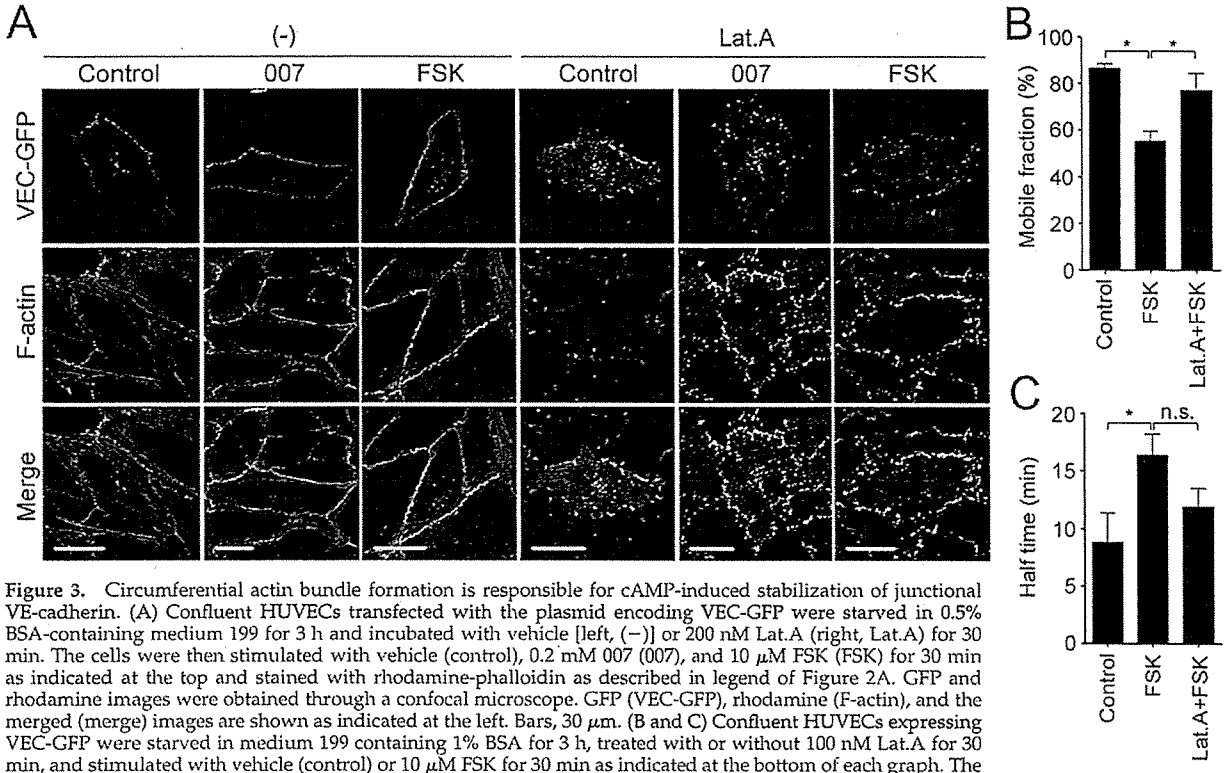

Figure 3. Circumferential actin bundle formation is responsible for cAMP-induced stabilization of junctional VE-cadherin. (A) Confluent HUVECs transfected with the plasmid encoding VEC-GFP were starved in 0.5% BSA-containing medium 199 for 3 h and incubated with vehicle [left, (−)] or 200 nM Lat.A (right, Lat.A) for 30 min. The cells were then stimulated with vehicle (control), 0.2 mM 007 (007), and 10 μM FSK (FSK) for 30 min as indicated at the top and stained with rhodamine-phalloidin as described in legend of Figure 2A. GFP and rhodamine images were obtained through a confocal microscope. GFP (VEC-GFP), rhodamine (F-actin), and the merged (merge) images are shown as indicated at the left. Bars, 30 μm. (B and C) Confluent HUVECs expressing VEC-GFP were starved in medium 199 containing 1% BSA for 3 h, treated with or without 100 nM Lat.A for 30 min, and stimulated with vehicle (control) or 10 μM FSK for 30 min as indicated at the bottom of each graph. The cells were then subjected to FRAP analysis as described in the legend of Figure 1B. The mobile fraction of VEC-GFP (B) and its recovery half-time (C) were calculated as described in the legend of Figure 1, D and E. Data are expressed as mean ± SE of five to seven independent experiments. Significant differences between two groups are indicated as *$p < 0.05$. n.s. indicates no significance between two groups.

and less decreased the junctional localization of VEC-GFP than 200 nM Lat.A (Supplemental Figure 4). Therefore, we tested the effect of Lat.A. on the stabilization of VE-cadherin at the cell–cell contacts by using the cells treated with 100 nM Lat.A. FSK-decreased mobile fraction of VEC-GFP at the cell–cell junctions and the FSK-prolonged half-time of its fluorescent recovery were partially inhibited by 100 nM Lat.A (Figure 3, B and C). These results suggest that the circumferential actin bundles induced by cAMP-Epac-Rap1 signal are required for stabilization of VE-cadherin at the cell–cell contacts.

The Circumferential Actin Bundling upon cAMP Stimulation Does Not Need Homophilic VE-Cadherin-based Cell–Cell Adhesions

The cytoplasmic region of cadherin binds β-catenin, which in turn associates with α-catenin (Ozawa and Kemler, 1992; Kemler, 1993). It has been shown that α-catenin coordinates actin dynamics at the sites of cadherin-based cell–cell contacts (Kobielak and Fuchs, 2004; Mege *et al.*, 2006; Weis and Nelson, 2006). Cadherin associates with p120-catenin through its juxtamembrane domain as well as β-catenin (Reynolds *et al.*, 1994). p120-catenin regulates actin cytoskeleton by controlling the activity of Rho family small GTPases (Reynolds, 2007). Thus, we hypothesized that a cAMP-Epac-Rap1 pathway initially promotes VE-cadherin–based cell–cell adhesions, which subsequently induce circumferential actin bundling through catenins. To test this hypothesis, we examined the effect of depletion of either VE-cadherin, α-catenin, β-catenin, or p120-catenin on actin reorganization. Depletion of either of them resulted in the disruption of central stress fibers and the induction of membrane ruffle formation close to the cell–cell contacts (Figure 4, A–D). These results suggest that central stress fiber formation depends on VE-cadherin/catenin complexes. However, unexpectedly FSK-induced circumferential actin bundling was not affected by depletion of VE-cadherin/catenin complexes (Figure 4, A–D, and Supplemental Figure 5, A–D). Furthermore, we examined the effect of extracellular Ca^{2+} chelation on FSK-induced circumferential actin bundling, because cadherin-dependent cell adhesion requires extracellular Ca^{2+}. FSK apparently induced formation of circumferential actin bundles even in the presence of EGTA (Supplemental Figure 6), although VE-cadherin disappeared from the cell–cell border in the presence of EGTA even when the cells were stimulated with FSK (Supplemental Figure 6). These results clearly indicate that cAMP-induced circumferential actin bundling does not require VE-cadherin/catenin complex-dependent reorganization of actin cytoskeleton.

α- and β-Catenins Are Required for cAMP-induced Accumulation of VE-Cadherin at Cell–Cell Contacts

It had been believed that cadherin–β-catenin complex is physically linked with actin fibers via α-catenin, although this model is recently challenged by the report that α-catenin dose not bind simultaneously to both the cadherin–β-catnin complex and the actin fibers (Yamada *et al.*, 2005; Drees *et al.*, 2005; Gates and Peifer, 2005). To test the requirement of α- and β-catenins in cAMP-induced accumulation of VE-cadherin at the cell–cell contacts, we examined the effect of

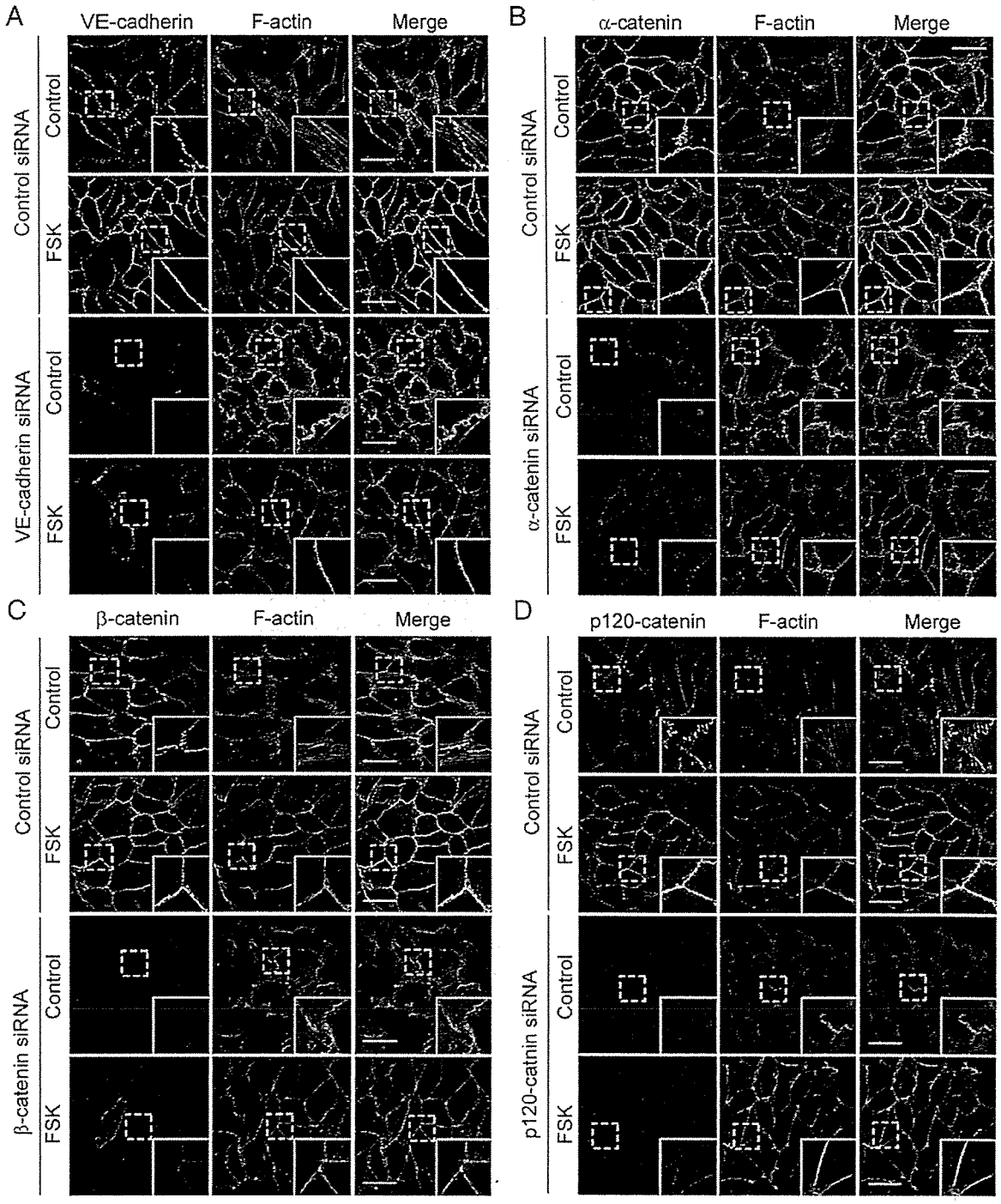

Figure 4. cAMP-induced circumferential actin bundling does not depend upon VE-cadherin–based cell–cell adhesions. (A–D) HUVECs were transfected with control siRNA (top panels of each figure) or with siRNAs targeting against VE-cadherin (A), α-catenin (B), β-catenin (C), and p120-catenin (D) (bottom panels of each figure), cultured for 48 h, and replated onto the collagen-coated glass-base dish. After 24 h, the cells were starved in medium 199 containing 0.5% BSA for 3 h and stimulated with vehicle (control) or 10 μM FSK for 30 min as indicated at the left of each figure. The cells were stained with anti-VE-cadherin (A), anti-α-catenin (B), anti-β-catenin (C), and anti-p120-catenin (D) antibodies and visualized with Alexa 488-conjugated secondary antibody as described in Figure 2A. The cells were also stained with rhodamine-phalloidin to visualize F-actin. Alexa 488 and rhodamine images were obtained through a confocal microscope. Alexa 488 images for VE-cadherin (A), α-catenin (B), β-catenin (C), and p120-catenin (D) are shown at the left column. Rhodamine (F-actin) and the merged (merge) images are shown at the middle and right columns, respectively. The boxed areas marked by dotted line in the images are enlarged in the bottom right corner of each image. Bars, 50 μm.

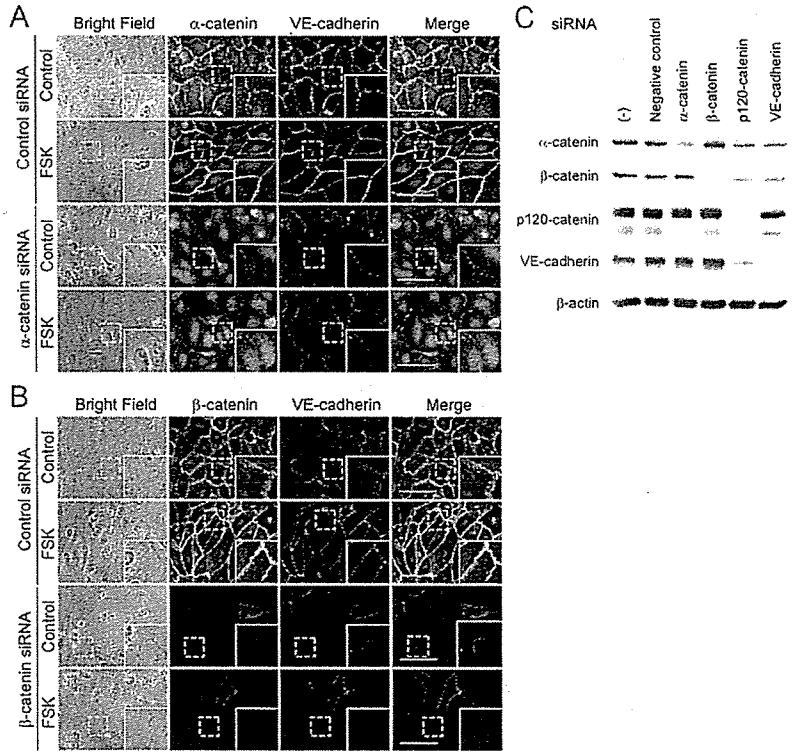

Figure 5. α- and β-Catenins are essential for cAMP-induced accumulation of VE-cadherin at cell–cell contacts. (A and B) HUVECs were transfected with control siRNA (top panels of each figure) or with siRNAs targeting against α-catenin (A) and β-catenin (B) (bottom panels of each figure) and stimulated with vehicle (control) or FSK as described in the legend of Figure 4. The cells were immunostained with either anti-α-catenin (A) or anti-β-catenin (B) antibody and with anti-VE-cadherin antibody and then visualized with Alexa 488- and Alexa 546-conjugated secondary antibodies, respectively. Phase contrast, Alexa 488 and Alexa 546 images were obtained using an IX81 inverted microscope (Olympus). Phase contrast (bright field), Alexa 488 (α-catenin in A and β-catenin in B), Alexa 546 (VE-cadherin), and the merged (merge) images are shown as indicated at the top of each column. The boxed areas marked by dotted line in the images are enlarged in the lower right corner of each image. Bars, 30 μm. (C) HUVECs were transfected without [(−)] or with control siRNA (negative control) or siRNAs targeting α-catenin, β-catenin, p120-catenin, and VE-cadherin as indicated at the top and cultured for 72 h. Cell lysates were subjected to Western blot analysis with anti-α-catenin, anti-β-catenin, anti-p120-catenin, anti-VE-cadherin, and anti-β-actin antibodies as indicated at the left.

depletion of catenins on the accumulation of VE-cadherin. Depletion of either α- or β-catenin weakened not only the junctional localization of VE-cadherin in control HUVECs but also the FSK-induced accumulation of VE-cadherin at cell–cell contacts without affecting the expression level of VE-cadherin (Figure 5, A–C, and Supplemental Figure 7, A and B). Knockdown of p120-catenin by siRNA also resulted in disappearance of VE-cadherin at cell–cell contacts in either control- or FSK-stimulated cells but possibly due to the primarily down-regulated expression of VE-cadherin (Figure 5C and Supplemental Figure 8). These results indicate that α- and β-catenins are responsible for cAMP-induced accumulation of VE-cadherin at the cell–cell contacts and suggest that α- and β-catenins mediate the physical link between actin and VE-cadherin.

cAMP Induces Formation of Circumferential Actin Bundles, Which Anchor Junctional VE-Cadherin through α- and β-Catenins

To confirm that α- and β-catenins mediate physical link between actin and VE-cadherin in cAMP–Epac–Rap1 signal-activated endothelial cells, we decided to examine the localization and dynamics of the mutants of VE-cadherin in which the cytoplasmic domain was modified. We also constructed the plasmids encoding the mutants of VEC-GFP (Figure 6A and Supplemental Figure 9, A and B): VECΔβ-GFP in which the β-catenin binding domain is deleted, VECΔC-GFP in which the cytoplasmic domain is deleted, VECΔC-α-GFP in which the cytoplasmic domain is replaced with α-catenin, and VECΔC-αΔN–GFP in which the cytoplasmic domain is replaced with α-catenin lacking N-terminal β-catenin binding domain. When these expression plasmids were transfected into HUVECs, all VEC-GFP mutants as well as wild type VEC-GFP localized at cell–cell contacts (Figure 6B and Supplemental Figure 9C). FACS analysis revealed that their expression levels are similar (Supplemental Figure 9D). Stimulation with FSK resulted in accumulation of wild-type VEC-GFP on the circumferential actin bundles (Figure 6B). When the cells expressing either VECΔβ-GFP or VECΔC-GFP were stimulated with FSK, circumferential actin bundling occurred. However, neither of them could accumulate on the bundled actin filaments and was broadly distributed around the cell–cell junctions (Figure 6B). In contrast, VECΔC-α-GFP clearly concentrated on the circumferential actin bundles formed upon the stimulation with FSK (Figure 6B). Similarly, VECΔC-αΔN-GFP also accumulated on the bundled actin filaments in FSK-stimulated cells (Figure 6B). Together with the evidence that VECΔC-αΔN-GFP was incapable of associating with β-catenin (Supplemental Figure 9E), these results indicate that the ability of VE-cadherin/α-catenin chimera to concentrate on the circumferential actin bundles is not due to α-catenin acting as a β-catenin binding site. Consistently, VECΔC-α-GFP, but not VEC-GFP, could accumulate on the bundled actin filaments even in the β-catenin–depleted cells (Supplemental Figure 10, B and D). Furthermore, depletion of α-catenin by siRNA did not affect the accumulation of VECΔC-α-GFP on the bundled actin filaments, although α-catenin was required for the localization of VEC-GFP on the actin bundles (Supplemental Figure 10, A and C). Collectively, these results indicate that α- and β-catenins localize VE-cadherin to the circumferential actin bundles.

Furthermore, we performed FRAP analyses of VEC-GFP mutants. FSK significantly reduced the mobile fractions of VEC-GFP, VECΔC-α-GFP, and VECΔC-αΔN-GFP at the cell–cell contacts and prolonged the half-time of their fluo-

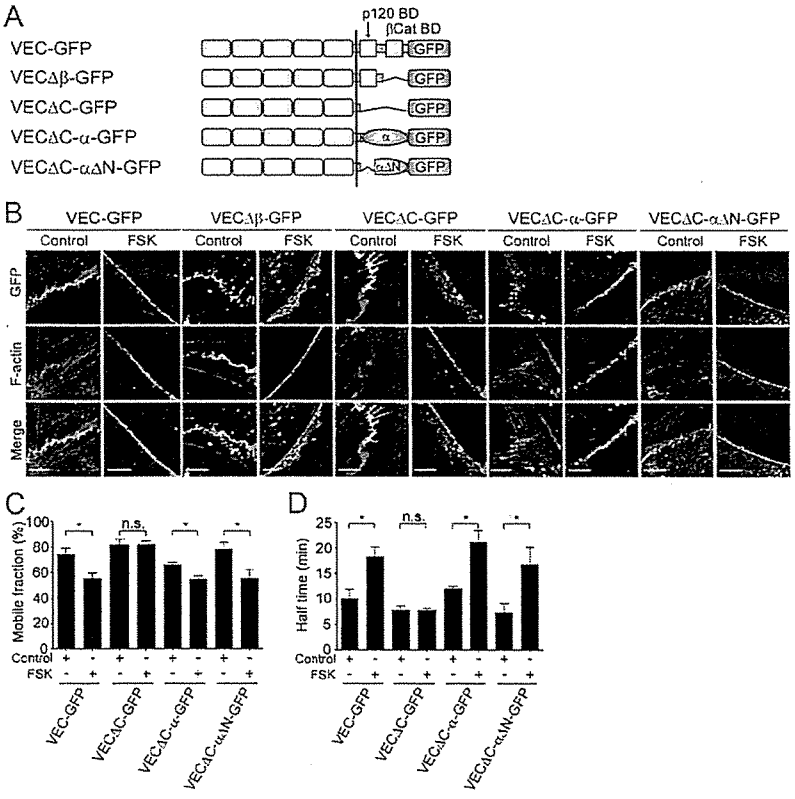

Figure 6. α- and β-Catenins locate and stabilize VE-cadherin at the circumferential actin bundles. (A) Schematic illustrations of VEC-GFP and its mutants. VEC-GFP, VE-cadherin carboxy-terminally tagged with GFP; VEC-GFPΔβ-GFP, a VEC-GFP mutant lacking the β-catenin binding domain of VE-cadherin; VEC-ΔC-GFP, a VEC-GFP mutant lacking the cytoplasmic region of VE-cadherin; VECΔC-α-GFP, a VEC-GFP mutant in which the cytoplasmic region of VE-cadherin is replaced with α-catenin; and VECΔC-αΔN-GFP, a VEC-GFP mutant in which the cytoplasmic region of VE-cadherin is replaced with α-catenin lacking N-terminal β-catenin binding domain. (B) HUVECs were transfected with the plasmid encoding either VEC-GFP or its mutant as indicated at the top. The cells were starved in medium 199 containing 0.5% BSA for 3 h and stimulated with vehicle (control) or 10 μM FSK (FSK) for 30 min. The cells were stained with rhodamine-phalloidin to visualize F-actin as described in the legend of Figure 2A. GFP and rhodamine images were obtained through a confocal microscope. GFP, rhodamine (F-actin), and the merged (merge) images are shown as indicated at the left. The border between the untransfected cell and the cell expressing GFP tagged-VE-cadhein is shown. Bars, 5 μm. (C and D) Confluent HUVECs plated on collagen-coated glass-base dish were transfected with the plasmid encoding VEC-GFP, VECΔC-GFP, VECΔC-α-GFP, or VECΔC-αΔN-GFP as indicated at the bottom of each figure. The cells were starved, stimulated with vehicle (control) or 10 μM FSK for 30 min, and subjected to FRAP analysis as described in the legend of Figure 1B. The mobile fraction of VEC-GFP and its mutants (C) and their recovery half-time (D) were calculated as described in the legend of Figure 1, D and E. Data are expressed as mean ± SE of six to eight independent experiments. Significant differences between two groups are indicated as $^*p < 0.05$. n.s. indicates no significance between two groups.

rescence recovery (Figure 6, C and D). Effect of FSK on the stability of VECΔC-α-GFP as well as VEC-GFP at cell–cell contacts was canceled by treatment with 100 nM Lat.A (Figure 3, B and C, and Supplemental Figure 11, A and B). In clear contrast, the mobile fraction of junctional VECΔC-GFP and its recovery rate were unaffected by stimulation with FSK (Figure 6, C and D). Collectively, these results strongly suggest that anchoring of VE-cadherin to circumferential actin bundles through α- and β-catenins results in the stabilization of VE-cadherin at cell–cell junctions.

PECAM1 is an immunoglobulin-family cell adhesion molecule expressed in endothelial cells and localized at cell–cell junctions (Woodfin *et al.*, 2007). However, unlike VE-cadherin, localization of PECAM1 is not confined to the AJs because it is incapable of associating with actin cytoskeleton. Indeed, PECAM1 did not accumulate on the circumferential actin bundles in FSK-stimulated HUVECs (Figure 7A), which is reminiscent of the localization of VECΔC-GFP and VECΔβ-GFP. Thus, we assumed that the importance of the link between actin and VE-cadherin through α- and β-catenins for the stabilization of VE-cadherin can be claimed by comparing the localization and dynamics of VE-cadherin to those of PECAM1. To this end, we constructed the plasmid encoding PECAM1 carboxy-terminally tagged with GFP (PECAM1-GFP) and those encoding its mutants (Figure 7B and Supplemental Figure 9, A–D); PECAM1ΔC-GFP in which the cytoplasmic region is deleted, PECAM1ΔC-α-GFP in which the cytoplasmic region is replaced with α-catenin and PECAM1ΔC-VEC/C-GFP in which the cytoplasmic region is replaced with that of VE-cadherin. As expected, PECAM1-GFP and PECAM1ΔC-GFP were broadly localized around the cell–cell junctions, irrespective of the presence or absence of circumferential actin bundles upon stimulation with FSK (Figure 7C). Consistently, FSK did not affect the mobile fractions of PECAM1-GFP and PECAM1ΔC-GFP at the cell–cell contacts and their recovery rate (Figure 7, D and E). In contrast, PECAM1ΔC-α-GFP and PECAM1ΔC-VEC/C-GFP clearly accumulated on the circumferential actin bundles in the FSK-stimulated cells (Figure 7C). FSK-induced concentration of PECAM1ΔC-α-GFP on the bundled actin filaments occurred even in the β-catenin–depleted cells (Supplemental Figure 12). Furthermore, the mobile fraction of PECAM1ΔC-α-GFP was significantly reduced by stimulation with FSK, although FSK did not affect its recovery rate (Figure 7, D and E), possibly due to the interaction with endogenous PECAM1. These findings indicate that α- and β-catenins have potential to locate VE-cadherin to the circumferential actin bundles induced by a cAMP–Epac–Rap1 signal and to stabilize VE-cadherin at the cell–cell contacts.

DISCUSSION

We found that a cAMP-Epac–Rap1 signal initially induces circumferential actin bundle formation independently of VE-cadherin/catenin complexes and that α- and β-catenins have potential to locate VE-cadherin to the bundled actin and to stabilize VE-cadherin at the cell–cell contacts. cAMP

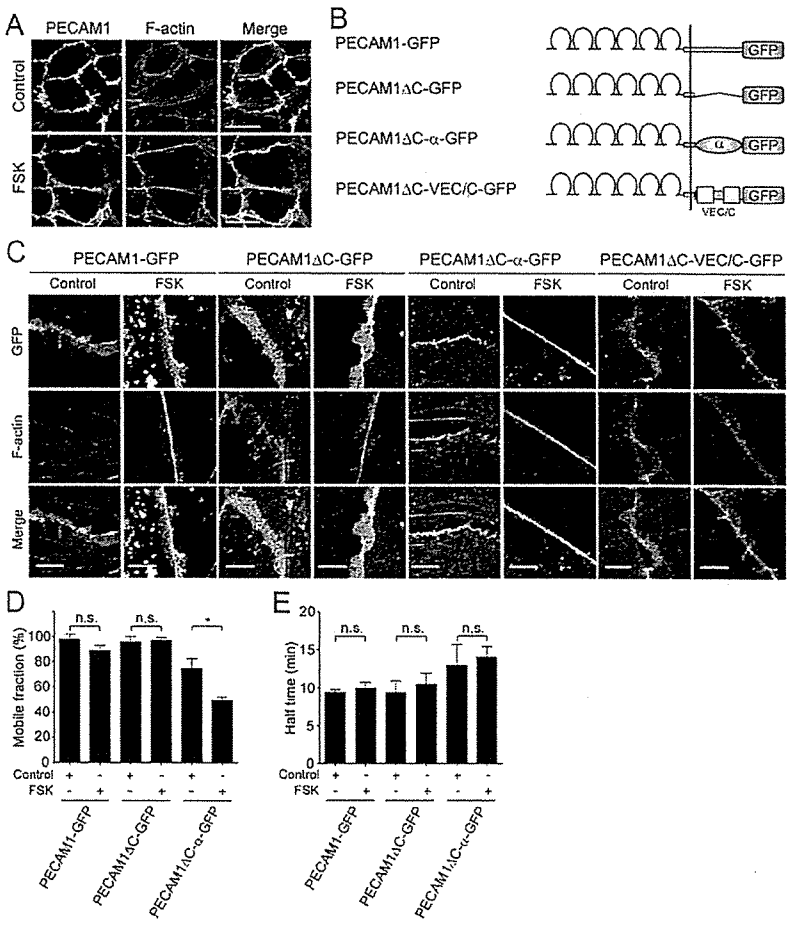

Figure 7. PECAM1 that is incapable of associating with actin cytoskeleton is not stabilized on the circumferential actin bundles. (A) Monolayer-cultured HUVECs were stimulated with vehicle (top, control) or 10 μM FSK (bottom) for 30 min as described in the legend of Figure 2A. After stimulation, the cells were immunostained with anti-PECAM1 antibody and visualized with Alexa 488-conjugated secondary antibody. The cells were also stained with rhodamine-phalloidin to visualize F-actin. Alexa 488 and rhodamine images were obtained through a confocal microscope. Alexa 488 (PECAM1), rhodamine (F-actin), and the merged (merge) images are shown as indicated at the top of each column. (B) Schematic illustrations of PECAM1-GFP and its mutants. PECAM1-GFP, PECAM1 carboxy-terminally tagged with GFP; PECAM1ΔC-GFP, a PECAM1-GFP mutant lacking the cytoplasmic region of PECAM1; PECAM1ΔC-α-GFP, a PECAM1-GFP mutant in which the cytoplasmic region of PECAM1 is replaced with α-catenin; and PECAM1ΔC-VEC/C-GFP, a PECAM1-GFP mutant in which the cytoplasmic region of PECAM1 is replaced with that of VE-cadherin. (C) HUVECs were transfected with the plasmid encoding either PECAM1-GFP or its mutant as indicated at the top. The cells were stimulated with vehicle (control) or 10 μM FSK and stained with rhodamine-phalloidin similarly to the legend of Figure 6B. GFP and rhodamine images were obtained through a confocal microscope. GFP, rhodamine (F-actin), and, the merged (merge) images are shown as indicated at the left. The border between the untransfected cell and the cell expressing GFP tagged-PECAM1 is shown. (D and E) Confluent HUVECs plated on a collagen-coated glass-base dish were transfected with the plasmid encoding PECAM1-GFP, PECAM1ΔC-GFP, or PECAM1ΔC-α-GFP as indicated at the bottom of each graph. The cells were starved, stimulated with vehicle (control) or 10 μM FSK for 30 min, and subjected to FRAP analysis as described in the legend of Figure 1B. The mobile fraction of PECAM1-GFP and its mutants (D) and their recovery half-time (E) were calculated as described in the legend of Figure 1, D and E. Data are expressed as mean ± SE of five to six independent experiments. Significant differences between two groups are indicated as *$p < 0.05$. n.s. indicates no significance between two groups. Bars, 30 μm (A) and 5 μm (C).

is a well-known intracellular second messenger that is capable of promoting endothelial barrier function through both PKA and Epac (Yuan, 2002; Cullere *et al.*, 2005; Fukuhara *et al.*, 2005; Kooistra *et al.*, 2005; Pannekoek *et al.*, 2009). Previously, we and others have reported that cAMP potentiates VE-cadherin–based cell–cell adhesions through an Epac–Rap1 pathway (Cullere *et al.*, 2005; Fukuhara *et al.*, 2005; Kooistra *et al.*, 2005). Thus, circumferential actin bundling induced by cAMP–Epac–Rap1 signal is essential for endothelial barrier function mediated by VE-cadherin.

The mechanism how stabilization of VE-cadherin is regulated in cAMP–Epac–Rap1 signal-activated endothelial cells fits the classical static model: Catenin tethers cadherin to actin cytoskeleton. The cadherin–β-catenin complex has been believed to be physically linked with actin cytoskeleton directly or indirectly through α-catenin, which is responsible for maintenance of AJs (Nagafuchi *et al.*, 1994; Rimm *et al.*, 1995; Sako *et al.*, 1998; Watabe-Uchida *et al.*, 1998; Imamura *et al.*, 1999). However, the Weis and Nelson groups have recently suggested a new dynamic model in which α-catenin does not statically link cadherin to actin but directly regulates actin dynamics at the cell–cell contacts by demonstrating that α-catenin does not associate with the cadherin–β-catenin complex and with cytoskeleton simultaneously (Drees *et al.*, 2005; Gates and Peifer, 2005; Yamada *et al.*, 2005). By performing FRAP analysis of GFP-tagged E-cadherin (E-cadherin-GFP), they showed that ~80% of E-cadherin-GFP is immobilized at cell–cell contacts in epithelial cells. However, the mobility of junctional E-cadherin-GFP was not affected by disruption of actin cytoskeleton. In addition, a mutant of E-cadherin-GFP lacking its cytoplasmic domain had a mobility fraction similar to that of the full-length E-cadherin-GFP. These observations suggest that anchoring to actin cytoskeleton through α- and β-catenins does not contribute to the stabilization of E-cadherin at cell–cell junctions. In clear contrast to their findings, we found that >70% of VE-cadherin is mobile at the cell–cell contacts in unstimulated endothelial cells under confluent culture and that elevation of intracellular cAMP level reduced the mobile fraction of junctional VEC-GFP, which was significantly inhibited by disruption of actin cytoskeleton. Furthermore, elevation of intracellular cAMP level did not affect the mobile fractions of VECΔC-GFP but decreased that of VECΔC-α-GFP. These results indicate that a stable linkage

between VE-cadherin and actin bundles mediated by α- and β-catenins is responsible for cAMP-induced stabilization of VE-cadherin at cell–cell contacts.

α- and β-Catenins might indirectly tether VE-cadherin to bundled actin. α-catenin is known to interact with various actin binding proteins including vinculin, α-actinin, spectrin, zonula occludins-1, and afadin (Kobielak and Fuchs, 2004). Therefore, these proteins may mediate linkage of the cadherin–catenin complex to actin cytoskeleton. Consistently, Abe and Takeichi (2007) have recently reported that EPLIN binds α-catenin and actin filaments simultaneously, thereby linking the cadherin–catenin complex to the actin cytoskeleton. Because EPLIN is expressed not only in epithelial cells but also in endothelial cells (our unpublished data), VE-cadherin–β-catenin–α-catenin complex may be anchored to circumferential actin bundles through EPLIN.

We noticed that homophilic VE-cadherin–based cell–cell adhesion is not the trigger for promoting circumferential actin bundling in cAMP–Epac–Rap1 signal-activated cells. It has been reported that α-catenin directly regulates actin dynamics instead of simply linking the cadherin–β-catenin complex to actin cytoskeleton (Kobielak and Fuchs, 2004; Mege *et al.*, 2006; Weis and Nelson, 2006). The Weis and Nelson groups have shown that α-catenin homodimer competes with the Arp2/3 complex for binding to actin filaments, thereby inhibiting branching nucleation of actin filaments, instead promoting formation of linear actin bundles (Drees *et al.*, 2005; Gates and Peifer, 2005). EPLIN also acts not only in linking the cadherin–catenin complex to actin bundles but also in actively stabilizing these bundles (Abe and Takeichi, 2007). Furthermore, it has been reported that α-catenin locates several actin regulators such as formin-1, vinculin and Ena/VASP to the nascent AJs, thereby inducing formation of radial actin cables (Watabe-Uchida *et al.*, 1998; Weiss *et al.*, 1998; Vasioukhin *et al.*, 2001; Kobielak and Fuchs, 2004; Kobielak *et al.*, 2004). These results indicate that cadherin-based cell–cell adhesions coordinate actin dynamics at cell–cell junctions through α-catenin. Consistently, we found that VE-cadherin–based cell–cell adhesions are responsible for formation of central stress fibers in unstimulated cells. However, FSK-induced circumferential actin bundling was not inhibited by the depletion of either VE-cadherin, β-catenin, α-catenin, or p120-catenin or by disruption of cadherin-dependent cell adhesions by extracellular Ca^{2+} chelation. This result is consistent with the previous report that VE-cadherin–specific blocking antibody does not affect 007-induced actin remodeling in endothelial cells (Kooistra *et al.*, 2005). Thus, these findings demonstrate that circumferential actin bundling induced by cAMP signal does not require VE-cadherin–based cell–cell adhesions.

How does cAMP-Epac-Rap1 signal induce reorganization of actin cytoskeleton at endothelial cell–cell contacts? It has been reported that Rap1 promotes cell spreading by localizing a subset of Rac guanine nucleotide exchange factors such as Vav2 and Tiam1 to sites of active lamellipodia extension (Arthur *et al.*, 2004). Consistently, Rac has been shown to be involved in cAMP-induced endothelial barrier function (Birukova *et al.*, 2007; Baumer *et al.*, 2008). Thus, cAMP-induced Rap1 activation at cell–cell contacts may lead to the local activation of Rac, thereby inducing circumferential actin bundling. Indeed, our previous report revealed that Rap1 is activated at endothelial cell–cell contacts (Sakurai *et al.*, 2006). In addition, other Rap1 effectors such as K-Rev Interaction Trapped gene-1 and AF-6 may also be involved in cAMP-induced actin bundling (Boettner *et al.*, 2000, 2003; Glading *et al.*, 2007). Furthermore, it still remains unknown how cAMP signal locally regulates actin dynamics at cell–cell junctions. Because VE-cadherin–based cell–cell adhesions are dispensable for cAMP-induced actin bundling, other cell adhesion molecules may be involved in local regulation of actin dynamics. One of the candidates is nectin that is involved in formation of AJs in epithelial cells (Takai *et al.*, 2008), although its function in endothelial cells is still unknown. Thus, further studies are required to elucidate the molecular mechanisms by which a cAMP–Epac–Rap1 pathway induces circumferential actin bundling.

Intracellular cAMP activates two downstream effectors Epac and PKA, both of which are known to enhance endo-

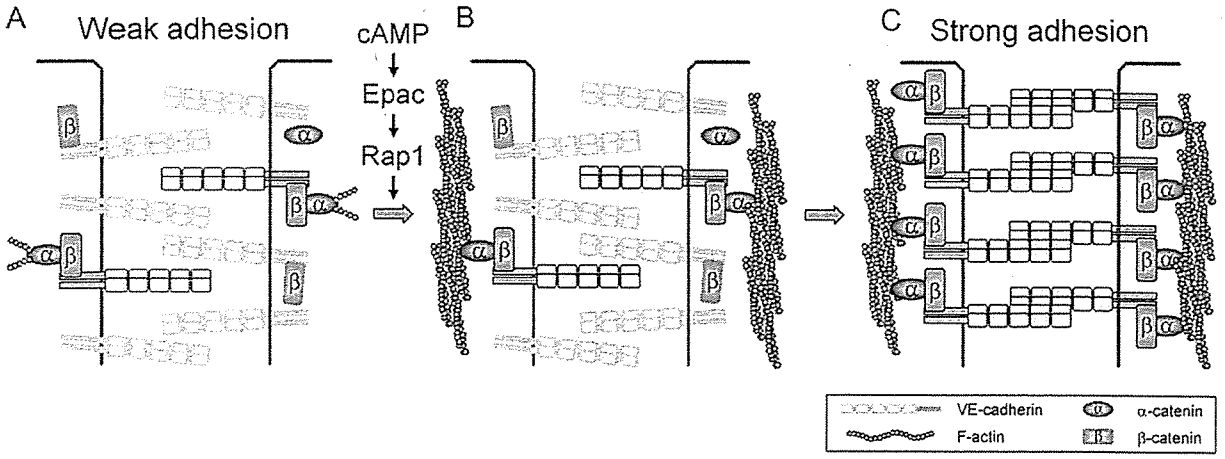

Figure 8. Schematic representation of our proposed model that accounts for how VE-cadherin is stabilized at the cell–cell contacts in cAMP–Epac–Rap1 signal-activated endothelial cells. (A) In unstimulated endothelial cells, the majority of VE-cadherin molecules (~75%) is mobile at cell–cell junctions, possibly due to the lack of circumferential actin bundles. VE-cadherin that does not associate with actin cytoskeleton has weak cell–cell adhesion activity. (B) When cAMP-Epac-Rap1 signal is activated, circumferential actin bundling occurs independently of VE-cadherin-based cell–cell adhesions. (C) Subsequently, α- and β-catenins link VE-cadherin to the bundled actin filaments, thereby stabilizing VE-cadherin at cell–cell contacts. Stabilization of VE-cadherin on the bundled actin filaments results in strong cell–cell adhesions. VE-cadherin that associates with bundled actin filaments through α- and β-catenins is outlined. α- and β-Catenins which link VE-cadherin to the bundled actin filaments are also outlined.

thelial barrier functions. In this study, we clearly indicate that PKA activation by 6-Bnz does not induce circumferential actin bundling and does not enhance stability of VE-cadherin at cell–cell contacts. Recently, Lorenowicz *et al.* (2008) have reported that Epac promotes the formation of cortical actin bundles, whereas PKA induces formation of stress fibers, although activation of either cAMP effector decreases endothelial permeability. Therefore, Epac and PKA may regulate endothelial barrier function through distinct signaling mechanisms.

In conclusion, we have demonstrated that circumferential actin bundle formation and subsequent linkage between actin bundles and VE-cadherin through α- and β-catenins are responsible for the stabilization of VE-cadherin at the cell–cell contacts in cAMP–Epac-Rap1 signal-activated cells (Figure 8). These findings strongly support the classical model that α-catenin is required for statically linking cadherin–β-catenin complexes to bundled actin filaments to maintain AJs.

ACKNOWLEDGMENTS

We are grateful to A. Nagafuchi (Kumamoto University) for the expression plasmid encoding α-catenin and helpful advice; to S. Hattori (University of Tokyo) and M. Matsuda (Kyoto University) for adenoviruses; to K. Matsuo, M. Sone, M. Minamimoto, and Y. Matsuura for technical assistance; and to J. T. Pearson for critical reading of the manuscript. This work was supported in part by grants from the Ministry of Education, Science, Sports and Culture of Japan (to S. F. and N. M.); the Ministry of Health, Labor, and Welfare of Japan (to N. M.); the Program for the Promotion of Fundamental Studies in Health Sciences of the National Institute of Biomedical Innovation (to S. F. and N. M.); the Naito Foundation (to S. F.); Takeda Science Foundation (to S. F. and N. M.); the Sagawa Foundation for Promotion of Cancer Research (to S. F.); Mochida Memorial Foundation for Medical and Pharmaceutical Research (to S. F.); Kowa Life Science Foundation (to S. F.); Kanae Foundation for the Promotion of Medical Science (to S. F.); The Novartis Foundation (Japan) for the Promotion of Science (to S. F.); Senri Life Science Foundation (to S. F.); the Mitsubishi Foundation (to N. M.); and AstraZeneca (to N. M.).

REFERENCES

Abe, K., and Takeichi, M. (2007). EPLIN mediates linkage of the cadherin catenin complex to F-actin and stabilizes the circumferential actin belt. Proc. Natl. Acad. Sci. USA *105*, 13–19.

Adamson, R. H., Ly, J. C., Sarai, R. K., Lenz, J. F., Altangerel, A., Drenckhahn, D., and Curry, F. E. (2008). Epac/Rap1 pathway regulates microvascular hyperpermeability induced by PAF in rat mesentery. Am. J. Physiol. Heart Circ. Physiol. *294*, H1188–H1196.

Andriopoulou, P., Navarro, P., Zanetti, A., Lampugnani, M. G., and Dejana, E. (1999). Histamine induces tyrosine phosphorylation of endothelial cell-to-cell adherens junctions. Arterioscler. Thromb. Vasc. Biol. *19*, 2286–2297.

Arthur, W. T., Quilliam, L. A., and Cooper, J. A. (2004). Rap1 promotes cell spreading by localizing Rac guanine nucleotide exchange factors. J. Cell Biol. *167*, 111–122.

Augustin, H. G., Young, K. G., Thurston, G., and Alitalo, K. (2009). Control of vascular morphogenesis and homeostasis through the angiopoietin-Tie system. Nat. Rev. Mol. Cell Biol. *10*, 165–177.

Baumer, Y., Drenckhahn, D., and Waschke, J. (2008). cAMP induced Rac 1-mediated cytoskeletal reorganization in microvascular endothelium. Histochem. Cell Biol. *129*, 765–778.

Birukova, A. A., Liu, F., Garcia, J. G., and Verin, A. D. (2004). Protein kinase A attenuates endothelial cell barrier dysfunction induced by microtubule disassembly. Am. J. Physiol. Lung Cell Mol. Physiol. *287*, L86–L93.

Birukova, A. A., Zagranichnaya, T., Fu, P., Alekseeva, E., Chen, W., Jacobson, J. R., and Birukov, K. G. (2007). Prostaglandins PGE(2) and PGI(2) promote endothelial barrier enhancement via PKA- and Epac1/Rap1-dependent Rac activation. Exp. Cell Res. *313*, 2504–2520.

Boettner, B., Govek, E. E., Cross, J., and Van Aelst, L. (2000). The junctional multidomain protein AF-6 is a binding partner of the Rap1A GTPase and associates with the actin cytoskeletal regulator profilin. Proc. Natl. Acad. Sci. USA *97*, 9064–9069.

Boettner, B., Harjes, P., Ishimaru, S., Heke, M., Fan, H. Q., Qin, Y., Van Aelst, L., and Gaul, U. (2003). The AF-6 homolog canoe acts as a Rap1 effector during dorsal closure of the *Drosophila* embryo. Genetics *165*, 159–169.

Cullere, X., Shaw, S. K., Andersson, L., Hirahashi, J., Luscinskas, F. W., and Mayadas, T. N. (2005). Regulation of vascular endothelial barrier function by Epac, a cAMP-activated exchange factor for Rap GTPase. Blood *105*, 1950–1955.

Dejana, E. (2004). Endothelial cell-cell junctions: happy together. Nat. Rev. Mol. Cell. Biol. *5*, 261–270.

Dejana, E., Tournier-Lasserve, E., and Weinstein, B. M. (2009). The control of vascular integrity by endothelial cell junctions: molecular basis and pathological implications. Dev. Cell *16*, 209–221.

Dejana, E., Orsenigo, F., and Lampugnani, M. G. (2008). The role of adherens junctions and VE-cadherin in the control of vascular permeability. J. Cell Sci. *121*, 2115–2122.

Drees, F., Pokutta, S., Yamada, S., Nelson, W. J., and Weis, W. I. (2005). Alpha-catenin is a molecular switch that binds E-cadherin-beta-catenin and regulates actin-filament assembly. Cell *123*, 903–915.

Ebnet, K., Suzuki, A., Ohno, S., and Vestweber, D. (2004). Junctional adhesion molecules (JAMs): more molecules with dual functions? J. Cell Sci. *117*, 19–29.

Farmer, P. J., Bernier, S. G., Lepage, A., Guillemette, G., Regoli, D., and Sirois, P. (2001). Permeability of endothelial monolayers to albumin is increased by bradykinin and inhibited by prostaglandins. Am. J. Physiol. Lung Cell Mol. Physiol. *280*, L732–L738.

Fukuhara, S., Sako, K., Minami, T., Noda, K., Kim, H. Z., Kodama, T., Shibuya, M., Takakura, N., Koh, G. Y., and Mochizuki, N. (2008). Differential function of Tie2 at cell-cell contacts and cell-substratum contacts regulated by angiopoietin-1. Nat. Cell Biol. *10*, 513–526.

Fukuhara, S., Sako, K., Noda, K., Nagao, K., Miura, K., and Mochizuki, N. (2009). Tie2 is tied at the cell-cell contacts and to extracellular matrix by angiopoietin-1. Exp. Mol. Med. *41*, 133–139.

Fukuhara, S., Sakurai, A., Sano, H., Yamagishi, A., Somekawa, S., Takakura, N., Saito, Y., Kangawa, K., and Mochizuki, N. (2005). Cyclic AMP potentiates vascular endothelial cadherin-mediated cell-cell contact to enhance endothelial barrier function through an Epac-Rap1 signaling pathway. Mol. Cell. Biol. *25*, 136–146.

Fukuhara, S., Sakurai, A., Yamagishi, A., Sako, K., and Mochizuki, N. (2006). Vascular endothelial cadherin-mediated cell-cell adhesion regulated by a small GTPase, Rap1. J. Biochem. Mol. Biol. *39*, 132–139.

Gamble, J. R., Drew, J., Trezise, L., Underwood, A., Parsons, M., Kasminkas, L., Rudge, J., Yancopoulos, G., and Vadas, M. A. (2000). Angiopoietin-1 is an antipermeability and anti-inflammatory agent in vitro and targets cell junctions. Circ. Res. *87*, 603–607.

Garcia, J. G., Liu, F., Verin, A. D., Birukova, A., Dechert, M. A., Gerthoffer, W. T., Bamberg, J. R., and English, D. (2001). Sphingosine 1-phosphate promotes endothelial cell barrier integrity by Edg-dependent cytoskeletal rearrangement. J. Clin. Invest. *108*, 689–701.

Gates, J., and Peifer, M. (2005). Can 1000 reviews be wrong? Actin, alpha-catenin, and adherens junctions. Cell *123*, 769–772.

Gavard, J. (2009). Breaking the VE-cadherin bonds. FEBS Lett. *583*, 1–6.

Gavard, J., and Gutkind, J. S. (2006). VEGF controls endothelial-cell permeability by promoting the β-arrestin-dependent endocytosis of VE-cadherin. Nat. Cell Biol. *8*, 1223–1234.

Glading, A., Han, J., Stockton, R. A., and Ginsberg, M. H. (2007). KRIT-1/CCM1 is a Rap1 effector that regulates endothelial cell cell junctions. J. Cell Biol. *179*, 247–254.

Hippenstiel, S., Witzenrath, M., Schmeck, B., Hocke, A., Krisp, M., Krull, M., Seybold, J., Seeger, W., Rascher, W., Schutte, H., and Suttorp, N. (2002). Adrenomedullin reduces endothelial hyperpermeability. Circ. Res. *91*, 618–625.

Hogan, C., Serpente, N., Cogram, P., Hosking, C. R., Bialucha, C. U., Feller, S. M., Braga, V.M.M., Birchmeier, W., and Fujita, Y. (2004). Rap1 regulates the formation of E-cadherin-based cell-cell contacts. Mol. Cell. Biol. *24*, 6690–6700.

Imamura, Y., Itoh, M., Maeno, Y., Tsukita, S., and Nagafuchi, A. (1999). Functional domains of α-catenin required for the strong state of cadherin-based cell adhesion. J. Cell Biol. *144*, 1311–1322.

Kemler, R. (1993). From cadherins to catenins: cytoplasmic protein interactions and regulation of cell adhesion. Trends Genet. *9*, 317–321.

Kobielak, A., Pasolli, H. A., and Fuchs, E. (2004). Mammalian formin-1 participates in adherens junctions and polymerization of linear actin cables. Nat. Cell Biol. *6*, 21–30.

Kobielak, A., and Fuchs, E. (2004). α-Catenin: at the junction of intercellular adhesion and actin dynamics. Nat. Rev. Mol. Cell Biol. *5*, 614–625.

Kooistra, M. R., Corada, M., Dejana, E., and Bos, J. L. (2005). Epac1 regulates integrity of endothelial cell junctions through VE-cadherin. FEBS Lett. *579*, 4966–4972.

Kooistra, M. R., Dube, N., and Bos, J. L. (2007). Rap *1*, a key regulator in cell-cell junction formation. J. Cell Sci. *120*, 17–22.

Langeler, E. G., and van Hinsbergh, V. W. (1991). Norepinephrine and iloprost improve barrier function of human endothelial cell monolayers: role of cAMP. Am. J. Physiol. *260*, C1052–C1059.

Liu, F., Verin, A. D., Borbiev, T., and Garcia, J. G. (2001). Role of cAMP-dependent protein kinase A activity in endothelial cell cytoskeleton rearrangement. Am. J. Physiol. Lung Cell Mol. Physiol. *280*, L1309–L1317.

Lorenowicz, M. J., Fernandez-Borja, M., Kooistra, M. R., Bos, J. L., and Hordijk, P. L. (2008). PKA and Epac1 regulate endothelial integrity and migration through parallel and independent pathways. Eur. J. Cell Biol. *87*, 779–792.

Mege, R. M., Gavard, J., and Lambert, M. (2006). Regulation of cell-cell junctions by the cytoskeleton. Curr. Opin. Cell Biol. *18*, 541–548.

Nagafuchi, A., Ishihara, S., and Tsukita, S. (1994). The roles of catenins in the cadherin-mediated cell adhesion: functional analysis of E-cadherin-alpha catenin fusion molecules. J. Cell Biol. *127*, 235–245.

Ozawa, M., and Kemler, R. (1992). Molecular organization of the uvomorulin-catenin complex. J. Cell Biol. *116*, 989–996.

Pannekoek, W. J., Kooistra, M. R., Zwartkruis, F. J., and Bos, J. L. (2009). Cell-cell junction formation: the role of Rap1 and Rap1 guanine nucleotide exchange factors. Biochim. Biophys. Acta *1788*, 790–796.

Paul, R., Zhang, Z. G., Eliceiri, B. P., Jiang, Q., Boccia, A. D., Zhang, R. L., Chopp, M., and Cheresh, D. A. (2001). Src deficiency or blockade of Src activity in mice provides cerebral protection following stroke. Nat. Med. *7*, 222–227.

Price, L. S., Hajdo-Milasinovic, A., Zhao, J., Zwartkruis, F. J., Collard, J. G., and Bos, J. L. (2004). Rap1 regulates E-cadherin-mediated cell-cell adhesion. J. Biol. Chem. *279*, 35127–35132.

Qiao, J., Huang, F., and Lum, H. (2003). PKA inhibits RhoA activation: a protection mechanism against endothelial barrier dysfunction. Am. J. Physiol. Lung Cell Mol. Physiol. *284*, L972–L980.

Quinlan, M. P., and Hyatt, J. L. (1999). Establishment of the circumferential actin filament network is a prerequisite for localization of the cadherin-catenin complex in epithelial cells. Cell Growth Differ. *10*, 839–854.

Reynolds, A. B. (2007). p120-catenin: past and present. Biochim. Biophys. Acta *1773*, 2–7.

Reynolds, A. B., Daniel, J., McCrea, P. D., Wheelock, M. J., Wu, J., and Zhang, Z. (1994). Identification of a new catenin: the tyrosine kinase substrate p120cas associates with E-cadherin complexes. Mol. Cell. Biol. *14*, 8333–8342.

Rimm, D. L., Koslov, E. R., Kebriaei, P., Cianci, C. D., and Morrow, J. S. (1995). α1(E)-catenin is an actin-binding and -bundling protein mediating the attachment of F-actin to the membrane adhesion complex. Proc. Natl. Acad. Sci. USA *92*, 8813–8817.

Sako, Y., Nagafuchi, A., Tsukita, S., Takeichi, M., and Kusumi, A. (1998). Cytoplasmic regulation of the movement of E-cadherin on the free cell surface as studied by optical tweezers and single particle tracking: corralling and tethering by the membrane skeleton. J. Cell Biol. *140*, 1227–1240.

Sakurai, A., Fukuhara, S., Yamagishi, A., Sako, K., Kamioka, Y., Masuda, M., Nakaoka, Y., and Mochizuki, N. (2006). MAGI-1 is required for Rap1 activation upon cell-cell contact and for enhancement of vascular endothelial cadherin-mediated cell adhesion. Mol. Biol. Cell *17*, 966–976.

Spector, I., Shochet, N. R., Blasberger, D., and Kashman, Y. (1989). Latrunculins–novel marine macrolides that disrupt microfilament organization and affect cell growth: I. Comparison with cytochalasin D. Cell Motil. Cytoskeleton *13*, 127–144.

Takai, Y., Miyoshi, J., Ikeda, W., and Ogita, H. (2008). Nectins and nectin-like molecules: roles in contact inhibition of cell movement and proliferation. Nat. Rev. Mol. Cell Biol. *9*, 603–615.

Thurston, G., Suri, C., Smith, K., McClain, J., Sato, T. N., Yancopoulos, G. D., and McDonald, D. M. (1999). Leakage-resistant blood vessels in mice transgenically overexpressing angiopoietin-1. Science *286*, 2511–2514.

Vasioukhin, V., Bauer, C., Degenstein, L., Wise, B., and Fuchs, E. (2001). Hyperproliferation and defects in epithelial polarity upon conditional ablation of α-catenin in skin. Cell *104*, 605–617.

Vestweber, D., Winderlich, M., Cagna, G., and Nottebaum, A. F. (2009). Cell adhesion dynamics at endothelial junctions: VE-cadherin as a major player. Trends Cell Biol. *19*, 8–15.

Wallez, Y., and Huber, P. (2008). Endothelial adherens and tight junctions in vascular homeostasis, inflammation and angiogenesis. Biochim. Biophys. Acta *1778*, 794–809.

Watabe-Uchida, M., Uchida, N., Imamura, Y., Nagafuchi, A., Fujimoto, K., Uemura, T., Vermeulen, S., van Roy, F., Adamson, E. D., and Takeichi, M. (1998). α-Catenin-vinculin interaction functions to organize the apical junctional complex in epithelial cells. J. Cell Biol. *142*, 847–857.

Weis, S., Cui, J., Barnes, L., and Cheresh, D. (2004). Endothelial barrier disruption by VEGF-mediated Src activity potentiates tumor cell extravasation and metastasis. J. Cell Biol. *167*, 223–229.

Weis, W. I., and Nelson, W. J. (2006). Re-solving the cadherin-catenin-actin conundrum. J. Biol. Chem. *281*, 35593–35597.

Weiss, E. E., Kroemker, M., Rudiger, A. H., Jockusch, B. M., and Rudiger, M. (1998). Vinculin is part of the cadherin-catenin junctional complex: complex formation between α-catenin and vinculin. J. Cell Biol. *141*, 755–764.

Woodfin, A., Voisin, M. B., and Nourshargh, S. (2007). PECAM-1, a multifunctional molecule in inflammation and vascular biology. Arterioscler. Thromb. Vasc. Biol. *27*, 2514–2523.

Yamada, S., Pokutta, S., Drees, F., Weis, W. I., and Nelson, W. J. (2005). Deconstructing the cadherin-catenin-actin complex. Cell *123*, 889–901.

Yuan, S. Y. (2002). Protein kinase signaling in the modulation of microvascular permeability. Vasc. Pharmacol. *39*, 213–223.

Basic Res Cardiol (2010) 105:787–794
DOI 10.1007/s00395-010-0119-y

ORIGINAL CONTRIBUTION

A histamine H_2 receptor blocker ameliorates development of heart failure in dogs independently of β-adrenergic receptor blockade

Hiroyuki Takahama · Hiroshi Asanuma · Shoji Sanada · Masashi Fujita · Hideyuki Sasaki · Masakatsu Wakeno · Jiyoong Kim · Masanori Asakura · Seiji Takashima · Tetsuo Minamino · Kazuo Komamura · Masaru Sugimachi · Masafumi Kitakaze

Received: 21 July 2010 / Revised: 31 August 2010 / Accepted: 2 September 2010 / Published online: 18 September 2010

Abstract Histamine has a positive inotropic effect on ventricular myocardium and stimulation of histamine H_2 receptors increases the intracellular cAMP level via Gs protein, as dose stimulation of β-adrenergic receptors, and worsens heart failure. To test whether a histamine H_2 receptor blocker had a beneficial effect in addition to β-adrenergic receptor blockade, we investigated the cardioprotective effect of famotidine, a histamine H_2 receptor blocker, in dogs receiving a β-blocker. We induced heart failure in dogs by rapid ventricular pacing (230 beats/min). Animals received no drugs (control group), famotidine (1 mg/kg daily), carvedilol (0.1 mg/kg daily), or carvedilol plus famotidine. Both cardiac catheterization and echocardiography were performed before and 4 weeks after the initiation of pacing. Immunohistochemical studies showed the appearance of mast cells and histamine in the myocardium after 4 weeks of pacing. In the control group, the left ventricular ejection fraction (LVEF) was decreased after 4 weeks compared with before pacing (71 ± 2 vs. $27 \pm 2\%$, $p < 0.05$) and mean pulmonary capillary wedge pressure (PCWP) was increased (8 ± 1 vs. 19 ± 3 mmHg). Famotidine ameliorated the decrease of LVEF and increase of PCWP, while the combination of carvedilol plus famotidine further improved both parameters compared with the carvedilol groups. These beneficial effects of famotidine were associated with a decrease of the myocardial cAMP level. Histamine H_2 receptor blockade preserves cardiac systolic function in dogs with pacing-induced heart failure, even in the presence of β-adrenergic receptor blockade. This finding strengthens the rationale for using histamine H_2 blockers in the treatment of heart failure.

Keywords Heart failure · Histamine · Histamine H_2 receptor blocker · β-Adrenergic receptor blocker

H. Takahama · M. Wakeno · J. Kim · M. Asakura · M. Kitakaze (✉)
Department of Cardiovascular Medicine, National Cerebral and Cardiovascular Center, Suita, Osaka 565-8565, Japan
e-mail: kitakaze@zf6.so-net.ne.jp

H. Asanuma · H. Sasaki · K. Komamura · M. Sugimachi
Cardiovascular Dynamics Research Institute, National Cerebral and Cardiovascular Center, Suita, Japan

H. Asanuma
Department of Emergency Room Medicine, Kinki University School of Medicine, Osaka-Sayama, Japan

S. Sanada · M. Fujita · S. Takashima · T. Minamino
Department of Cardiovascular Medicine, Osaka University Graduate School of Medicine, Suita, Japan

Introduction

Chronic heart failure (CHF) is one of the major causes of morbidity and mortality worldwide, and is characterized by neurohormonal imbalances that include activation of the sympathetic nervous system [9, 15]. β-Adrenergic receptor blockade is a established treatment of CHF because it protects the heart from the harmful effects of the sympathetic nervous system that are partly mediated via cyclic adenosine monophosphate (cAMP)-dependent pathways [2, 34]. Interestingly, histamine H_2 receptors are linked to Gs proteins that facilitate the production of cAMP (as are β-adrenergic receptors) and are expressed in the heart [18, 29, 33]. Histamine has a positive inotropic effect on human ventricular myocardium and chronotropic effects [3, 12], and also autonomic control of the heart [21]. Indeed, we previously reported that famotidine, a histamine H_2